分类号________ 密级________

U D C________ 编号________

华中师范大学

博 士 学 位 论 文

RHIC-STAR 固定靶金金碰撞实验中质子数分布的高阶矩测量

学位申请人姓名: 张宇

申请学位学生类别: 全日制博士

申请学位学科专业: 粒子物理与原子核物理

指导教师姓名: 罗晓峰 教授

许怒 教授

忠诚博雅，朴实刚毅

博士学位论文

论文题目：**RHIC-STAR** 固定靶金金碰撞实验中质子数分布的高阶矩测量

论文作者：　张宇

指导教师：　罗晓峰 教授, 许怒 教授

学科专业：　粒子物理与原子核物理

研究方向：　相对论重离子碰撞物理

华中师范大学物理科学与技术学院

2022 年 5 月

Dissertation

Measurements of Higher Moments of Proton Multiplicity Distributions in Fixed-Target Au+Au Collisions by the STAR Experiment at RHIC

By

Yu Zhang

Supervisor: Xiaofeng Luo, Nu Xu

Specialty: Particle Physics and Nuclear Physics

Research Area: Physics of Relativistic Heavy Ion Collision

College of Physical Science and Technology

Central China Normal University

May, 2022

华中师范大学学位论文原创性声明和使用授权说明

原创性声明

本人郑重声明：所呈交的学位论文，是本人在导师指导下，独立进行研究工作所取得的研究成果。除文中已经标明引用的内容外，本论文不包含任何其他个人或集体已经发表或撰写过的研究成果。对本文的研究做出贡献的个人和集体，均已在文中以明确方式标明。本声明的法律结果由本人承担。

作者签名： 日期：2022 年 5 月 23 日

学位论文版权使用授权书

学位论文作者完全了解华中师范大学有关保留、使用学位论文的规定，即：研究生在校攻读学位期间论文工作的知识产权单位属华中师范大学。学校有权保留并向国家有关部门或机构送交论文的复印件和电子版，允许学位论文被查阅和借阅；学校可以公布学位论文的全部或部分内容，可以允许采用影印、缩印或其它复制手段保存、汇编学位论文。（保密的学位论文在解密后遵守此规定）保密论文注释：本学位论文属于保密，在______年解密后适用本授权书。非保密论文注释：本学位论文不属于保密范围，适用本授权书。

作者签名： 导师签名：

日期：2022 年 5 月 23 日 日期：2022 年 5 月 23 日

本人已经认真阅读“CALIS 高校学位论文全文数据库发布章程”，同意将本人的学位论文提交“CALIS 高校学位论文全文数据库”中全文发布，并可按“章程”中的规定享受相关权益。同意论文提交后滞后：□半年；□一年；□二年发布。

作者签名： 导师签名：

日期：2022 年 5 月 23 日 日期：2022 年 5 月 23 日

Contents

摘　要

高能重离子碰撞实验中一个主要的目的是为了研究量子色动力学（QCD）的相结构。在自然界中，夸克和胶子被禁锢在强子内部，人们预测高温和高密条件下，夸克和胶子自由度可以从强子中解禁出来，形成如同宇宙大爆炸后几十微秒产生的物质，其通常称为夸克胶子等离子体（Quark-Gluon Plasma，QGP）。在实验室中人们通过大型加速器把重离子加速到接近光速然后使其发生对撞，碰撞产生的能量被沉积在很小的空间内，创造出来极端高温高压的状态以期望可以产生 QGP。为了描述强子相和 QGP 相的相变，通常人们使用一张 QCD 相图，相图可以用温度和重子化学势来表示。从第一性原理出发的格点量子色动力学（Lattice QCD）计算表明，在零重子化学势时强子相和 QGP 相之间的转变是平滑穿越。而在有限的重子化学势区域，由于格点 QCD 计算存在符号问题无法给出可靠结果。很多基于 QCD 理论的研究结果表明在高重子化学势时，会存在一个一阶相变边界，以及一个一阶相边界的终点，这个终点通常叫做量子色动力学临界点（QCD Critical Point）。目前，临界点位置的理论计算还存在较大困难和不确定性因此，人们希望通过重离子碰撞能量扫描实验来获得不同的温度和重子化学势，从而探索 QCD 相图的不同区域，寻找 QCD 相变临界点和一阶相变边界。

理论预言，逐事件守恒量（如净重子数、净奇异数以及净电荷数）分布的高阶累积量是重离子碰撞中寻找临界点的敏感观测量。在 QCD 临界点的附近，系统的关联长度会发散，而守恒荷的高阶累积量可以敏感地反映临界关联长度的发散。另一方面，守恒量的高阶累积量可以直接与不同守恒荷热力学敏感系数紧密相关，所以实验测量结果可以与理论模型计算直接相连。最近来自对 RHIC 能量扫描第一阶段，质心系能量为 7.7 – 200 GeV 的实验数据分析显示，净质子数四阶涨落在最中心碰撞中存在一个非单调能量依赖趋势，其具有 3.1 σ 的显著性，这个结果和理论预言的 QCD 临界点的信号一致。但目前结果在能量 20 GeV 以下仍存在较大的统计误差，仍需要较大的统计量。另外在低能高重子密度区域仍存在很大空缺，在低能区域完成高阶涨落的测量对于寻找 QCD 临界点至关重要。本论文总结了对 STAR 在 2018 年固定靶实验采集的金金碰撞 $\sqrt{s_{\mathrm{NN}}} = 3\,\mathrm{GeV}$ 的实验数据的质子数高阶涨落的测量。论文将讨论具体的数据分析过程、方法、遇到的问题，以及最终的

测量结果和结论。

论文由以下几个章节组成：第 1 章介绍了研究动机以及实验观测量，即累积量的定义、模型的基线等。第 2 章介绍了 RHIC-STAR 实验装置，以及简要介绍了本分析中用到的探测器。第 3 章介绍了 3 GeV 的数据集，数据筛选过程，分析方法如探测器效率修正、事件堆叠效应修正和初始体积涨落修正等。第 4 章展示了对金金碰撞 $\sqrt{s_{\mathrm{NN}}} = 3$ GeV 在快度 $-0.9 < y < 0$ 及横动量 $0.4 < p_{\mathrm{T}} < 2.0$ GeV/c 的质子数分布高阶累积量测量结果，并和多个模型计算结果比较讨论。我们对最终的实验结果进行了探测器效率、堆叠事件修正和初始体积涨落修正，并把实验结果与强子输运模型、流体动力学模型的计算结果相比较，主要有以下结论：（1）对累积量使用体积涨落进行修正，结果显示仍可能存在未修正的效应，但体积涨落效应对最中心碰撞的 C_3/C_2 和 C_4/C_2 测量结果可能影响较小；（2）质子数分布高阶累积量的实验测量结果，其趋势可以较好地被强子输运模型的计算结果所重现，这预示着 3 GeV 可能是强子散射占主导的能量点，QCD 临界点如果存在并且可以被找到的话，可能仅存在于高于 3 GeV 的能量上。第 5 章是 3 GeV 净质子数分布高阶矩分析的总结和展望。在这篇论文中我们完成了固定靶实验碰撞能量为 3 GeV 金金碰撞的净质子高阶矩测量，主要结论见前述。RHIC 能量扫描第二阶段的数据采集已经结束，其碰撞能量为 3–19.6 GeV，统计量是第一阶段能量扫描所采集的数据量的 10 倍以上。这意味着我们可以在低能高重子密度区域对守恒荷的高阶涨落进行高精度的测量，甚至可能到高阶矩的八至十阶。守恒荷的高阶涨落分析对于寻找 QCD 临界点，研究 QCD 相图结构有重要意义。

关键词：相对论重离子碰撞；量子色动力学；临界点；逐事件涨落；守恒量高阶矩。

Abstract

Experimental evidences at RHIC and LHC have demonstrated the formation of Quark-Gluon Plasma (QGP) in ultra-relativistic heavy-ion collisions at small baryon chemical potential ($\mu_B \approx 0$ MeV) where the phase transition from the hadronic matter to QGP is suggested to be a crossover from state-of-the-art Lattice QCD calculations. It has been conjectured that there is a first-order phase transition and a critical point at finite μ_B region in the QCD phase diagram. In the search of the possible QCD critical point, higher-order cumulants of conserved quantities such as net-baryon number, net-strangeness number and net-charge number are sensitive observables to locate its position. Experimentally net-proton and net-kaon number are used proxy for net-baryon and net-strangeness number due to the difficulty to detect neutral particles in experiment. Recent results from the STAR experiment on net-proton higher-order cumulants have shown intriguing non-monotonic energy dependence with 3.1 σ significance in the most central Au+Au collisions at $\sqrt{s_{\rm NN}} = 7.7$ - 200 GeV while there are still large statistical uncertainties for lower energy $\sqrt{s_{\rm NN}} < 20$ GeV. More experimental data are needed to shrink the statistical uncertainty and confirm the trend.

In this year 2018, STAR collected around 250 million events with fixed-target experiment in Au+Au collision at $\sqrt{s_{\rm NN}} = 3$ GeV. 3 GeV is the lowest energy point from the STAR fixed-target experiment. The net-proton fluctuation measurements at this energy will enable us to discover QCD phase digram in a wide baryon chemical potential range. In this thesis, I will summarize the systematic analysis of event-by-event fluctuation of proton multiplicity distribution in 3 GeV Au+Au collisions. The relevant analysis details and correction methods will also be discussed. In order to understand the collision dynamics in the absence of the critical behavior, we have carried out simulations with transport model such as UrQMD for collisions at 3 GeV. Connections between experimental data and physics implication in the high baryon density region will be discussed.

The thesis is organized as follows. Chapter 1 is an introduction to the motivation, experimental observables. Chapter 2 shows experiment setup and a brief introduction to STR detectors. Chapter 3 discusses the dataset and data selection criteria as well as analysis techniques like detector efficiency correction, pileup effect correction and volume fluctuation correction. Chapter 4 shows final results. The main conclusions are shown below. 1) Due to the weak correlation between reference multiplicity and initial number of participants, large volume fluctuation effect was seen. It appears from UrQMD and Glauber that most central collisions are least affected. 2) The consistency between data and results of both UrQMD and hydrodynamic model of C_4/C_2 in the most central collisions, signal the effects of baryon number conservation and an energy regime dominated by hadronic interactions. 3) The QCD critical point, if discovered in heavy-ion collisions, could only exist at energies higher than 3 GeV. Chapter 5 shows the summary and outlook. We report a systematic study of cumulants and correlation functions of proton multiplicity distributions up to 6th-order from STAR fixed-target experiment $\sqrt{s_{\mathrm{NN}}} = 3$ GeV Au+Au collisions. The outlook is shown below. The BES-II program of RHIC has finished in 2021 and collected 10 times larger statistics than BES-I in Au+Au collisions at $\sqrt{s_{\mathrm{NN}}} = 3 - 19.6$ GeV. The high statistics data will allow one to perform high precision measurements of higher-order cumulants even up to 8$^{\text{th}}$ order and to explore the QCD phase diagram at high baryon density which is the most important region for the search of the QCD critical point.

Keywords: Relativistic heavy ion collision; QCD phase transition; QCD critical point; Fluctuation; Higher-order cumulant.

Chapter 1

Introduction

1.1 Standard Model

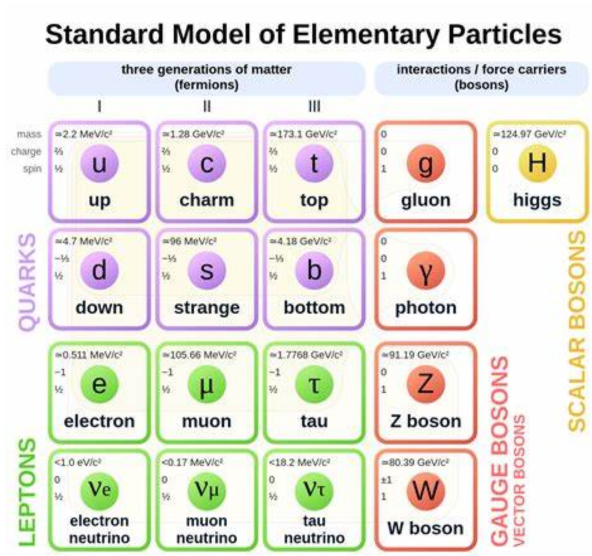

Figure 1.1.1: The standard model of elementary particles.

The Standard model of elementary particles is the theory which describes the forces of strong, weak and electromagnetic and how the corresponding carrier particles interact with each other. Figure 1.1.1 [1] shows the standard model of elementary particles. There are 12 fermions with spin $\frac{1}{2}$, 4 gauge bosons with spin 1 and Higgs boson with spin 0. According to the standard model, there are 3 generations (purple color in figure) of quarks, up and down quarks as the first generation, charm and strange quarks as the second generation and top and bottom quarks as the third generation. Considering each quark has its anti-particle and has 3 colors, there are in total 36 quarks. Baryon consists of 3 quarks while mesons consist of one quark and one anti-quark. Baryon and meson are both called hadron. Hadrons can participate in both strong and weak interactions.

There are also 3 generations of leptons (electron and electron neutrino as the first generation, muon and muon neutrino as the second generation and tau and tau neutrino as the third generation) which are shown with green color. Leptons can participate in all weak interactions and electro-magnetic interactions. The 4 particles shown with red color are gauge bosons which carry the fundamental interactions. The gluon has 8 species and carries strong interaction. The photon carries electromagnetic interaction and $W^{\pm}$ and Z carry weak interactions. The higgs boson in yellow color is the source of mass of all elemental particles.

The standard model successfully incorporates strong, weak and electromagnetic forces and predict the existence of up, down quarks and $W^{\pm}$ and Z bosons. But the standard model is not complete and there are still many unanswered questions. For example, the commonly known force gravity is not included in the standard model. The standard model may need to be expanded or revised.

1.2 Quantum Chromodynamics

The quantum chromodynamics (QCD) is the theory that describes the strong interaction. As is known quarks and gluons are color confined and form hadrons. Color confinement and asymptotic freedom are two key characteristics of the QCD. Asymptotic freedom means that when two color charges are more close, strong interactions between the two particles are weaker and vice versa.

The strong interaction coupling constant is defined as

$$\alpha_s(Q^2) = \frac{g_s^2(Q)}{4\pi} \approx \frac{1}{\beta_0 \ln(Q\Lambda^2)}, \tag{1.2.1}$$

where β_0 is written as

$$\beta_0 = \frac{33 - 2N_f}{12\pi}, \tag{1.2.2}$$

Λ is the QCD scale parameter, N_f is number of quarks flavors and Q is momentum transfer.

Figure 1.2.1 [2] shows the experimental measurements of coupling constant (α_s) of strong interactions as a function of the respective energy scale Q. It can be seen that with the increase of energy scale Q,

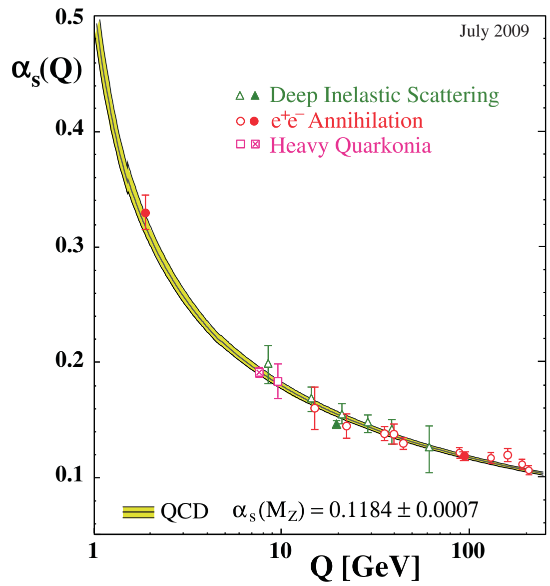

Figure 1.2.1: The running strong coupling constant α_s as a function of momentum transfer Q.

the coupling constant α_s decreases. If the distance between quarks is small or the momentum transfer is large then α_s becomes small which means the interaction strength between quarks becomes weaker. This is called asymptotic freedom. While if the distance between quarks is large or Q_s is small, then α_s becomes larger which means the interaction between quarks becomes strong, and quarks are confined within hadrons which are colorless. This is called color confinement. Thus in nature, no free quarks or gluons are directly observed.

1.3 QCD Phase Diagram and Critical Point

As is known from previous section quarks and gluons are color-confined. Then it can be imagined that quarks and gluons can be released under extremely high temperature and energy density. The color-deconfined phase with quark and gluon freedom is created which is usually called quark-gluon-plasma (QGP) which has been proved by experimental results from RHIC in collisions energies where μ_B approaches zero and the Large Hadron Collider (LHC) [3, 4, 5, 6]. A QCD phase diagram in terms of temperature and baryon chemical potential is used to display the hadronic phase and QGP phase. Fig. 1.3.1 shows a QCD phase diagram but its structure is less understood so far. In this region where $\mu_B \sim 0$, lattice

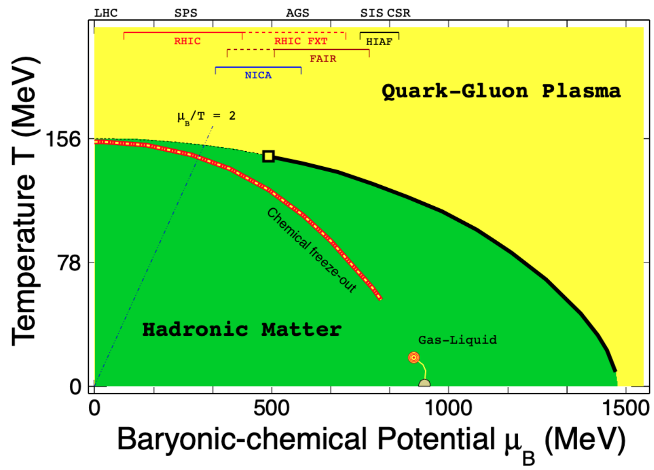

Figure 1.3.1: The QCD phase diagram in terms of temperature and baryon chemical potential. The red line indicates a freeze-out line while the black line indicates the QCD phase transition boundary. The black open square is the conjectured QCD critical point.

QCD (LQCD) predicts a smooth crossover from a hadronic state to a QGP phase [7, 8, 9] and QGP matter has been found to hadronize at temperatures close to the transition temperature at $\mu_B = 0$ MeV estimated by lattice QCD [10, 11]. At finite baryon chemical potential, due to the sign problem it is hard to perform calculation in lattice QCD. Various models predicted a 1st order phase transition [12, 13, 14]. If it is true, there should be an end point of the 1st order phase boundary [15, 16]. This end point is usually called QCD critical point. Provided that there is sufficient time for the system to develop to the size under study, the signal of the critical point could be measured in experiment [17, 18, 19, 20, 21, 22, 23]. The higher-order event-by-event fluctuations of conserved quantities like net-baryon number (B), net-electric charge number and net-strangeness number are sensitive observables to the system correlation length and may serve as indicators of critical behaviors [23, 24, 25, 26, 27, 28]. The critical signature of higher-order cumulants will be discussed in Sec. 1.7. This is one of the major goals of the beam energy scan program at the relativistic heavy-ion collider (RHIC) which is conducted at different collision energies ($\sqrt{s_{\rm NN}}$) so as to scan the QCD phase diagram to search for the possible QCD critical point [29, 30].

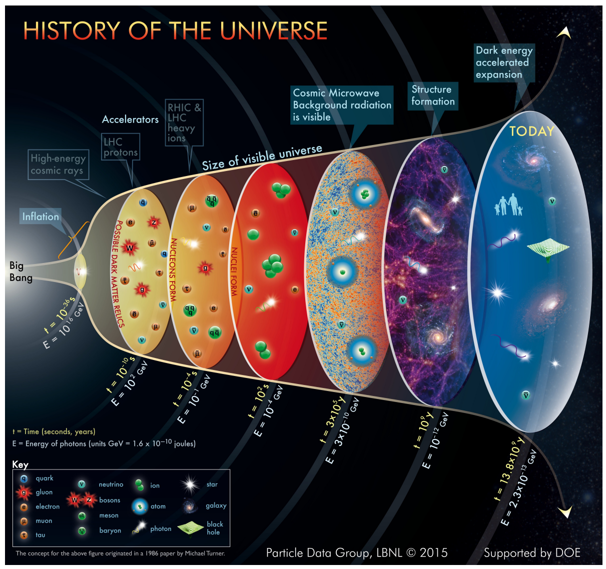

Figure 1.4.1: History of the universe.

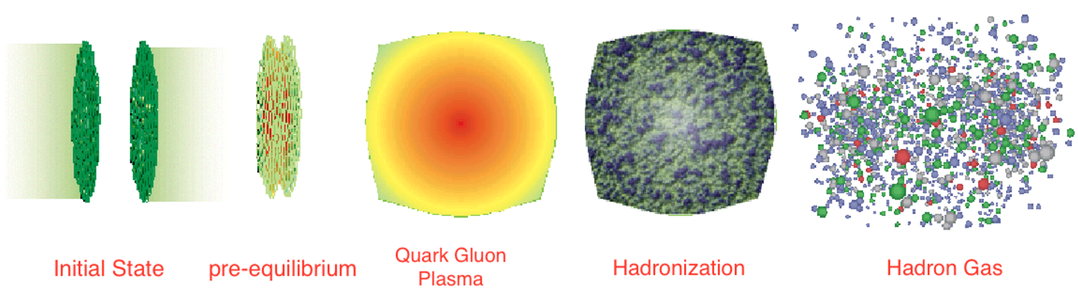

Figure 1.4.2: The evolution of heavy ion collision experiment.

1.4 Relativistic Heavy Ion Collision

In the low temperature and energy density world that human being live in, quarks and gluons are confined within hadrons. As mentioned in previous section QGP could exist under extremely high temperature or energy density, for example, a few millionths of second after the Big Bang, as shown in Fig. 1.4.1 [31]. People have to rely on heavy-ion collision experiments to create such condition. The relativistic heavy ion collider located in Brookhaven National Laboratory started the beam energy scan (BES) program phase I since the year 2010. Recently the BES phase II has just finished data-taking. The collision energy ($\sqrt{s_{\rm NN}}$) covers a wide range from 3 to 200 GeV.

Now let me briefly introduce different stages of heavy ion experiments. Experimentally heavy ions like gold or lead nuclei are accelerated to near the speed of light and collide with each other. The collision processes are described by several stages like pre-equilibrium, local thermal equilibrium and hadronization which are shown in Fig. 1.4.2.

Because of Lorentz contraction the two nuclei move like pancakes, then collide with each other, deposit energy. Nucleons are then released from ions and experience a pre-equilibrium stage then reaches the local thermal equilibrium. At this stage the energy density reaches a maximum and degree of freedom of quarks and gluons are released. The QGP is formed. The created hot and condensed matter expands due to a high pressure and cools down. When the temperature reaches the critical temperature quarks and gluons are confined within nucleons again and hadrons begin to form. There are two stages defined by people during hadronization. One is chemical freeze-out when the species of hadrons are finialized or we say there are no inelastic collisions. The other is kinematic freeze-out when elastic collisions cease. The formed hadrons are then measured by detectors.

1.5 Fluctuation

A system for grand canonical ensemble can be characterized by its dimensionless pressure which is the logarithm of the QCD partition function [32],

$$\frac{P}{T^4} = \frac{1}{VT^3} \ln[Z(V, T, \mu_B, \mu_Q, \mu_S)], \tag{1.5.1}$$

where V, T, μ_B, μ_Q and μ_S are volume of the system, temperature and chemical potential for conserved quantities of net-baryon number, net-charge number and net-strangeness number. Taking derivatives for each kind of chemical potential gives cumulants of each conserved quantity,

$$\chi_{i,j,k}^{B,Q,S} = \frac{\partial^{i+j+k}[p/T^4]}{\partial\hat{\mu}_B^i \partial\hat{\mu}_Q^j \partial\hat{\mu}_S^k}, \tag{1.5.2}$$

where $\chi_{i,j,k}^{B,Q,S}$ is defined as susceptibility. Then cumulants of the conserved quantities are given by

$$C_{i,j,k}^{B,Q,S} == \frac{\partial^{i+j+k}[Z(V,T,\mu_B,\mu_Q,\mu_S)]}{\partial\hat{\mu}_B^i \partial\hat{\mu}_Q^j \partial\hat{\mu}_S^k} = VT^3\chi_{i,j,k}^{B,Q,S}(T,\mu_B,\mu_Q,\mu_S) \tag{1.5.3}$$

which are readily compared with susceptibilities [9, 24, 32, 33, 34, 35, 36, 37, 38, 39]. As the hot dense matter created in heavy ion collisions expands during its evolution, its volume keeps changing. Experimentally the cumulant ratios are constructed to cancel volume dependence.

1.5.1 Cumulant

I will show the definition of cumulant in this section.

Let us consider a probability distribution $P(N)$ in which N is number of measured particle. The r^{th}-order raw moment (μ_r') and central moment (μ_r) are then defined by

$$\mu_r' = \sum_N N^r P(N) \tag{1.5.4}$$

and

$$\mu_r = \sum_N (N - \langle N \rangle)^r P(N) \tag{1.5.5}$$

where the bracket $\langle . \rangle$ indicates average. It is convenient to introduce a moment generating function,

$$G(\theta) = \sum_N e^{N\theta} P(N) = \langle e^{N\theta} \rangle, \tag{1.5.6}$$

Then the r^{th}-order raw moment can be expressed as r^{th}-order derivative of $G(\theta)$

$$\mu_r' = \frac{d^r}{d\theta^r} G(\theta)\Big|_{\theta=0}, \tag{1.5.7}$$

Since moments drastically increase with increasing the order r, cumulants are easier to handle rather than moments. A cumulant generating function is defined as

$$K(\theta) = \ln G(\theta), \tag{1.5.8}$$

The r^{th}-order cumulant is then given by taking derivatives of $K(\theta)$:

$$C_r = \frac{d^r}{d\theta^r} K(\theta)\Big|_{\theta=0}, \tag{1.5.9}$$

Cumulants can be expressed by raw moments and central moments recursively shown in Eqs. 1.5.11 and 1.5.10.

$$C_n(n \geq 1) = \mu_n' - \sum_{m=1}^{n-1} \binom{n-1}{m} \mu_m' C_{n-m}, \tag{1.5.10}$$

$$C_n(n \geq 2) = \mu_n - \sum_{m=1}^{n-2} \binom{n-1}{m} \mu_m C_{n-m}. \tag{1.5.11}$$

Cumulants up to 6^{th}-order in terms of central moments are shown below.

$$\begin{aligned}
C_1 &= \langle N \rangle, \\
C_2 &= \left\langle (\delta N)^2 \right\rangle = \mu_2, \\
C_3 &= \left\langle (\delta N)^3 \right\rangle = \mu_3, \\
C_4 &= \left\langle (\delta N)^4 \right\rangle - 3\left\langle (\delta N)^2 \right\rangle^2 = \mu_4 - 3\mu_2^2, \\
C_5 &= \left\langle (\delta N)^5 \right\rangle - 10\left\langle (\delta N)^2 \right\rangle \left\langle (\delta N)^3 \right\rangle = \mu_5 - 10\mu_2\mu_3, \\
C_6 &= \left\langle (\delta N)^6 \right\rangle + 30\left\langle (\delta N)^2 \right\rangle^3 - 15\left\langle (\delta N)^2 \right\rangle \left\langle (\delta N)^4 \right\rangle - 10\left\langle (\delta N)^3 \right\rangle^2 \\
&= \mu_6 + 30\mu_2^3 - 15\mu_2\mu_4 - 10\mu_3^2
\end{aligned} \tag{1.5.12}$$

where $\delta N = N - \langle N \rangle$.

The cumulants are related to the various moments as

$$M = C_1, \quad \sigma^2 = C_2, \quad S = \frac{C_3}{(C_2)^{3/2}}, \quad \kappa = \frac{C_4}{C_2^2}. \tag{1.5.13}$$

The products of moments can be expressed in terms of the cumulant ratios as

$$\sigma^2/M = \frac{C_2}{C_1}, \quad S\sigma = \frac{C_3}{C_2}, \quad \kappa\sigma^2 = \frac{C_4}{C_2}. \tag{1.5.14}$$

As is shown in Fig. 1.5.1, positive, negative and zero skewness and kurtosis can be seen in different colors.

1.5.2 Factorial Cumulant

Factorial moment generating function $H(t)$ is the mean value of t^N.

$$H(t) = \sum_N t^N P(N), \tag{1.5.15}$$

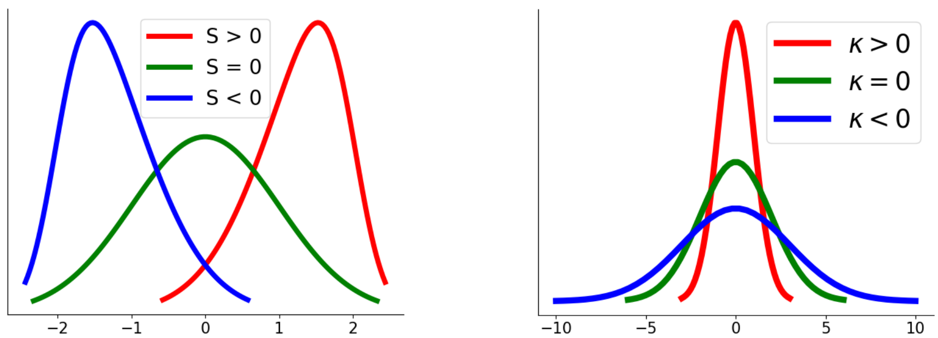

Figure 1.5.1: A sketch of negative, positive and zero skewness (S) and kurtosis (κ).

Then n^{th} order factorial moment (F_n) is obtained by taking n^{th} derivatives of $H(t)$.

$$F_n = \frac{d^n}{dt^n} H(t)|_{t=1}, \tag{1.5.16}$$

Factorial moments up to 6$^{\text{th}}$-order are shown below in terms of raw moments.

$$\begin{aligned}
F_1 &= \mu_1^{\prime}, \\
F_2 &= \mu^{\prime 2} - \mu^{\prime}, \\
F_3 &= \mu^{\prime 3} - 3\mu^{\prime 2} + 2\mu^{\prime}, \\
F_4 &= \mu^{\prime 4} - 6\mu^{\prime 3} + 11\mu^{\prime 2} - 6\mu^{\prime}, \\
F_5 &= \mu^{\prime 5} - 10\mu^{\prime 4} + 35\mu^{\prime 3} - 50\mu^{\prime 2} + 24\mu^{\prime}, \\
F_6 &= \mu^{\prime 6} - 15\mu^{\prime 5} + 85\mu^{\prime 4} - 225\mu^{\prime 3} + 274\mu^{\prime 2} - 120\mu^{\prime}.
\end{aligned} \tag{1.5.17}$$

It is seen that factorial moments are connected to raw moments by a recursion equation $F_n = \langle N(N-1)(N-2)\cdots(N-n+1) = \langle \frac{N!}{(N-n)!} \rangle$. Similarly $\ln H(t)$ is defined as the generating function of factorial cumulant which is also called integrated correlation function (for simplicity correlation function is used instead). Taking derivatives of $\ln H(t)$ gives n^{th} order factorial cumulant (κ_n).

$$\kappa_n = \frac{d^n}{dt^n} \ln H(t)|_{t=1}, \tag{1.5.18}$$

Factorial cumulants expressions can be displayed in terms of cumulants and vice versa. The expressions are shown below in 1.5.19 and 1.5.20.

$$
\begin{aligned}
\kappa_1 &= C_1, \\
\kappa_2 &= -C_1 + C_2, \\
\kappa_3 &= 2C_1 - 3C_2 + C_3, \\
\kappa_4 &= -6C_1 + 11C_2 - 6C_3 + C_4, \\
\kappa_5 &= 24C_1 - 50C_2 + 35C_3 - 10C_4 + C_5, \\
\kappa_6 &= -120C_1 + 274C_2 - 225C_3 + 85C_4 - 15C_5 + C_6.
\end{aligned}
\tag{1.5.19}
$$

$$
\begin{aligned}
C_1 &= \kappa_1, \\
C_2 &= \kappa_1 + \kappa_2, \\
C_3 &= \kappa_1 + 3\kappa_2 + \kappa_3, \\
C_4 &= \kappa_1 + 7\kappa_2 + 6\kappa_3 + \kappa_4, \\
C_5 &= \kappa_1 + 15\kappa_2 + 25\kappa_3 + 10\kappa_4 + \kappa_5, \\
C_6 &= \kappa_1 + 31\kappa_2 + 90\kappa_3 + 65\kappa_4 + 15\kappa_5 + \kappa_6.
\end{aligned}
\tag{1.5.20}
$$

Various useful correlation function ratios can be displayed in terms of cumulant ratios shown below.

$$
\begin{aligned}
\frac{\kappa_2}{\kappa_1} &= \frac{C_2}{C_1} - 1, \\
\frac{\kappa_3}{\kappa_1} &= (\frac{C_3}{C_1} - 1) - 3(\frac{C_2}{C_1} - 1), \\
\frac{\kappa_4}{\kappa_1} &= (\frac{C_4}{C_1} - 1) - 6(\frac{C_3}{C_1} - 1) + 11(\frac{C_2}{C_1} - 1), \\
\frac{\kappa_5}{\kappa_1} &= (\frac{C_5}{C_1} - 1) - 10(\frac{C_4}{C_1} - 1) + 35(\frac{C_3}{C_1} - 1) - 50(\frac{C_2}{C_1} - 1), \\
\frac{\kappa_6}{\kappa_1} &= (\frac{C_6}{C_1} - 1) - 15(\frac{C_5}{C_1} - 1) + 85(\frac{C_4}{C_1} - 1) - 225(\frac{C_3}{C_1} - 1) \\
&\quad + 274(\frac{C_2}{C_1} - 1).
\end{aligned}
\tag{1.5.21}
$$

$$
\begin{aligned}
\frac{C_2}{C_1} &= \frac{\kappa_2}{\kappa_1} + 1, \\
\frac{C_3}{C_2} &= \frac{\kappa_3/\kappa_1 - 2}{\kappa_2/\kappa_1 + 1} + 3, \\
\frac{C_4}{C_2} &= \frac{\kappa_4/\kappa_1 + 6\kappa_3/\kappa_1 - 6}{\kappa_2/\kappa_1 + 1} + 7, \\
\frac{C_5}{C_1} &= \frac{\kappa_5}{\kappa_1} + 10\frac{\kappa_4}{\kappa_1} + 25\frac{\kappa_3}{\kappa_1} + 15\frac{\kappa_2}{\kappa_1} + 1, \\
\frac{C_6}{C_2} &= \frac{\kappa_6/\kappa_1 + 15\kappa_5/\kappa_1 + 65\kappa_4/\kappa_1 + 90\kappa_3/\kappa_1 - 30}{\kappa_2/\kappa_1 + 1} + 31.
\end{aligned}
\tag{1.5.22}
$$

Reduced cumulant ratios ($\frac{C_n}{C_1} - 1$) are shown in Eq. 1.5.23.

$$
\begin{aligned}
\frac{C_2}{C_1} - 1 &= \frac{\kappa_2}{\kappa_1}, \\
\frac{C_3}{C_1} - 1 &= 3\frac{\kappa_2}{\kappa_1} + \frac{\kappa_3}{\kappa_1}, \\
\frac{C_4}{C_1} - 1 &= 7\frac{\kappa_2}{\kappa_1} + 6\frac{\kappa_3}{\kappa_1} + \frac{\kappa_4}{\kappa_1}, \\
\frac{C_5}{C_1} - 1 &= 15\frac{\kappa_2}{\kappa_1} + 25\frac{\kappa_3}{\kappa_1} + 10\frac{\kappa_4}{\kappa_1} + \frac{\kappa_5}{\kappa_1}, \\
\frac{C_6}{C_1} - 1 &= 31\frac{\kappa_2}{\kappa_1} + 90\frac{\kappa_3}{\kappa_1} + 65\frac{\kappa_4}{\kappa_1} + 15\frac{\kappa_5}{\kappa_1} + \frac{\kappa_6}{\kappa_1}.
\end{aligned}
\tag{1.5.23}
$$

1.6 Useful Statistical Distributions

1.6.1 Binomial Distribution

Bernoulli experiment describes a random experiment that is independently repeated. There will be two outcomes for each trial: failure or success. If enough number of times are repeated one can obtain some useful information from the experiment.

Binomial distribution describes number of successful or failed Bernoulli experiments where experiments share identical possibility to succeed/fail. The probability distribution of Binomial distribution of random variable N is given by

$$P(N = k) = \binom{N}{k} p^k (1 - p)^{N-k} \tag{1.6.1}$$

where k is number of successful/failed trials and p is probability for each trial to succeed/fail.

Binomial distribution is useful in experiment related to detector efficiency. As will be discussed in Sec. 3.3 the detector efficiency correction method is based on Binomial responded detector efficiency.

1.6.2 Poisson Distribution

Poisson distribution is a famous discrete probability distribution in the theory of statistics. Its probability distribution ($P(N=k)$) is given by

$$P(N=k) = \frac{\lambda^k}{k!}e^{-\lambda}, k = 0, 1, \cdots \tag{1.6.2}$$

where λ is the average of number of events that occur. It is used to describe number of events that randomly occur per unit time. As there is no correlation between each event thus Poisson distribution is commonly used as a baseline to compare with experiment data.

The moment generating function of Poisson distribution is

$$M(t) = \sum_{k=0}^{\infty} e^{kt}e^{-\lambda}\frac{\lambda^k}{k!} = e^{-\lambda}\sum_{k=0}^{\infty}\frac{(\lambda e^t)^k}{k!}e^{\lambda(e^t-1)}, \tag{1.6.3}$$

then cumulant generating function is shown as

$$K(t) = \ln M(t) = \lambda(e^t - 1), \tag{1.6.4}$$

. Taking derivatives of $K(t)$ gives cumulants of each order which are shown as

$$C_n = \lambda\frac{d^n}{dt^n}(e^t - 1)|_{t=0} = \lambda e^t|_{t=0} = \lambda. \tag{1.6.5}$$

and it is seen that cumulant ratios are equal to unity.

1.6.3 Gaussian Distribution

Gaussian distribution is an important distribution in the theory of statistics. Its probability distribution $P(N)$ for a random variable N is described by

$$P(N) = \frac{1}{\sqrt{2\pi}\sigma}e^{-\frac{(N-\mu)^2}{2\sigma^2}}, \tag{1.6.6}$$

where μ and σ are the mean value and standard deviation of N, respectively. Similarly the moment generating function $M(t)$ and cumulant generating function $K(t)$ are expressed as

$$M(t) = Ee^{tN} = \int_{-\infty}^{\infty} e^{tN} \frac{1}{\sqrt{2\pi\sigma}} e^{-\frac{(N-\mu)^2}{s\sigma^2}} dN, \tag{1.6.7}$$

and

$$K(t) = \ln M(t) = \mu t + \frac{1}{2}\sigma^2 t^2. \tag{1.6.8}$$

Taking derivatives of $K(t)$ goves cumulants of each order which are shown below

$$C_1 = \mu, \quad C_2 = \sigma^2, \quad C_n(n \geq 3) = 0. \tag{1.6.9}$$

From Eq. 1.6.9 one can see that higher order cumulants ($n \geq 3$) equal zero that means the cumulant ratios like $S\sigma$ and $\kappa\sigma^2$ are measure of non-Gaussian fluctuation.

1.7 Signature of the QCD Critical Point

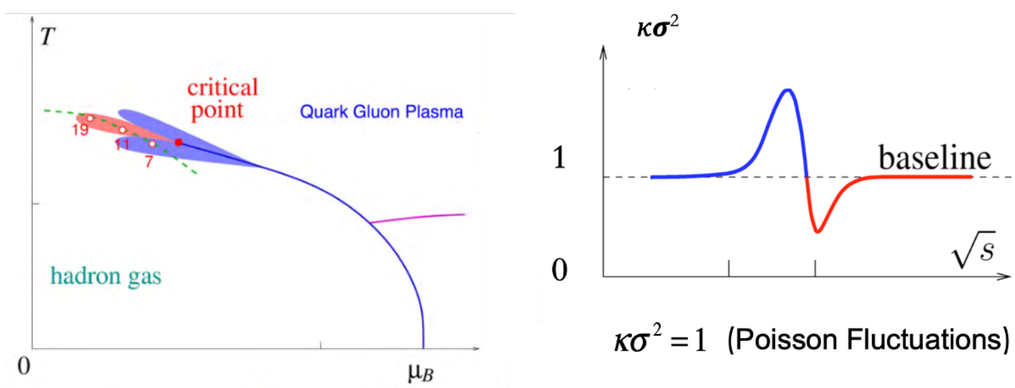

Figure 1.7.1: Left panel: the QCD phase diagram in terms of temperature T and baryon chemical potential $\mu_{\rm B}$ with conjectured QCD critical point (red circle) and $1^{\rm th}$-order phase transition line (blue line). The green dash line indicates chemical freeze-out. Right panel: $4^{\rm th}$ cumulant ratio C_4/C_2 ($\kappa\sigma^2$) as a function a collision energy ($\sqrt{s}$). The dash line indicates the Poisson baseline.

Higher order cumulants of conserved quantities like net-baryon (B) number, net-charge (Q) number and net-strangeness (S) number are proposed as promising observables to search for QCD critical point as well as the 1st-order phase transition boundary [20, 24, 40, 41, 42]. It is known at the critical point the correlation length ξ of the system will diverge, and cumulants of conserved quantities (B, Q, S) are proved to be sensitive to ξ. Theoretical calculations of sensitivity of cumulants on critical point are briefly shown below.

The calculations [25, 26, 27] are based on the probability distribution of an order parameter field that will develop finite correlation length at the critical point. The probability distribution $P(\sigma)$ is expresses as $P(\sigma) \sim e^{-\Omega(\sigma)/T}$ where Ω is the free energy of the field σ. Ω can be expanded in powers of σ and the gradients,

$$\Omega(\sigma) = \int d^3x[\frac{1}{2}(\sigma)^2 + \frac{m_\sigma^2}{2}\sigma^2 + \frac{\lambda_3}{3}\sigma^3 + \frac{\lambda_4}{4}\sigma^4 + \cdots], \tag{1.7.1}$$

where $m_\sigma = 1/\xi$ is the σ field screening mass, λ_3 and λ_4 are interaction couplings. Let V be the volume of the system. The moments of the zero momentum mode is $\sigma_V \equiv \int d^3\sigma(x)$, and cumulants of the σ field are

$$\begin{aligned} C_2 &= \langle\sigma_V^2\rangle = VT\xi^2, \\ C_3 &= \langle\sigma_V^3\rangle = 2\lambda_3 VT\xi^6, \\ C_4 &= \langle\sigma_V^4\rangle - 3\langle\sigma_V^2\rangle^2 = 6VT^3[2(\lambda_3\xi)^2 - \lambda_4]\xi^8. \end{aligned} \tag{1.7.2}$$

At the critical point, the correlation length $\xi \to \infty$, the couplings λ_3 and λ_4 scale with ξ,

$$\begin{aligned} \lambda_3 &= \tilde{\lambda}_3 T(T\xi)^{-3/2}, \\ \lambda_4 &= \tilde{\lambda}_4 T\xi^{-1}. \end{aligned} \tag{1.7.3}$$

where $\tilde{\lambda}_3$ and $\tilde{\lambda}_4$ are dimensionless couplings and do not depend on ξ. According to the direction of approach to the critical point (crossover or 1th-order phase transition), the $\tilde{\lambda}_3$ and $\tilde{\lambda}_4$ vary from 0 to ~8 and from ~4 to ~20, respectively. Taking Eq. 1.7.3 to Eq. 1.7.2, we have

$$\begin{aligned} C_3 &= 2\tilde{\lambda}_3 VT^{3/2}\xi^{4.5}, \\ C_4 &= 6VT^2(2\tilde{\lambda}_3 - \tilde{\lambda}_4)\xi^7. \end{aligned} \tag{1.7.4}$$

Fig. 1.7.1 (left panel) shows the QCD phase diagram in terms of temperature and baryon chemical potential. The contributions from QCD critical point to the 4th-order cumulant ratio C_4/C_2 ($\kappa\sigma^2$) calculated from σ model [25, 26, 27] are drawn with red (negative contribution) and blue (positive contribution) shaded area. Due to the contributions from QCD critical point, $\kappa\sigma^2$ shows a non-monotonic energy dependence which is a signature of the critical point. However, in heavy ion collisions, effects like finite size, limited lifetime of the hot nuclear system, thermal blurring, diffusion as well as resonance decay effects may put constraints on the significance of signals [43, 44, 45, 46, 47, 48, 49, 50, 51, 52]. When studying the higher-order cumulant ratios, it is essential to demonstrate that in the absence of critical behavior, the ratios are consistent with the expectations from the non-critical baseline. The expectation for the C_4/C_2 ratio under Poisson statistics is unity, though the measured net-proton C_4/C_2 within the experimental kinematic acceptance is expected to show a reduction due to the baryon number conservation [53, 54]. This reduction is expected to increase with decreasing collision energy [55]. Previously, the HADES Collaboration reported their measurement of the proton cumulant ratio of C_4/C_2 in central Au+Au collisions at $\sqrt{s_{\mathrm{NN}}} = 2.4\,\mathrm{GeV}$ consistent with unity within large uncertainties. More precise data at the low collision energy is needed to quantitatively interpret the collision energy dependence of the (net-)proton fluctuation.

1.8 Thesis Motivation

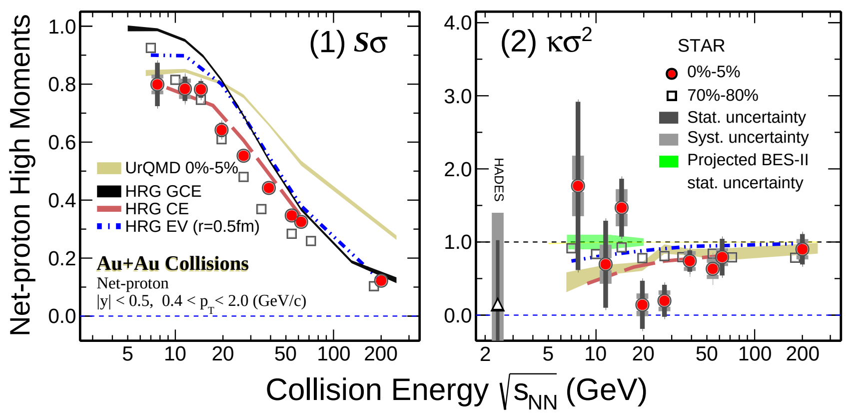

Figure 1.8.1: Collision energy dependence of cumulant ratios $S\sigma$ and $\kappa\sigma^2$ of net-proton multiplicity distributions in Au+Au collisions of RHIC beam energy scan I energies within acceptance $|y| < 0.5$ and $0.4 < p_{\mathrm{T}} < 2.0\ \mathrm{GeV}/c$.

The thesis is motivated by the critical signature shown in Sec. 1.7 to measure the net-proton cumulants from the dedicated fixed-target experiment of the STAR at $\sqrt{s_{\mathrm{NN}}} = 3\,\mathrm{GeV}$ which is the lowest and important energy point of the RHIC beam energy scan program at high baryon density region.

At small μ_{B} lattice QCD calculations have predicted positive cumulant ratio of C_4/C_2 and negative ratios of C_5/C_1 and C_6/C_2 for the formation of QGP matter. The results suggest that a critical point below

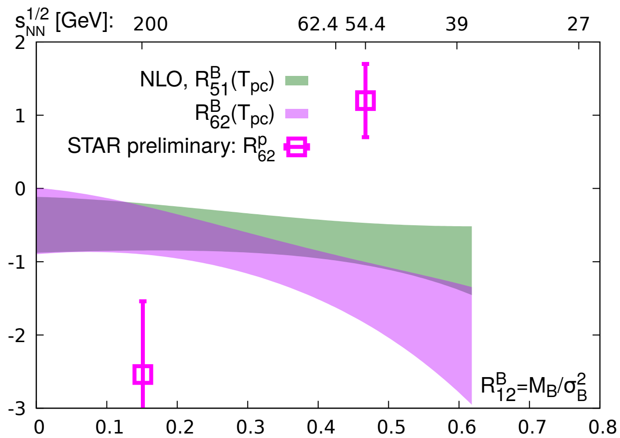

Figure 1.8.2: Lattice QCD calculations of net-baryon cumulant ratios of C_5/C_1 (green shaded area) and C_6/C_2 (pink shaded area) at $\sqrt{s_{\mathrm{NN}}} = 39 - 200\,\mathrm{GeV}$. The pink squares are cumulant ratio C_6/C_2 from STAR preliminary results in Au+Au collisions at $\sqrt{s_{\mathrm{NN}}} = 54.4$ and $200\,\mathrm{GeV}$ for the 0-40% centrality class.

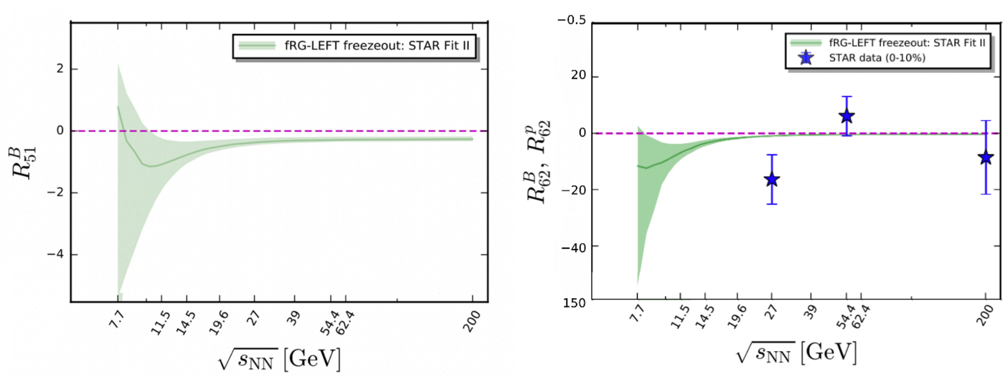

Figure 1.8.3: Theoretical calculations using the functional renormalisation group (fRG) approach of baryon number fluctuations C_5/C_1 and C_6/C_2 as functions of the collision energy.

μ_B < 200 Mev is unlikely to exist [56]. As is shown in Sec. 1.7 the non-monotonic energy dependence of $\kappa\sigma^2$ is a signature of the QCD critical point. Figure 1.8.1 shows energy dependence of cumulant ratios $S\sigma$ and $\kappa\sigma^2$ of net-proton multiplicity distributions in Au+Au collisions at $\sqrt{s_{\rm NN}}$ = 7.7-200 GeV [57]. The $S\sigma$ (left panel) shows a decreasing trend with the increase of collision energy both in central and peripheral collisions. The decreasing trend can be qualitatively described by HRG [47] and UrQMD [58, 59] models. The $\kappa\sigma^2$ (right panel in Fig. 1.8.1) shows a non-monotonic energy dependence in central collisions while the results for peripheral collisions show monotonic energy dependence. The non-monotonic trend in central collisions can not be described by different conditions (GCE, EV, and CE) of HRG and UrQMD models. These results from BES-I inspired a BES-II program which focuses on the collision energy region between 3 – 20 GeV (μ_B = 200 – 750 MeV). BES-II combines both collider and fixed-target configurations of the STAR experiment in order to investigate the nature of the phase transition [60].

It was also pointed out that the experimental measured multiplicity distributions suffer sizable contributions from fluctuating collision volume. This effect, often called volume fluctuation (VF), is expected to be larger at low collision energies and/or low multiplicity events. As is shown in the study [61] using hadronic transport model in $\sqrt{s_{\rm NN}}$ = 3 GeV Au+Au collisions that at low energies, the centrality resolution for determining the collision centrality using charged particle multiplicities is not sufficient to reduce the initial volume fluctuation effect for higher-order cumulant analysis. Therefore, to better understand the effect of VF, it is important to systematically perform measurements within various kinematic windows and different collision centralities.

Recently first principle lattice QCD calculations shown in Fig. 1.8.2 on the baryon number susceptibilities ratios χ_6^B/χ_2^B and χ_6^B/χ_2^B cover a wide range of collision energy ($\sqrt{s_{\rm NN}}$) from 39 to 200 GeV [62]. Negative signs of χ_6^B/χ_2^B and χ_6^B/χ_2^B are predicted due the crossover transition of between QGP and hadron phase. The calculation using the functional renormalisation group (FRG) approach shown in Fig. 1.8.3 also gives negative χ_6^B/χ_2^B and χ_6^B/χ_2^B over a wide range of μ_B 20 - 420 MeV corresponding to central Au+Au collisions at $\sqrt{s_{\rm NN}}$ = 200 and 7.7 GeV, respectively [63]. While this is contrast to the calculations from hadronic transport model UrQMD and HRG model which C_5/C_1 and C_6/C_2 remain positive. As there is no phase transition physics is implemented in the UrQMD and HRG models, the calculations would be baselines for the case without critical physics.

It is pointed in Ref. [64] that acceptance dependence of cumulants and correlation functions are also important to study QCD phase transition. It is pointed out that there may be two qualitatively different regimes: $\Delta y \gg \Delta y_{\rm corr}$ and $\Delta y \ll \Delta y_{\rm corr}$, where Δy is the width of the kinematic acceptance in rapidity and $\Delta y_{\rm corr}$ is the range of the proton correlations in rapidity. When $\Delta y \ll \Delta y_{\rm corr}$, one expects the cumulant ratios to approach the Poisson limit at $\Delta y \sim \langle N \rangle \to 0$. Alternatively, one expects the correlation functions to become rapidity independent as Δy becomes wider. In the $\Delta y \gg \Delta y_{\text{corr}}$ regime as Δy increases, cumulants are expected to grow linearly from the uncorrelated contributions while the cumulant ratios are expected saturate from any physical correlations. Therefore, the rapidity and transverse momentum dependence of proton cumulants and correlation functions are important to search for signatures of criticality. It should be noted, the acceptance dependence could be sensitive to non-equilibrium effects [65, 66], smearing due to diffusion and hadronic rescattering in the expansion of the system [67].

Chapter 2

Experiment Setup

2.1 Relativistic Heavy Ion Collider

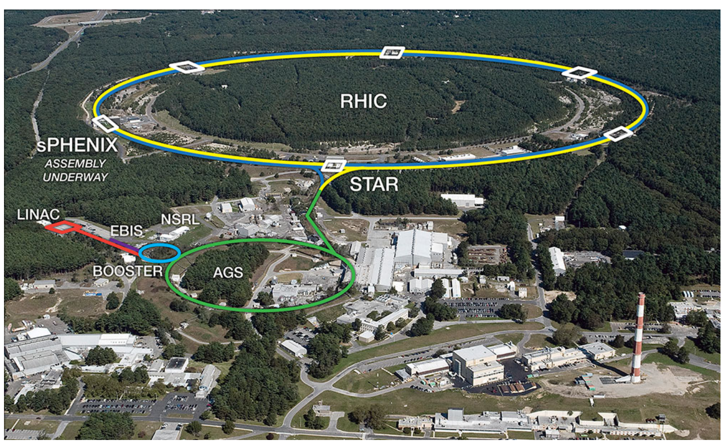

Figure 2.1.1: The relativistic heavy ion collider located in Brookhaven national laboratory of the US.

The relativistic heavy ion collider (RHIC) shown in Fig. 2.1.1 [68] is located in Brookhaven national laboratory [1] in which the STAR experiment [2] is one of the premier particle detectors in the world. In RHIC two beams of gold ions are accelerated at nearly the speed of light in oppotite directions and travel around

[1]https://www.bnl.gov

[2]https://www.star.bnl.gov

RHIC 2.4-mile ring, and finally collide with each other to create a very high temperature and energy density region which is supposed to melt proton and neutrons and to free quarks and gluons for a short time.

2.2 STAR Detector System

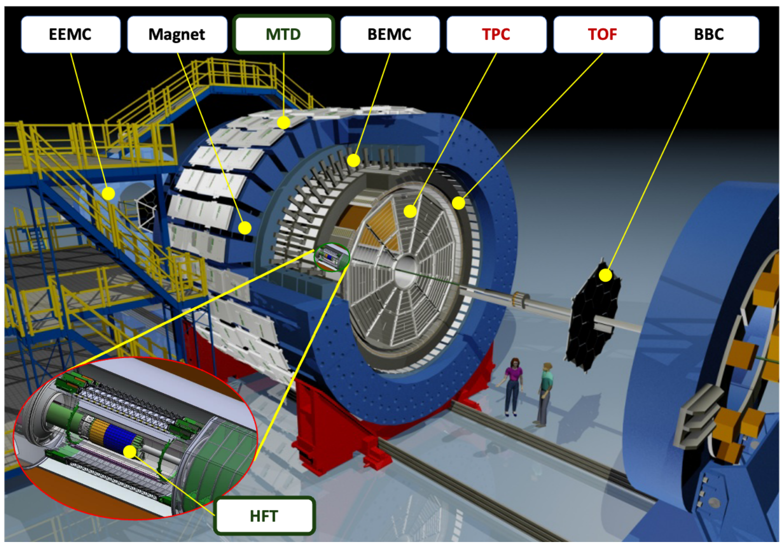

Figure 2.2.1: The STAR detector system.

The STAR experiment at RHIC is to study the formation and properties of quark gluon plasma which is believed to exist at very high energy density generated by heavy ion collisions. Because of the complexity of the system produced in collisions the STAR detector system consists of several types of detectors which are functioning to measure different types of particles. With these detectors working together experiment data of heavy ion collisions is collected for scientific analysis.

In the following sections, as they are closely related to particle identification, the two detectors called time projection chamber (TPC) and time of flight detector (TOF) will be mainly discussed.

2.2.1 Time Projection Chamber

The time projection chamber [69] shown in Fig. 2.2.2 is a tracking device with which trajectories, momentum as well as ionization energy loss of particles when they travel through TPC are measured. The

TPC is a cylinder that is 4.2 m long and 4 m in diameter. Its acceptance covers ± 1.8 pseudo-rapidity through the full azimuthal angle. It is an empty barrel and sits in a large solenoidal magnet ($|B| = 0.5$ T) along the beam pipe (z-axis) direction. The magnetic field is sued to bend the trajectories of the original particles and also help keep the drifting electrons from dispersing as they travel. The TPC is filled with P10 gas (10% methane, 90% argon) with a well-defined, uniform, electric field of $\sim$135 V/cm and has readout 12 sectors on both ends. Collisions happen near the center of the TPC. When charged particles transverse through the TPC they ionize gas atoms and ionized gas atoms will release secondary electrons. Then those free electrons will drift at a steady speed around 5.45 cm/μs to the readout end caps at the bottom of TPC. The energy deposited from drift electrons to the readout end caps and their drift time are measured. With these information the ionization position (TPC hits) of charged particles are obtained and trajectories are reconstructed. The energy loss of each ionization point is used to identify particle species.

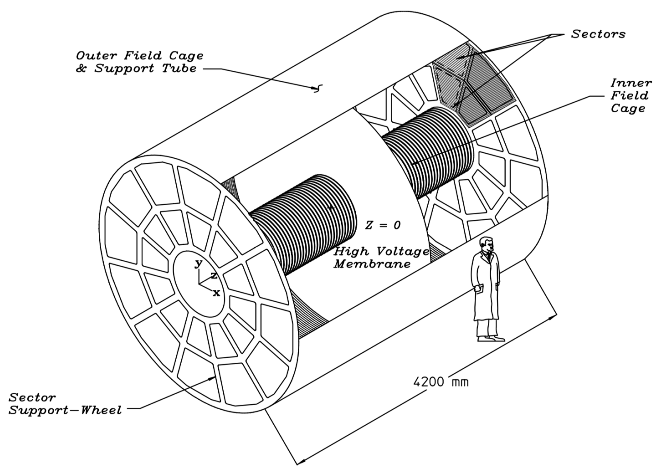

Figure 2.2.2: The time projection chamber of the STAR detector system.

Fig. 2.2.3 shows the energy loss (dE/dx) for particles in the TPC as a function as a function of the rigidity (p/q GeV/c) of the primary particle in $\sqrt{s_{\mathrm{NN}}} = 39$ GeV Au+Au collisions. The lines on the plot are fits from Bichsel function [70]. It is seen that protons are well separated from pions at $p < 1$ GeV/c.

The Bathe-Bloch Eq. 2.2.1 gives mean value of charged particle ionized energy loss

$$\frac{\mathrm{dE}}{\mathrm{dx}} = -K\frac{Z}{A}\frac{\rho}{\beta^2}\{\ln(\frac{2m_e c^2\gamma^2\beta^2}{I}) - \beta^2 - \frac{\delta}{2}\} \tag{2.2.1}$$

where $2\pi N_a r_e^2 m_e c^2 = 0.1535$ MeVcm^2/g, $\gamma = 1/\sqrt{1-(v/c)^2}$. The measured energy loss (dE/dx) then can be compared with expected value shown in Eq. (2.2.1). The experimental measured dE/dx values of tracks

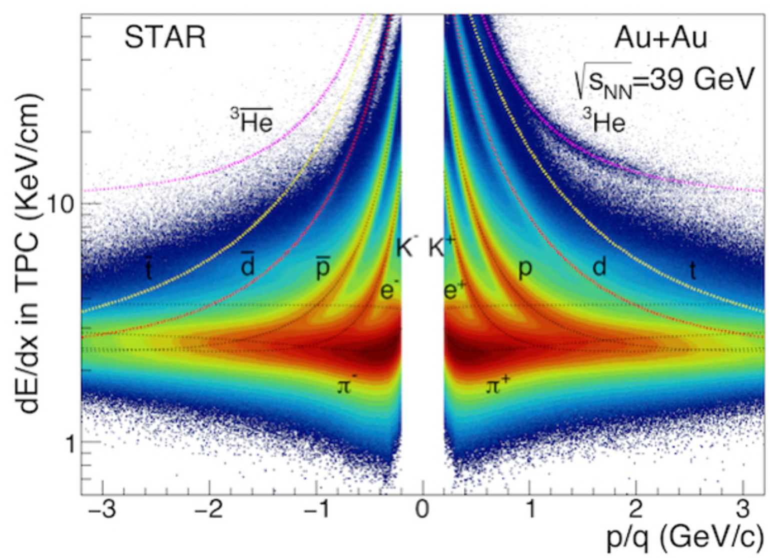

Figure 2.2.3: The energy loss distribution for primary and secondary particles in the STAR TPC as a function of the rigidity (p/q GeV/c) of the primary particle in $\sqrt{s_{\rm NN}} = 39$ GeV Au+Au collisions.

is usually described by Landau distribution which has a long tail which means a direct mean will lose some information of tracks. Thus a 70% truncated mean (typically 30% is removed before taking average) of dE/dx is calculated. Then Bichsel function [70] is used to fit dE/dx distribution. A variable $n\sigma$ is calculated by $n\sigma_{proton} = \frac{1}{R}\log\frac{\langle \mathrm{dE/dx_{measured}}\rangle}{\langle \mathrm{dE/dx_{Bichsel}}\rangle}$ where R is the resolution of energy loss. The $n\sigma$ describes number of σ that a track is away from expected value for this particle species. The $n\sigma$ distribution follows Gaussian statistics with $\sigma = 1$ and mean value is zero. Usually placing a cut on $|n\sigma| < 3$ means dropping 0.3% of tracks that are deviated from expected values of Bichsel model .

2.2.2 Time of Flight

To ensure high purity of proton for higher momentum ($p > 1$ GeV/c for data in collider mode and $p > 2$ GeV/c for fixed-target mode, refer to Sec. 3.1.3) the barrel Time of Flight (TOF) detector is used. The TOF detector is based on the Multi-gap Resistive Plate Chamber (MRPC) technology and located outside of TPC detector. Fig. 2.2.4 shows the tray, module and pad of TOF. There are in total 120 TOF trays mounted on the east and west sides of TPC so that TOF covers pseudo-rapidity $|\eta| \leq 1$ in full 2π azimuthal angle. Each TOF tray has 32 MRPC modules. MRPC mainly contains two electrodes with a voltage of 7 KV and

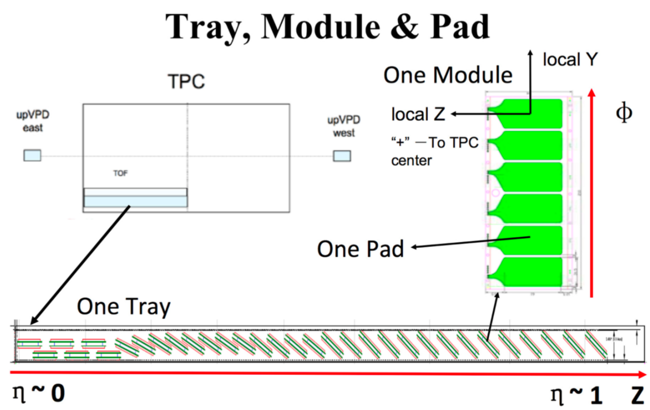

Figure 2.2.4: The time of flight detector of the STAR detector system.

a stack of resistive glass plates with 6 uniform gas gaps between them. Every small gas gap is filled with high and uniform electric field. When charged particles pass through the module, there will be simultaneous avalanches in the 6 gas gaps. Superposition of avalanches of 6 gas gaps is then measured. Given the track length L and total momentum p reconstructed by TPC, the track speed β as well as particle mass m are then calculated by

$$\begin{aligned} \beta &= \frac{L}{ct}, \\ m^2 &= p^2(\frac{1}{\beta} - 1) \end{aligned} \tag{2.2.2}$$

where t is flight time of tracks.

2.3 STAR Fixed-Target Experiment

In this section I introduce the fixed-target program in the STAR experiment. The fixed target experiment at $\sqrt{s_{\mathrm{NN}}}$= 3 GeV in Au+Au collisions allows for a statistically significant measurement of $\kappa\sigma^2$ at a collision energy between the HADES measurement [71] at $\sqrt{s_{\mathrm{NN}}}$= 2.4 GeV and the STAR's lowest energy point at $\sqrt{s_{\mathrm{NN}}}$= 7.7 GeV in collider mode.

Fig. 2.3.1 shows the schematic of fixed-target setup in the STAR experiment. The gold target was located at 200.7 cm from the center of the TPC and of thickness 1.93 g/cm^2 (0.25 mm) corresponding to a 1% interaction probability. An incident beam consisting of 12 bunches of 7×10^9 gold ions, circulated in

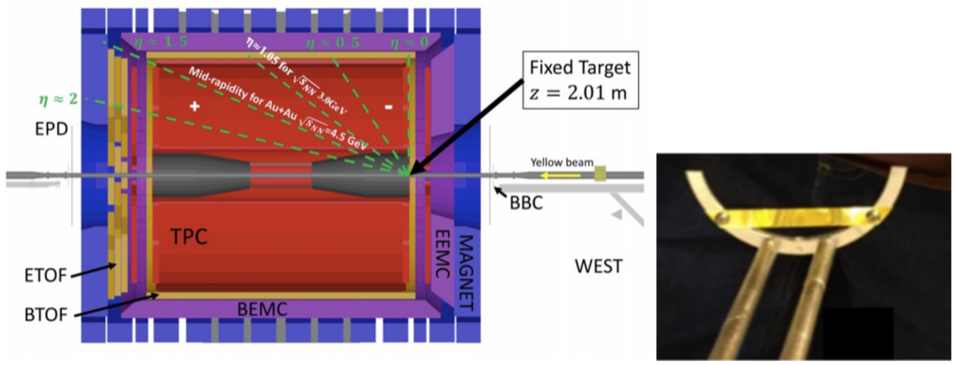

Figure 2.3.1: Left panel: The setup of fixed-target program of STAR experiment. Right panel: The gold target which is a 0.25 mm-thick foil.

the RHIC ring at 1 MHz with an energy of 3.85 GeV per nucleon, entered from the right side of the plot and bombarded the target.

Chapter 3

Analysis Details

3.1 Data Set

The data used in this analysis is collected from the STAR fixed-target experiment run in Au+Au collisions at $\sqrt{s_{\rm NN}}$= 3 GeV in the year 2018. Around 140 million events are used in this analysis.

$\sqrt{s_{\rm NN}}$(GeV)	**Trigger Setup Name**	**Year**	**Production Tag**	**Library**	**Trigger ID**
3.0	production_3p85GeV_fixedTarget_2018	2018	P19ie	SL20c	620052

Table 3.1: Data set of Au+Au collisions at $\sqrt{s_{\rm NN}}$= 3 GeV from fixed-target experiment.

3.1.1 Run Selection

Good runs are selected by run-by-run QA analysis shown in Fig. 3.1.1. Event level variables, like RefMult, V_z, V_r, and RefMult3 and track level variables like p_T, ϕ, η, and DCA are used to do run-by-run QA. The mean value of each variable per run are plotted as a function of run index. Runs that are within mean value $\pm$ 3σ are selected as good runs. Based on this selection, 72 runs are collected which is shown in Table 3.1.

Good Run List					
19153033	19153034	19153035	19153036	19153037	19153042
19153043	19153044	19153050	19153051	19153052	19153053
19153054	19153055	19153056	19153057	19153058	19153059
19153061	19153062	19153063	19153064	19153066	19154001
19154002	19154005	19154007	19154027	19154028	19154029
19154030	19154031	19154032	19154036	19154037	19154038
19154039	19154040	19154041	19154044	19154045	19154047
19154048	19154049	19154052	19154053	19154054	19154055
19154057	19154058	19154061	19154063	19154064	19154065
19154066	19154067	19155001	19155003	19155004	19155005
19155006	19155008	19155009	19155010	19155011	19155016
19155017	19155018	19155019	19155020	19155021	19155022

Table 3.2: A list of run number selected as good runs.

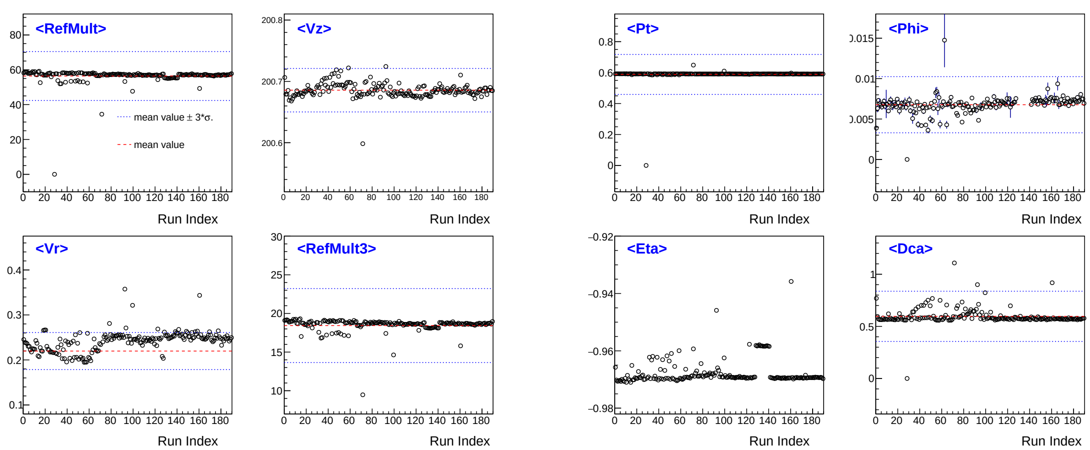

Figure 3.1.1: Run-by-run QA of event level variables, RefMult, V_z, V_r, and RefMult3, and track level variables, p_T, ϕ, η, and DCA. The red dashed line is the mean of run average of each variable. The blue dotted line indicates mean $\pm$ 3 times of standard deviation.

3.1.2 Event Selection

In the STAR fixed-target experiment, the vertex in beam (V_z [cm]) and radial direction (V_x, V_y [cm]) are required to be $199.5 < V_z < 202$ [cm] and 1.5 cm from the beam spot ($V_r = \sqrt{V_x^2 + (V_y + 2.)^2}$, $|V_r| < 1.5$ [cm]). The vertex distribution in radial and beam direction are shown in Fig. 3.1.2.

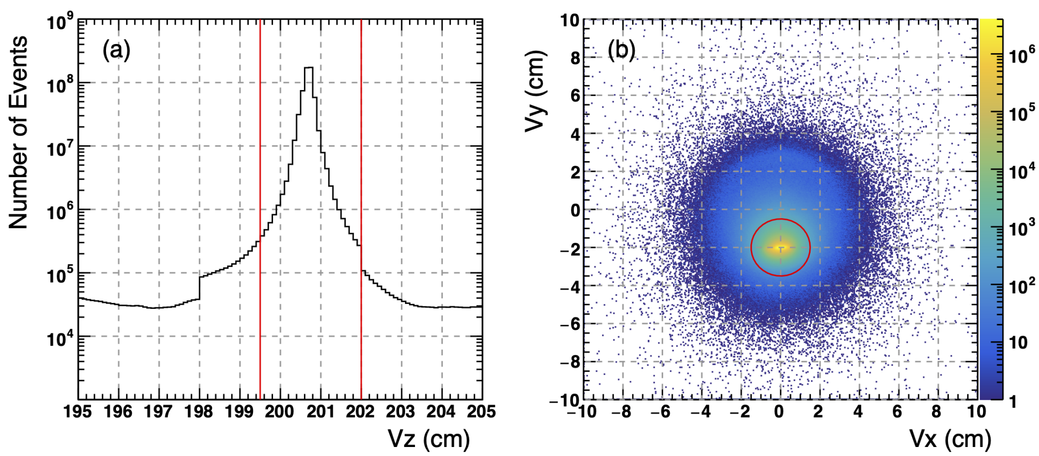

Figure 3.1.2: Panel (a): Vertex distribution (V_z cm) in beam direction. Panel (b): Vertex distribution (V_x and V_y) in radial direction.

3.1.3 Track Selection

To ensure track quality, number of hit points in TPC used for reconstructing track is required to be larger than 10 (nHitsFit > 10), a ratio number of hits points over number of maximum hits points are required to be larger than 0.51 and a DCA (Distance of Closest Approach) cut is required to be less than 3 cm.

Proton identification is mainly done by using TPC and TOF detectors. In TPC, particle identification is done by comparing energy loss to theoretical expectation value from Bichsel model [70]. Fig. 3.1.3 panel (a) shows TPC dE/dx vs rigidity(|p|/q, a ratio of total momentum over charge) distribution in which the red line means the theoretical expectation from Bichsel model. Instead of using energy loss per track length directly, a variable $n\sigma_p$ is defined as $\frac{1}{\sigma_R}\ln\frac{\mathrm{dE/dx_{measured}}}{\mathrm{dE/dx_{expectation}}}$ for convenience in which σ_R is momentum dependent dE/dx resolution. A cut $|n\sigma_p|<3.$ is placed to drop 0.3% of tracks which deviated from expectation value. Fig. 3.1.4 shows $|n\sigma_{proton}|$ for different total momentum slices. The proton purity is calculated

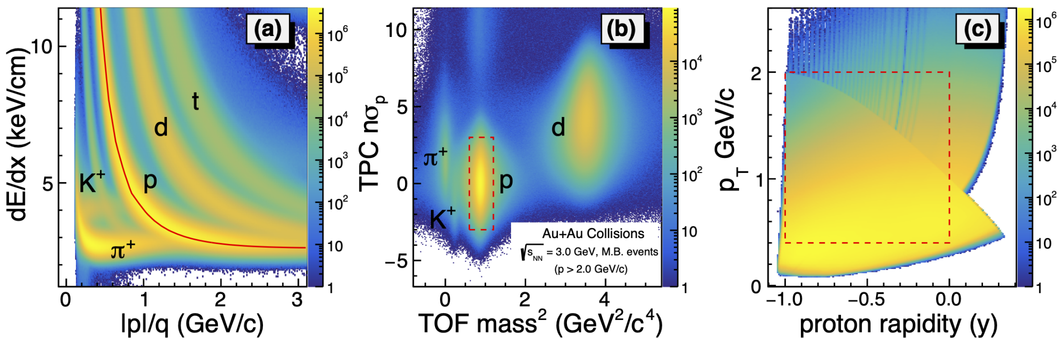

Figure 3.1.3: Panel (a): TPC Track energy loss (dE/dx (KeV/cm)) vs. momentum; pion, kaon, deuteron and triton are labeled. The proton Bethe-Bloch curve is plotted with red line. Panel (b): TPC $n\sigma_p$ vs. TOF $mass^2$. Panel (c): Transverse momentum (p_{T}) vs. proton rapidity.

by estimating the fraction of proton with removing contamination from other particles within +/- 3σ. In Fig. 3.1.4, proton purity is above 96% when total momentum in lab frame is less than around 2 GeV/c. For high momentum region, TOF detector is used for particle identification. The track velocity is calculated using the flight time of track from TOF and track length measured by TPC. Then track mass is calculated by $m = \sqrt{p * (1 - \beta^2)/\beta^2}$. Tracks with a momentum above 2 GeV/c require a mass-squared cut of $0.6 < m^2 < 1.2$ GeV^2/c^4. Fig. 3.1.3 panel (b) shows TPC $n\sigma_{proton}$ vs TOF mass square distribution with a momentum (in lab frame) cut $p > 2$ GeV/c applied. A red dashed box in Fig. 3.1.3 panel (b) is drawn to show the area for selected protons. Fig. 3.1.3 panel (c) shows transverse momentum (p_{T}) vs proton rapidity (y) in center of mass frame. The red dashed box indicates acceptance window ($0.4 < p_{\mathrm{T}} < 2.0$ GeV/c, $-0.9 < y < 0$) for the analysis.

3.2 Centrality Determination

Collision centrality is a measure of overlap of two colliding nucleus in beam direction. Experimentally charged particle reference multiplicity named FXTMult3 is used to define centrality. In this analysis in order to maximize centrality resolution, charged particles excluding protons (anti-protons are negligible, $\bar{p}/p \sim \exp(-2\mu_{\mathrm{B}}/T_{\mathrm{ch}}) < 10^{-6}$) are used in reference multiplicity within Full TPC acceptance $-2 < \eta < 0$ (η is defined as $\eta = 0.5 * \ln\left(\frac{E+p_z}{E-p_z}\right)$ in which p and p_z are total momentum and a fraction of total momentum in beam direction.) in lab frame. Protons and light nuclei are excluded to reduce self-correlation effect [72].

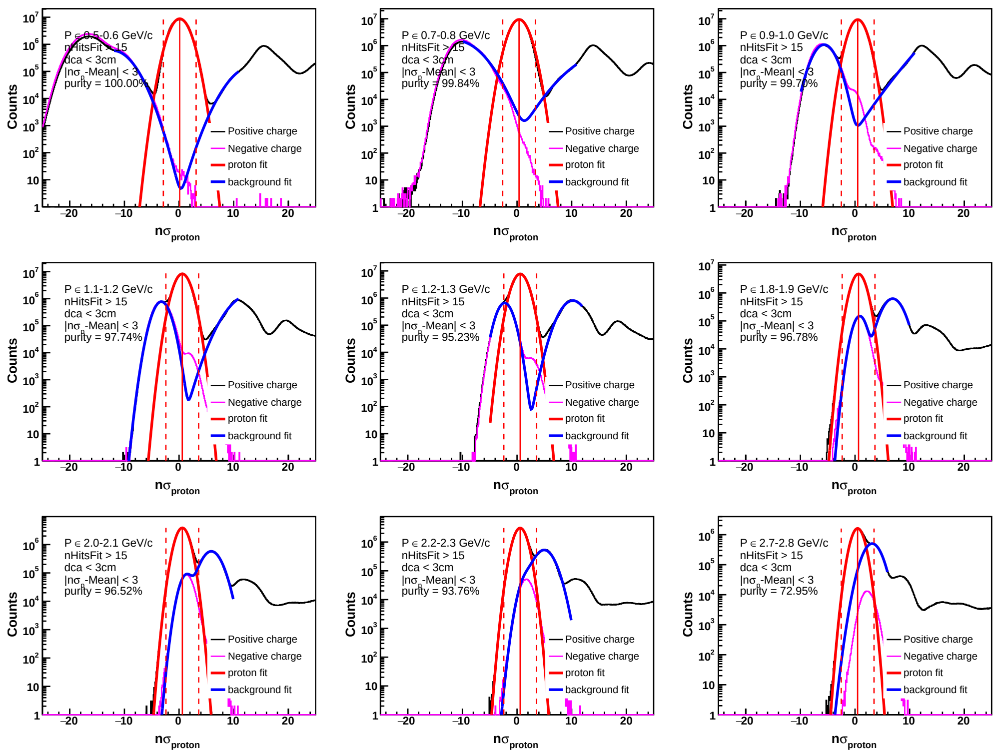

Figure 3.1.4: Proton $n\sigma_p$ distribution for each p_T window. Track quality cuts, nHits>15, DCA<3, are applied. Positive charged particles, negative charged particles are drawn as black and pink line, respectively. The peak around zero on x axis is for proton tracks which is fitted using Gaussian distribution while background are fitted using multi-Gaussian function.

The charged particle multiplicity distribution is divided into different percent, 0-5%, 5-10%, ..., 70-80%. There is a detector inefficiency for peripheral collisions event which is because of too small number of tracks to reconstruct an event. A simple Monte Carlo Glauber is usually used to simulate particle multiplicity distribution and fitted to data.

Monte Carlo Glauber (MCG) model is a widely used model in heavy-ion physics. It has simple assumptions:

1 Nucleons are randomly distributed by Wood-Saxon density distribution.
2 Nucleons travel in straight line trajectories.
3 Nucleons has only once inelastic collision at most.
4 A pair of nucleus will collide with each other if distance $< \sqrt{\sigma_{\text{inel}}^{\text{NN}}/\pi}$

The particle production is described by a two-component model, $dN/d\eta = (1-x)n_{\text{pp}}\frac{\langle N_{\text{part}}\rangle}{2} + x\langle N_{\text{coll}}\rangle$, in which x is hardness parameter, n_{pp} is particle production of p + p collisions, $\langle N_{\text{part}}\rangle$ is an average of number of participants, and $\langle N_{\text{coll}}\rangle$ is an average of number of binary collisions. Final multiplicity is then produced from binomial distribution given by

$$P_{\mu,k}(N) = \frac{\Gamma(N+k)}{\Gamma(N+1)\Gamma(k)} \cdot \frac{(\mu/k)^N}{(\mu/k+1)^{N+k}} \tag{3.2.1}$$

where μ is a mean value of particles generated from one source, and k corresponds to an inverse of a width of the distribution.

An additional parameter ϵ related to detector efficiency and acceptance is considered in Monte Carlo Glauber simulation. Then the simulated multiplicity distribution is then compared to data and performed a χ^2 test for multiplicity > 10. I scanned those parameters, n_{pp}, k, x, and ϵ, to find a minimum χ^2.

Fig. 3.2.1 shows Reference multiplicity distribution from data (black circles) and Monte Carlo Glauber simulation (red line). The vertical dashed lines indicate low edges in definition for centrality 0-5%, 5-10%, 10-20%, 20-30% which is shown in Table 3.3. From Fig. 3.2.1 it shows the Glauber simulation fits data well for multiplicity < 90. For multiplicity > 90 the large tail in data is due to pileup events. The pileup effect and corresponding correction will be discussed in Sec. 3.5.

3.3 Detector Efficiency Correction

TPC and TOF detectors are mainly used in particle identification, thus the efficiencies for both detectors need to be considered in cumulants calculation.

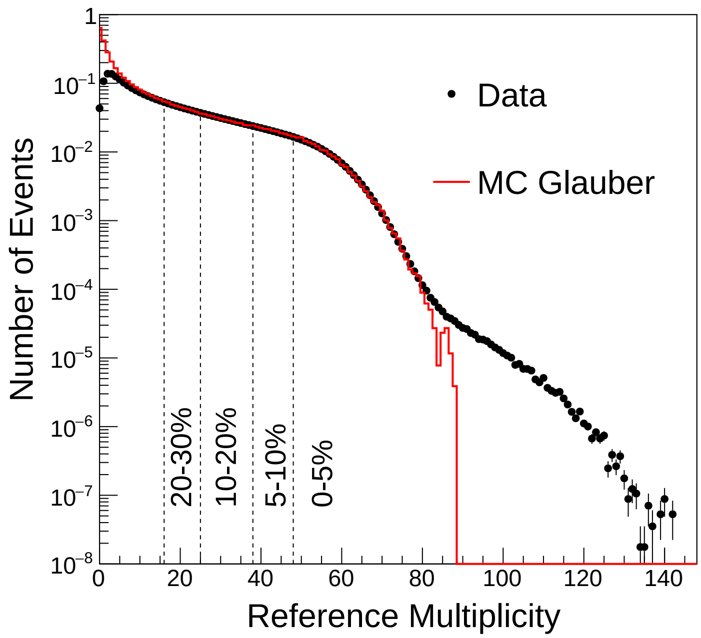

Figure 3.2.1: Reference multiplicity distribution (FXTMult3) in Au+Au collisions at $\sqrt{s_{\mathrm{NN}}} = 3\,\mathrm{GeV}$ (black circles), Glauber fitting (red line). The vertical dashed lines indicate different centrality bins.

Centrality (%)	$N_{ch} \geq$	$\langle N_{part} \rangle$	Pileup (%)
0–5	48	326(11)	2.32
5–10	38	282(8)	1.47
10–20	26	219(8)	1.28
20–30	16	157(7)	1.07
30–40	10	107(5)	0.90
40–50	6	70(5)	0.75
50–60	4	47(5)	0.64

Table 3.3: The uncorrected number (N_{ch}) of charged particles excluding protons within the pseudo-rapidity $-2 < \eta < 0$ used for the centrality selection for Au+Au collisions at $\sqrt{s_{NN}} = 3$ GeV. The centrality classes are expressed in % of total cross section. The lower boundary of the particle multiplicity (N_{ch}) is included for each centrality class. Values are provided for the average number of participants ($\langle N_{part} \rangle$) and pileup fraction. The fraction of pileup for each centrality bin is also shown in the last column. The averaged pileup fraction from the minimum biased collisions is determined to be 0.46%. Values in the (.) are associated systematic uncertainty.

The tracking efficiency in TPC is estimated by STAR Monte Carlo simulation [73]. Monte Carlo tracks are embedded into real tracks. Then all tracks are put into Geant simulation and going through TPC track re-construction procedure. The efficiency is estimated by counting how many Monte Carlo tracks are re-constructed compared to initial embedded ones.

The efficiency for TOF currently is done by a data-driven way. The matching efficiency for tracks of TOF to TPC is considered. Track in TOF that has one or more matching track in TPC is considered as one matched track. The efficiency can be described by

$$\epsilon_{matching} = \frac{N_{matched}}{N} \tag{3.3.1}$$

where $\epsilon_{matching}$, $N_{matched}$, and N are is TOF matching efficiency, number of tracks in TOF that are matched to TPC and total number of tracks detected in TOF.

According to the purity study shown in Fig. 3.1.4 that using only TPC for particle identification, proton purity is above around 95% for total momentum $p > 2$ GeV/c in lab frame. For higher momentum, the TOF PID is used to ensure high purity sample selected.

The efficiency correction of cumulants consider detector efficiency is Binomial responded. In the

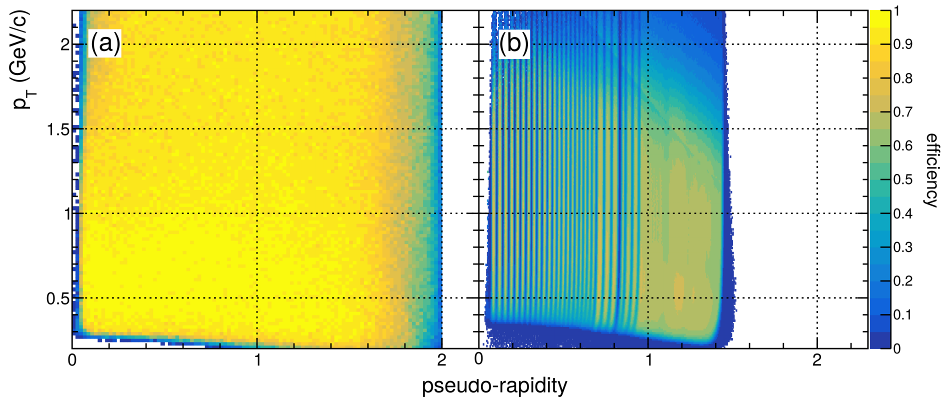

Figure 3.3.1: TPC tracking efficiency (a) and TOF matching efficiency (b) as a function of transverse momentum p_T (GeV/c) and pseudo-rapidity η.

previous analysis [57, 74] of BES-I data, the conventional method [75] considers two efficiency bins for single particle. For example, the efficiency value for lower p_T ($0.4 < p_T < 0.8$ GeV/c) bin and higher p_T ($0.8 < p_T < 2.0$ GeV/c) bin are used. The efficiency are integrated over rapidity. To handle infinite efficiency bins, a track-by-track efficiency correction method [76, 77] is applied in proton cumulant analysis. Fig. 3.3.1 shows TPC (a) and TOF efficiency (b) as a function of p_T and pseudo-rapidity η. It is seen that the efficiency value is not uniform specifically for TOF. There are efficiency gaps because of gaps in TOF modules.

3.4 Centrality Bin Width Correction

In order to show results and reduce the volume fluctuation effect (at 3 GeV reference multiplicity is not a good quantity to correspond to collision volume, but CBWC is still necessary. I'll discuss this in Sec. 3.6.) the centrality bin width correction method [72] is used to extract proper averages of cumulants and cumulant ratios at each centrality bin. The number of events for each reference multiplicity is used as weight. The method is described by

$$C = \frac{\sum_i^n C_i N_i}{\sum_i^n N_i} \tag{3.4.1}$$

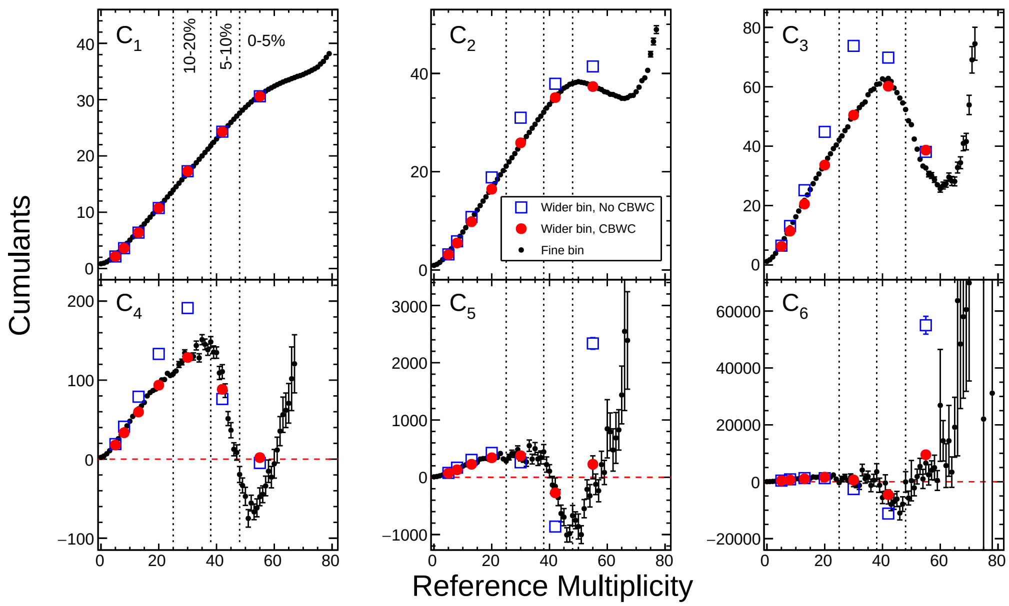

Figure 3.4.1: Proton cumulants up to 6$^{\text{th}}$ order as a function of reference multiplicity in Au+Au collisions at $\sqrt{s_{\text{NN}}} = 3$ GeV within acceptance of $-0.5 < y < 0$ and $0.4 < p_{\text{T}} < 2.0$ GeV/c. Centrality binned (wider bin in plot) results with and without centrality bin width correction are shown with red circles and blue squares, respectively. The cumulants as a function of reference multiplicity are shown with black circles. The vertical dashed lines indicate the centrality classes, from right to left, $0-5\%$, $5-10\%$, $10-20\%$, $20-30\%$, $30-40\%$, $40-50\%$ and $50-60\%$.

where C_i, C, and N_i are average of cumulant at each centrality bin, cumulant at reference multiplicity bin, and number of events at reference multiplicity bin.

Fig. 3.4.1 shows proton cumulants up to 6$^{\text{th}}$ order as a function of reference multiplicity in Au+Au collisions at $\sqrt{s_{\text{NN}}} = 3\,\text{GeV}$ within acceptance of $-0.5 < y < 0$ and $0.4 < p_{\text{T}} < 2.0\,\text{GeV}/c$. The results with CBWC (red circles) follow the reference multiplicity dependence (black circles) while the results without CBWC (blue squares) are exaggerated. This is because calculating cumulants in wider centrality bin means performing calculation on the integral of proton distribution from a wide range of initial collision geometry. The fluctuation of various collision volume is also included in the calculation of proton multiplicity distribution. A few more words on the volume fluctuation, as shall be seen in Sec. 3.6 that reference multiplicity may not be a good reference to initial collision geometry. A better reference quantity to collision geometry together with the CBWC should mostly reduce volume fluctuation.

3.5 Pileup Effect

Pileup event is defined as an event contains more than one single-collision event. Pileup events are because two or more collisions occur within a small time and space interval thus they are identified by detector as one event, thus their particle multiplicity are simple combination of two single-collision events. An evident signature of pileup events is a large tail shown in high end of reference multiplicity distribution. As shown in Fig. 3.2.1, the long tail (black circles) for reference multiplicity from 90 to 140 are mainly pileup events.

In the high luminosity fixed-target experiment, pileup events are large compared to collider mode, that makes the pileup a non-negligible effect in higher-order cumulant analysis in fixed-target experiment. In experiment, according to different response time of pileup events to sub-detectors, those pileup events are usually removed by clean cuts. In the 3 GeV analysis proton cumulant analysis, I used a pileup correction method [78] for cumulants to correct the effect brought by pileup events and used an unfolding approach [79] to estimate pileup fraction which is a necessary input for pileup correction.

3.5.1 Pileup Correction

The cumulant pileup correction method proposed in Ref. [78] assumed that pileup events are given by the superpositions of two independent single-collision events.

Let $P_m(N)$ be a probability distribution function to find one event with N particles at reference multiplicity m. Throughout this section I suppose that pileup events are formed by independent superposition of two single-collision events with the probability α. Then $P_m(N)$ can be rewritten as

$$P_m(N) = (1-\alpha_m)P_m^{\mathrm{t}}(N) + \alpha_m P_m^{\mathrm{pu}}(N) \tag{3.5.1}$$

where $P_m^{\mathrm{t}}(N)$ and $P_m^{\mathrm{pu}}(N)$ are probability distribution functions for single-collision event and pileup event respectively. Pileup events at multiplicity m can be decomposed into sub-pileup events whose multiplicity satisfies $m = i + j$. By looping all possible combinations of i and j which satisfies $m = i + j$, probability distribution function for pileup events is obtained and written as

$$P_m^{\mathrm{pu}}(N) = \sum_{i,j} \delta_{m,i+j} w_{i,j} P_{i,j}^{\mathrm{sub}}(N) \tag{3.5.2}$$

and

$$P_{i+j}^{sub}(N) = \sum_{N_i,N_j} \delta_{N,N_i+N_j} P_i^t(N_i) P_j^t(N_j) \tag{3.5.3}$$

where $w_{i,j}$ is the probability to observe a sub-pileup event among all pileup events at multiplicity m and $P_{i,j}^{sub}(N)$ represents the probability distribution of N in the sub-pileup events labeled by (i, j). i and j commutes in $w_{i,j}$ which gives $w_{i,j} = w_{j,i}$. Exhausting all combinations of i and j there should be

$$\sum_{i,j} \delta_{m,i+j} w_{i,j} = 1. \tag{3.5.4}$$

I also consider a multiplicity distribution $T(m)$ used for centrality determination. The pileup events at the m-th multiplicity bin are then decomposed into two sub-pileup events which satisfies $m = i + j$. Then I get [78]

$$w_{i,j} = \frac{\alpha T(i)T(j)}{\sum_{i,j} \delta_{m,i+j} \alpha T(i)T(j)}, \tag{3.5.5}$$

$$\alpha_m = \frac{\alpha \sum_{i,j} \delta_{m,i+j} T(i)T(j)}{(1-\alpha)T(m) + \alpha \sum_{i,j} \delta_{m,i+j} T(i)T(j)}. \tag{3.5.6}$$

The Equation 3.5.5 defines the weight of sub-pileup events having multiplicities i and j while Eq. 3.5.6 represents the pileup fraction at m-th multiplicity bin.

From Eqs. 3.5.1, 3.5.2, and 3.5.3 the moment generating function at multiplicity m can be expressed as

$$\begin{aligned} G_m(\theta) &= \sum_N e^{N\theta} P_m(N) \\ &= (1-\alpha_m) G_m^t(\theta) + \alpha_m \sum_{i,j} \delta_{m,i+j} w_{i,j} G_{i,j}^{sub}(\theta), \end{aligned} \tag{3.5.7}$$

with

$$G^{sub}_{i,j}(\theta) = G^{t}_{i}(\theta)G^{t}_{j}(\theta), \tag{3.5.8}$$

where $G^{t}_{m}(\theta) = \sum_{N} e^{N\theta} P^{t}_{m}(N)$ is the moment generating function of $P^{t}_{m}(N)$. The rth order moment of the observed distribution $P_m(N)$ is given by

$$\begin{aligned} \langle N^r \rangle_m &= \sum_{m} N^r P_m(N) = \frac{d^r}{d\theta^r} G(\theta)|_{\theta=0} \\ &= (1-\alpha_m)\langle N^r \rangle^{t}_{m} + \alpha_m \sum_{i,j} \delta_{m,i+j} w_{i,j} \langle N^r \rangle^{sub}_{i,j}, \end{aligned} \tag{3.5.9}$$

with $\langle N^r \rangle^{t}_{m} = \sum_{N} N^r P^{t}_{m}(N)$ and

$$\langle N^r \rangle^{sub}_{i,j} = \sum_{N} N^r P^{sub}_{i,j}(N) = \sum_{k=0}^{r} \binom{r}{k} \langle N^{r-k} \rangle^{t}_{i} \langle N^{k} \rangle^{t}_{j}. \tag{3.5.10}$$

Equation 3.5.10 can be alternatively written by cumulant in a compact form

$$\langle N^r \rangle^{sub}_{i,j,c} = \langle N^r \rangle^{t}_{i,c} + \langle N^r \rangle^{t}_{j,c}, \tag{3.5.11}$$

where $\langle N^r \rangle^{sub}_{i,j,c}$ and $\langle N^r \rangle^{t}_{j,c}$ are the cumulants of sub-pileup and true distributions, respectively. True moments are expressed recursively in terms of the measured moments at the lower multiplicity bins by solving Eqs. 3.5.9 and 3.5.10:

$$\langle N^r \rangle^{\mathrm{t}}_{m} = \frac{\langle N^r \rangle_m - \alpha_m \beta^{(r)}_{m}}{1-\alpha_m + 2\alpha_m w_{m,0}}, \tag{3.5.12}$$

with

$$\beta^{(r)}_{m} = \mu^{(r)}_{m} + \sum_{i,j>0} \delta_{m,i+j} w_{i,j} \langle N^r \rangle^{\mathrm{sub}}_{i,j}, \tag{3.5.13}$$

and

$$\mu^{(r)}_{m} = \begin{cases} 2w_{m,0} \sum_{k=0}^{r-1} \binom{r}{k} \langle N^{r-k} \rangle^{\mathrm{t}}_{0} \langle N^{k} \rangle^{\mathrm{t}}_{m} & (m>0), \\ \sum_{k=1}^{r-1} \binom{r}{k} \langle N^{r-k} \rangle^{\mathrm{t}}_{0} \langle N^{k} \rangle^{\mathrm{t}}_{0} & (m=0), \end{cases} \tag{3.5.14}$$

where $\langle N^r\rangle_m^t$ and $\langle N^r\rangle_m$ represent rth order true and measured moments at mth multiplicity bin, respectively. With true moments of each order obtained, one then can express true cumulants in terms of true moments. As can be seen from Eqs. (3.5.5)–(3.5.14), the necessary information to perform the pileup corrections are true multiplicity distribution $T(m)$ and pileup fraction α.

In real experiments, we can only measure the multiplicity distributions including pileup events, to extract the true multiplicity distribution for single-collision events one naive way is to use Monte-Carlo Glauber and particle production model to fit the measured multiplicity distribution. As the Glauber model is widely used for centrality determination it is firstly tried.

3.5.2 Pileup Correction Validation Using UrQMD Model

To validate the pileup correction method as well as the unfolding approach which will be shown in Sec. 3.5.3 I use single-collision events from UrQMD model [58, 59] to simulate pileup events and test the correction method. I show in this section a closure test as well as a realistic case for which single-collision distribution and pileup fraction is extracted from Glauber fit.

The UrQMD code I used is of version 3.4 and configured as the standard cascade mode. Around 80 million events are generated in Au+Au collisions at $\sqrt{s_{\mathrm{NN}}} = 3\,\mathrm{GeV}$ with the impact parameter from 0 to 15 fm. To simulate pileup events in experiment I randomly added up two UrQMD events under a predefined pileup fraction ($\alpha = 0.5\%$) to produce pileup UrQMD events. Protons within rapidity and transverse momentum of $-0.5 < y < 0$ and $0.4 < p_{\mathrm{T}} < 2.0$ (GeV/c) are selected for cumulant calculations of proton multiplicity distributions. Collision centrality is defined by dividing reference multiplicity distribution into different percent (0-5%, 5-10%, 10-20%, ..., 70-80%). Reference particles are using $\pi^{\pm}$ and $K^{\pm}$ with pseudo-rapidity $|\eta| < 1$. where (anti)protons are excluded to avoid self-correlation effect [72].

Proton cumulants and their ratios up to 4$^{\text{th}}$ order are calculated for several data sets. Fig. 3.5.2 shows cumulants and their ratios as a function of pileup fraction $1\% < \alpha < 10\%$ in which the black points are calculation for pure UrQMD data, the black squares are calculation for Pileup-UrQMD data in which pileup events are simulated and added in pure UrQMD events, the red stars are a closure test in which pileup correction is performed using correction parameters directly given by UrQMD data, and the blue circles are calculation with pileup correction parameters determined by Glauber model. Comparing black squares to black circles, it is seen that cumulants and their ratios are enhanced by pileup events. It is worth noting that the cumulant ratio C_4/C_2 even changes its sign from negative to positive then goes above unity when increasing pileup probability α. Comparing red stars and blue circles to black circles, it is found that with a precise estimation of α, the pileup correction works well for pileup probability up to 10%. While due to

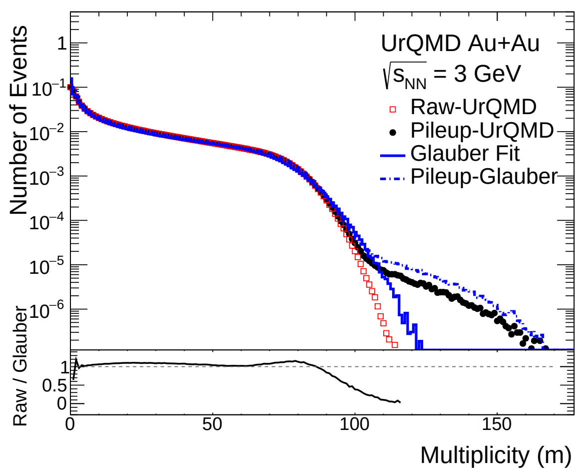

Figure 3.5.1: Reference multiplicity distribution (red squares) in Au+Au collisions at $\sqrt{s_{\mathrm{NN}}} = 3\,\mathrm{GeV}$ from UrQMD model. Reference particles are using $\pi^{\pm}$ and $K^{\pm}$ with pseudo-rapidity $|\eta| < 1$. The black circles are reference multiplicity distribution with pileup events which are simulated using pure UrQMD events under a pileup fraction $\alpha = 0.5\%$. The blue line is Monte-Carlo Glauber fit to Pileup-UrQMD distribution (black circles) while the blue dashed line is a best fit to Pileup-UrQMD distribution using single-collision distribution from Monte-Carlo Glauber fit(blue line). The black line in lower panel is a ratio of Raw-UrQMD distribution over distribution from Glauber fit.

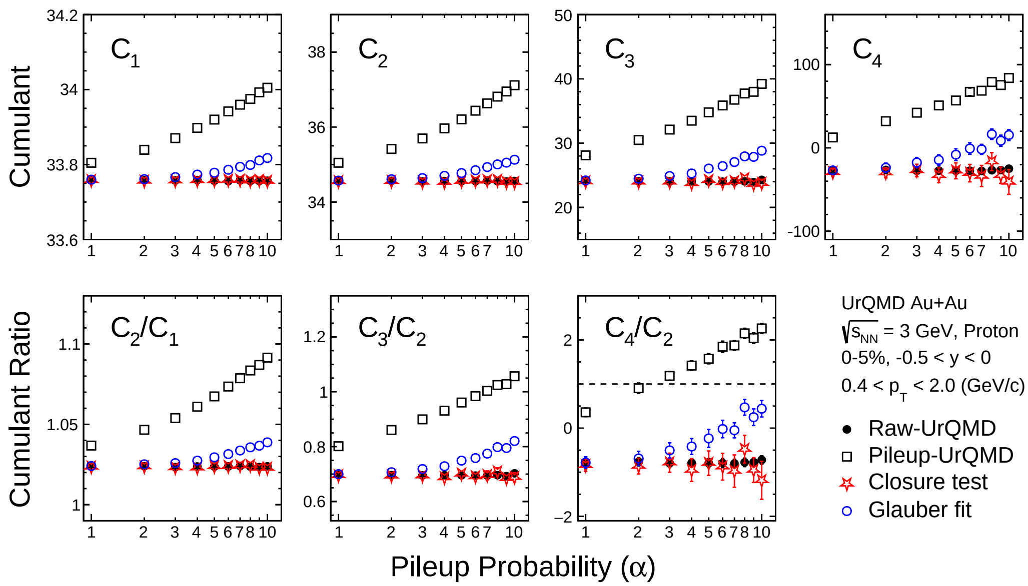

Figure 3.5.2: Pileup level dependence of cumulants and cumulant ratios up to 4$^{\text{th}}$ order in most central 5% Au+Au collisions at $\sqrt{s_{\text{NN}}} = 3$ GeV from UrQMD model. The results from default UrQMD are shown with black circles while results with pileup events are shown with black squares. The red stars and blue circles are results with pileup correction based on UrQMD and Glauber model, respectively.

the imperfect Glauber fit to Pileup-UrQMD data, the calculations (blue circles) using parameters extracted by the fit show deviation from true results (black circles). From above test, we see that pileup correction works well in the ideal case and the effectiveness mostly depends on how precise the pileup probability is estimated.

3.5.3 Pileup Correction with Unfolding Approach

To extract pileup probability to a higher precision, a model independent method named unfolding approach [80, 79] is tested and used in data analysis. The unfolding approach [80] was originally developed to reconstruct particle multiplicity distribution in terms of non-binomial detector efficiency. It is found the similar methodology is applicable in pileup correction. As discussed in Sec. 3.5.2, pileup corrections depend on how one can precisely extract the true multiplicity distribution for single-collision events. The issue is that the Glauber and particle production models, which are commonly used for centrality determination, cannot fit even the UrQMD data perfectly. A model independent way is necessary to make sure the quality of pileup corrections. In this section, I'll show the procedures to extract a precise pileup parameter using unfolding approach and a test on cumulants of this approach.

Figure 3.5.3 depicts a flowchart for the unfolding procedure. In real experiments, the multiplicity distribution is measured with the pileup events on top of the single-collision events as shown in the left row in Fig. 3.5.3. ”True” and ”Measured” in the figure represent the multiplicity distributions for single-collisions and inclusive distributions for both single-collisions and pileup events. They are labeled as ”(a) UrQMD experiment true” and ”(b) UrQMD experiment measured”, respectively. Both are related via a numerical process to generate pileup events called ”Pileup Filter”, which is defined as an independent superposition of two single-collision events with probability α for simplicity. Similarly, we suppose Monte-Carlo samples labeled as ”(c) toy-MC true” and ”(d) toy-MC measured”. They are also related via the same pileup filter between (a) and (b). In the rest of this paper, samples in the top row will be referred to as ”true coordinates”, while the bottom row will be ”measured coordinates”. The goal of the unfolding approach is to reconstruct (a) starting from (c). Detailed procedures are shown below:

0 Generate (a) UrQMD-experiment and (b) UrQMD-measured samples. They correspond to raw-UrQMD and pileup-UrQMD distributions in Sec. 3.5.2.

1 Generate a (c) toy-MC distribution based on the Glauber model.

2 The pileup filter is applied to (c) to get (d) toy-MC measured distribution.

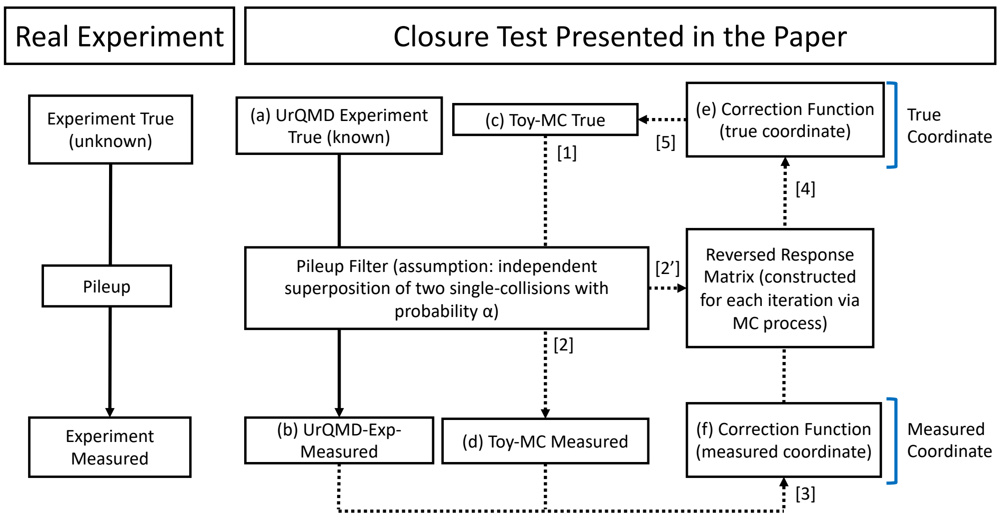

Figure 3.5.3: Flowcharts in unfolding to extract the true multiplicity distribution. The dotted arrows show the procedures repeated for iterations.

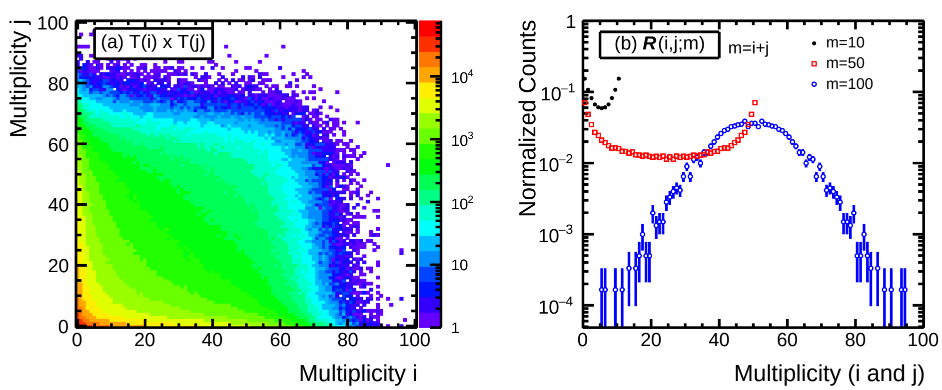

Figure 3.5.4: (Left) Correlations between two independence multiplicity distribution in pileup events. (Right) Response matrices for 0th, 50th, and 100th iteration.

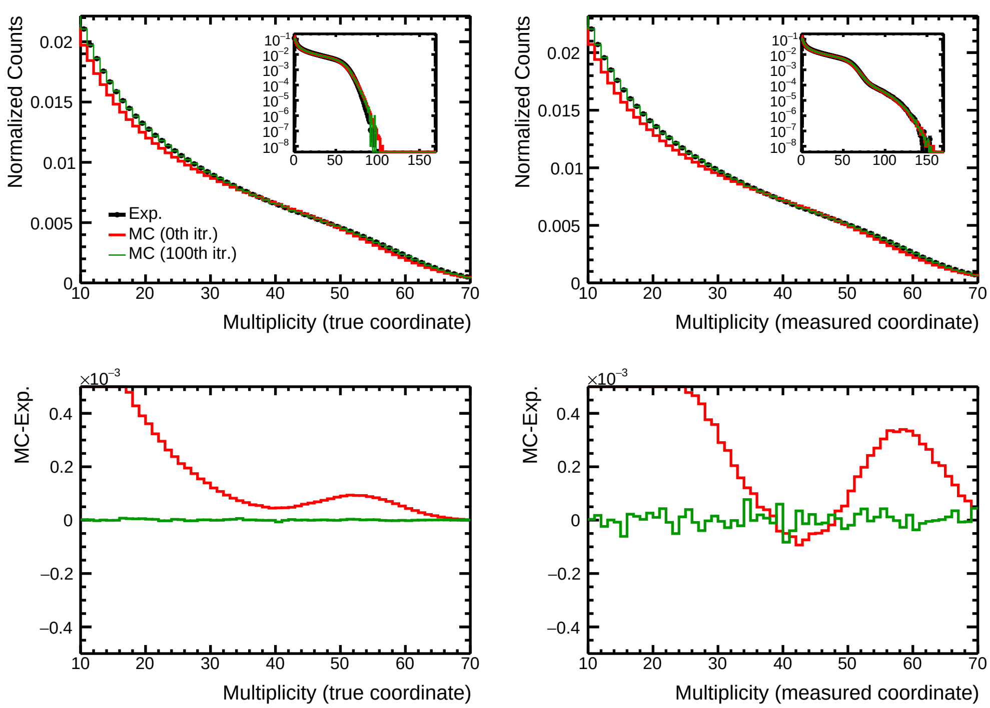

Figure 3.5.5: (Top) Multiplicity distributions for UrQMD, Glauber fit, and MC samples at 100th iteration. (Bottom) Difference between UrQMD and MC samples as a function of multiplicity. Left-hand side panels are for the true coordinates, while right-hand side panels are for the measured coordinates. The range of the x-axis is limited from 10 to 70 for illustration purpose.

3 During the MC process from **1** to **2**, I compute the reversed response matrices, $\boldsymbol{R}$, numerically as shown in Fig. 3.5.4. Note that any inversion procedure is not necessary here.

4 The correction function is determined by subtracting (b) from (d). It represents the difference between UrQMD-experiment and toy-MC distributions in the measured coordinates. See lower panels in Fig. 3.5.5.

5 The response matrix $\boldsymbol{R}$ is multiplied to (f) to get (e) the correction functions in the true coordinates.

6 By adding (e) to (c), the toy-MC distribution is modified to be closer to (a).

7 Repeat **1–6** until the correction functions become close enough to zero.

The response matrices in **3** are defined as

$$T(i,j) = \sum_{i,j} \delta_{m;i,j} R(i,j;m)\tilde{T}(m), \tag{3.5.15}$$

where $\tilde{T}(m)$ represents the probability distribution function of multiplicity in pileup events at measured coordinates, and $T(i,j)$ is a correlation between two multiplicities which forms pileup events. $P(i,j)$ and $R(i,j;m)$ are shown in Fig. 3.5.4. Distributions in Fig. 3.5.4-(b) are projections of Fig. 3.5.4-(a) onto a diagonal plane for $m = 10$, 50, and 100 with $m = i + j$. The response matrices relate the multiplicity m observed in pileup events at measured coordinates and their original multiplicities from two single-collision events, i and j at true coordinates. Note that the response matrices are determined during the numerical process of the pileup filter for each iteration. Fig. 3.5.5 shows multiplicity distributions and correction functions as a function of multiplicity for true and measured coordinates, respectively. The initial distribution of MC samples are taken from the best fit of the Glauber model to the UrQMD-experiment distribution in the true coordinates. Nevertheless, there are large differences from the UrQMD-experiment distribution as can be seen in the correction functions. After 100 iterations, the correction functions are found to be flat, which indicates that the multiplicity distribution for MC samples are successfully unfolded to UrQMD-experiment distributions. The resulting multiplicity distribution for the true coordinates can be used to determine the parameters for pileup corrections according to Eq. 3.5.5.

In our simulations the preseted value of pileup probability α is used for the unfolding approach. In real experiments, the pileup probability can be basically calculated from the beam rates and thickness of the target material. To determine this more precisely, the unfolding approach needs to be repeated by varying the pileup probability to find the best parameter which yields the smallest values of χ^2/NDF.

Let us then move to the pileup corrections on cumulants. The multiplicity distribution for the true coordinate after 100 iterations is used to define the parameters for pileup corrections. Results are shown in Fig. 3.5.6 for up to the 4$^{\text{th}}$-order cumulant as a function of centrality. Due to the effect of pileup events, the results at the most central collisions deviate from the true value of cumulants. The results of pileup correction using Glauber fits, however, still deviate from the true cumulants, which is because the Glauber fit is not perfect enough to describe the multiplicity distribution in UrQMD, as discussed in Sec. 3.5.2. We then apply pileup corrections with correction parameters determined by the unfolding approach. The results are consistent with true values of cumulants in the most central collisions. Therefore, it is concluded that our unfolding approach works well to determine the correction parameters for pileup corrections. In this work, we simulated pileup events by the superposition of two single-collision events, in fact the pileup events merged from more than two single-collision events can be also studied. In the unfolding approach the MC samples are taken from the best fit of the Glauber model to the UrQMD-experiment distributions. In principle, MC samples can start from any distributions like a flat distribution, but we propose to start from the distribution close to the experimental data to avoid possible systematics on the initial conditions of the MC samples.

Figure 3.5.6 shows cumulants and their ratios up to the 4$^{\text{th}}$-order as a function of centrality. Due to the effect of pileup events, the results at the most central collisions deviate from the true value of cumulants. The results of pileup correction using Glauber fits, however, still deviate from the true cumulants, which is because the Glauber fit is not perfect enough to describe the multiplicity distribution in UrQMD. We then apply pileup corrections with correction parameters determined by the unfolding approach. The results are consistent with true values of cumulants in the most central collisions. Therefore, it is concluded that our unfolding approach works well to determine the correction parameters for pileup corrections. In this work, we simulated pileup events by the superposition of two single-collision events, in fact the pileup events merged from more than two single-collision events can be also studied. In the unfolding approach the MC samples are taken from the best fit of the Glauber model to the UrQMD-experiment distributions. In principle, MC samples can start from any distributions like a flat distribution, but we propose to start from the distribution close to the experimental data to avoid possible systematics on the initial conditions of the MC samples.

3.5.4 Pileup Correction on Data

In Fig. 3.5.7, the left panel shows reference multiplicity distribution for data (black circles), unfolded single-collision distribution (blue line), and pileup events distribution (red line) which is subtracted from

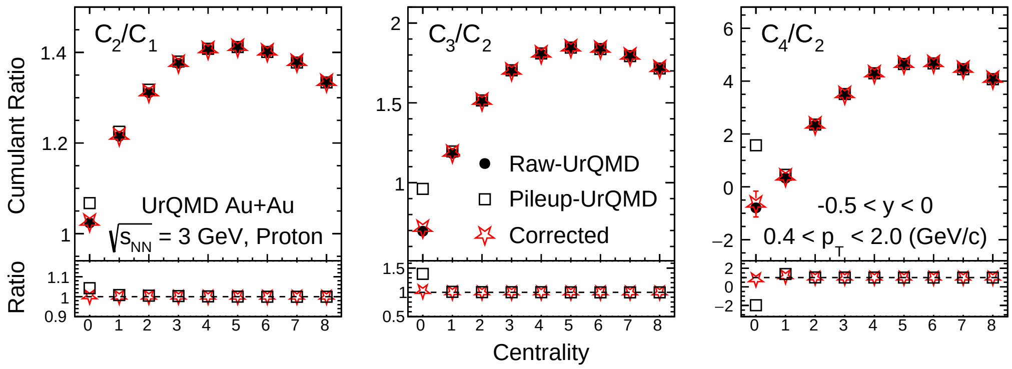

Figure 3.5.6: Centrality dependence of cumulants and cumulant ratios up to 4^{th}-order in Au+Au collisions at $\sqrt{s_{\text{NN}}} = 3\,\text{GeV}$ from UrQMD model. The results from default UrQMD are shown with black circles while results with pileup events are shown with black squares. The red stars are results with pileup correction using unfolding approach.

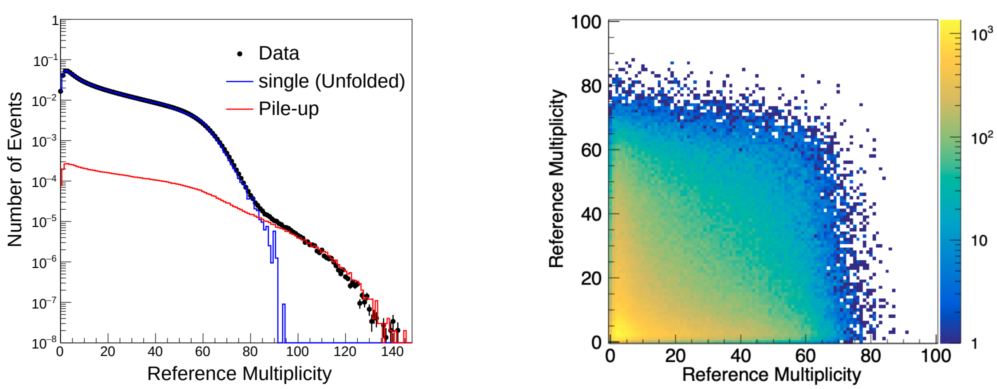

Figure 3.5.7: Left panel: Reference multiplicity distribution in Au+Au collisions at $\sqrt{s_{\text{NN}}} = 3\,\text{GeV}$. The data is shown with black circles while the unfolded single-collision distribution is shown with blue line. The red line represents pileup events distribution which is subtracted from data and unfolded distribution. Right panel: Correlation of single collision reference multiplicity distribution which forms pileup events. The single collision distribution is obtained by unfolding approach.

data and single-collision distribution. Then the pileup probability is also determined which is 0.46% ± 0.09% of all events and 2.10% ± 0.40% in the 0-5% centrality class. Right panel of Fig. 3.5.7 shows a correlation distribution of unfolded single-collision reference multiplicity.

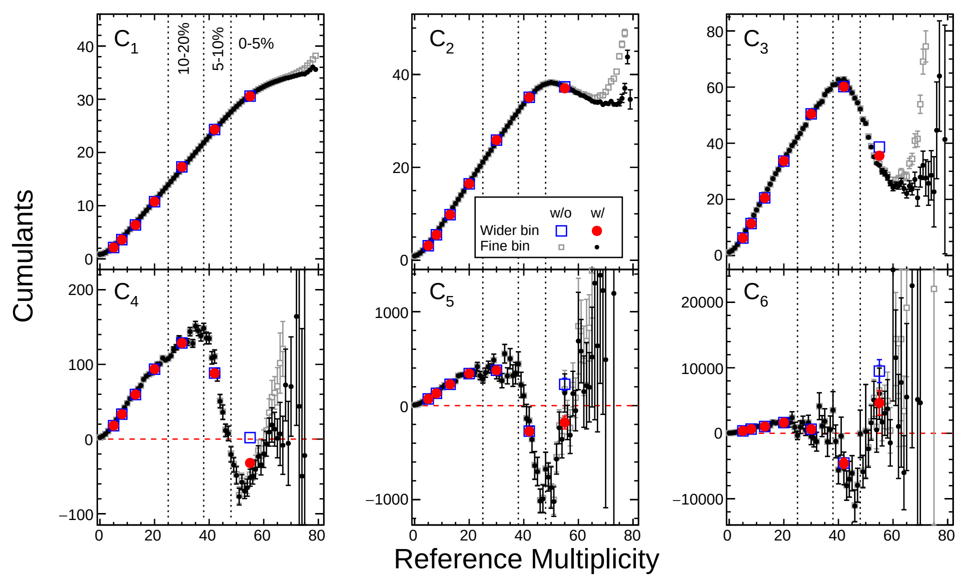

Figure 3.5.8: Proton cumulants up to 6$^{\text{th}}$-order as a function of reference multiplicity in Au+Au collisions at $\sqrt{s_{\rm NN}}$ = 3 GeV within acceptance of $-0.5 < y < 0$ and $0.4 < p_{\rm T} < 2.0$ GeV/c. Centrality binned (wider bin in plot) results with and without pileup correction are shown with red circles and blue squares, respectively. The cumulants with and without pileup correction as a function of reference multiplicity are shown with black circles and black squares, respectively. Same to Fig. 3.4.1 the vertical dashed lines indicate the centrality classes.

Figure 3.5.8 shows proton cumulants up to 6$^{\text{th}}$-order as a function of reference multiplicity in Au+Au collisions at $\sqrt{s_{\rm NN}}$ = 3 GeV within acceptance of $-0.5 < y < 0$ and $0.4 < p_{\rm T} < 2.0$ GeV/c. The pileup correction is done for each reference multiplicity bin (black circles) compared to that without correction (black squares). Centrality binned (wider bin in plot) results with and without pileup correction are then obtained by performing CBWC. Comparing results with and without pileup correction for both fine bin and wider bin, it is seen only cumulants from top 5% centrality class are modified. This is seen in UrQMD calculation shown in Fig. 3.5.6. Similar to Fig. 3.5.8, Fig. 3.5.9 shows cumulant ratios up to 6$^{\text{th}}$-order. A

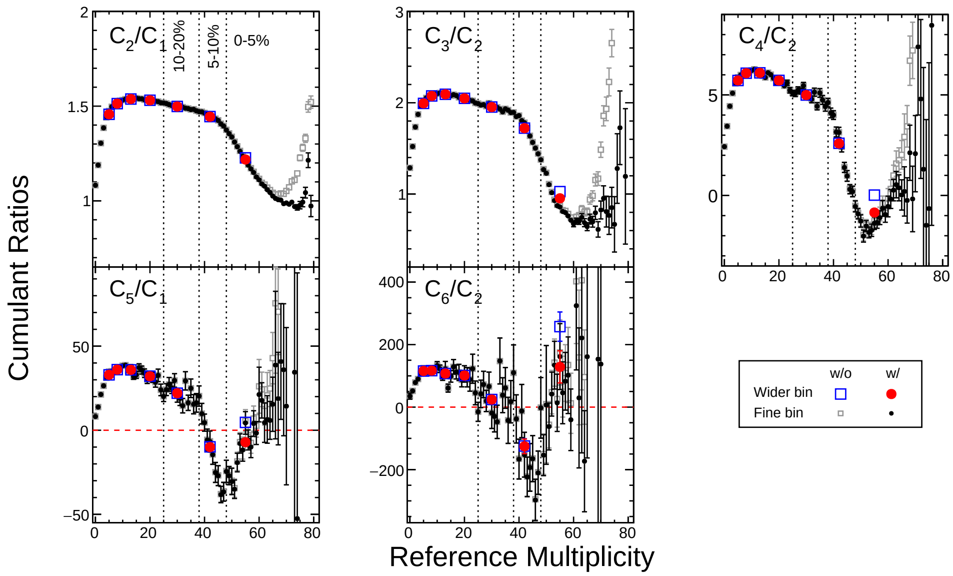

Figure 3.5.9: Proton cumulants up to 6$^{\text{th}}$-order as a function of reference multiplicity in Au+Au collisions at $\sqrt{s_{\text{NN}}} = 3\,\text{GeV}$ within acceptance of $-0.5 < y < 0$ and $0.4 < p_{\text{T}} < 2.0\,\text{GeV}/c$. The markers in plot are same to Fig. 3.5.8.

similar conclusion is drawn from the comparison of results with and without pileup correction that only most central centrality are affected by pileup effect.

Figure 3.5.10 shows cumulants and cumulant ratios as a function of $\langle N_{\mathrm{part}} \rangle$ up to 6^{th}-order in Au+Au collisions at $\sqrt{s_{\mathrm{NN}}} = 3\,\mathrm{GeV}$ within kinematic acceptance $-0.5 < y < 0$ and $0.4 < p_{\mathrm{T}} < 2.0\ \mathrm{GeV}/c$. The $\langle N_{\mathrm{part}} \rangle$ is the average of N_{part} from Glauber Monte Carlo simulation. From a large N_{part} to a low value it represents 0-5%, 5-10%, ⋯, 50-60%. Results without or with pileup correction are shown with red circles and black squares, respectively. The x axis is the average of number of participating nucleons N_{part}. From the comparison of results with and without pileup correction, it seems that result at most central centrality is modified. It's worth noting that C_4/C_2 at most 5% centrality even changes sign from positive to negative. Fig. 3.5.11 shows centrality dependence of correlation functions and their ratios up to 6^{th}-order in Au+Au collisions at $\sqrt{s_{\mathrm{NN}}} = 3\,\mathrm{GeV}$ within kinematic acceptance $-0.5 < y < 0$ and $0.4 < p_{\mathrm{T}} < 2.0\ \mathrm{GeV}/c$. A similar conclusion can be draw from the comparison of results with and without pileup correction.

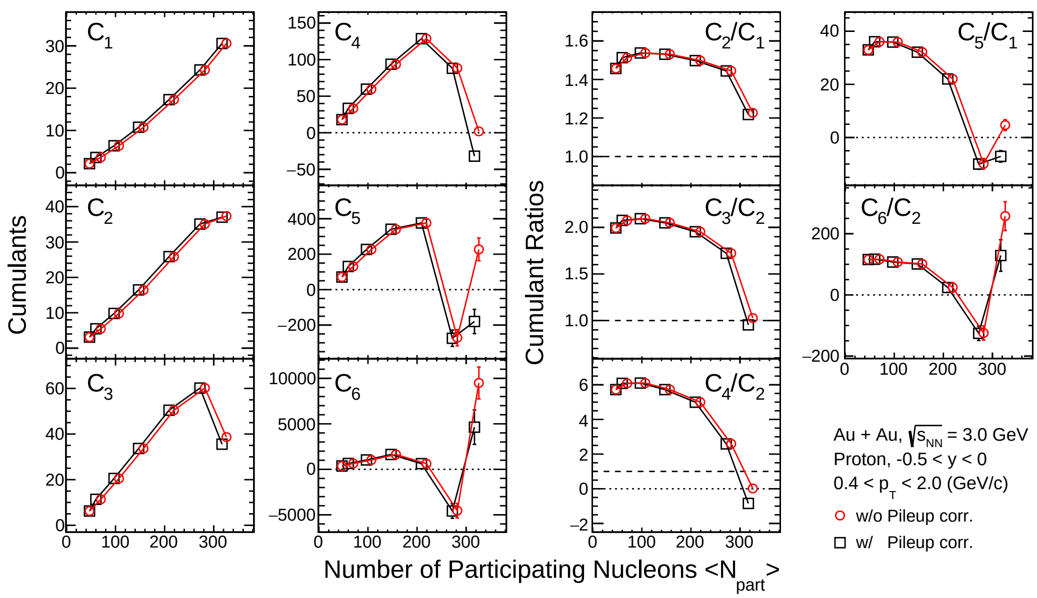

Figure 3.5.10: Centrality dependence of cumulants and cumulant ratios up to 6^{th}-order in Au+Au collisions at $\sqrt{s_{\mathrm{NN}}} = 3\,\mathrm{GeV}$ within kinematic acceptance $-0.5 < y < 0$ and $0.4 < p_{\mathrm{T}} < 2.0\ \mathrm{GeV}/c$. Results without or with pileup correction are shown with red circles and black squares, respectively.

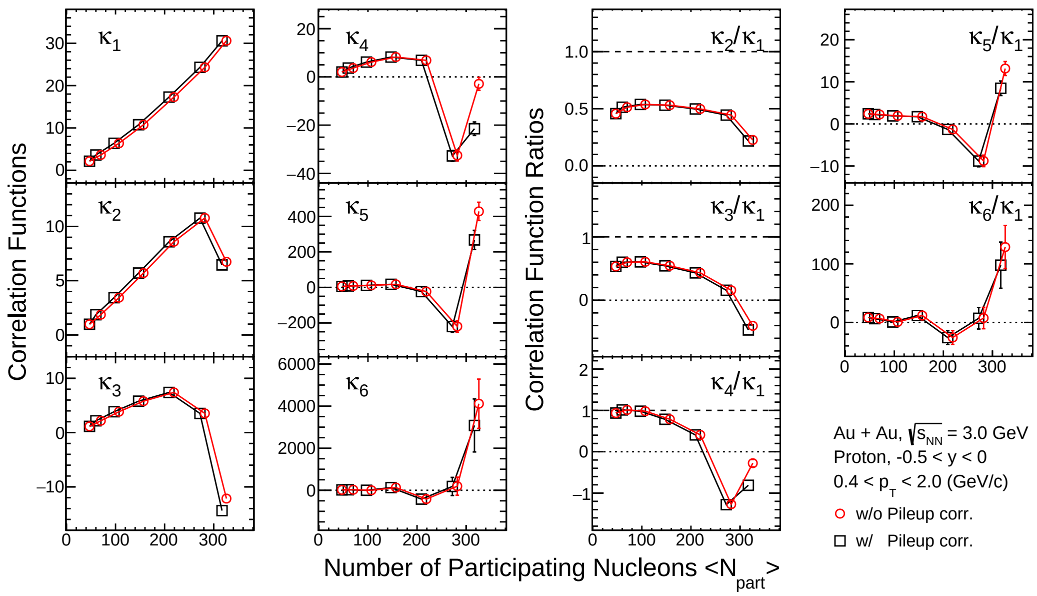

Figure 3.5.11: Centrality dependence of correlation functions and correlation function ratios up to 6th-order in Au+Au collisions at $\sqrt{s_{\mathrm{NN}}} = 3\,\mathrm{GeV}$ within kinematic acceptance $-0.5 < y < 0$ and $0.4 < p_{\mathrm{T}} < 2.0$ GeV/c. Results without or with pileup correction are shown with red circles and black squares, respectively.

3.6 Initial Volume Fluctuation Correction

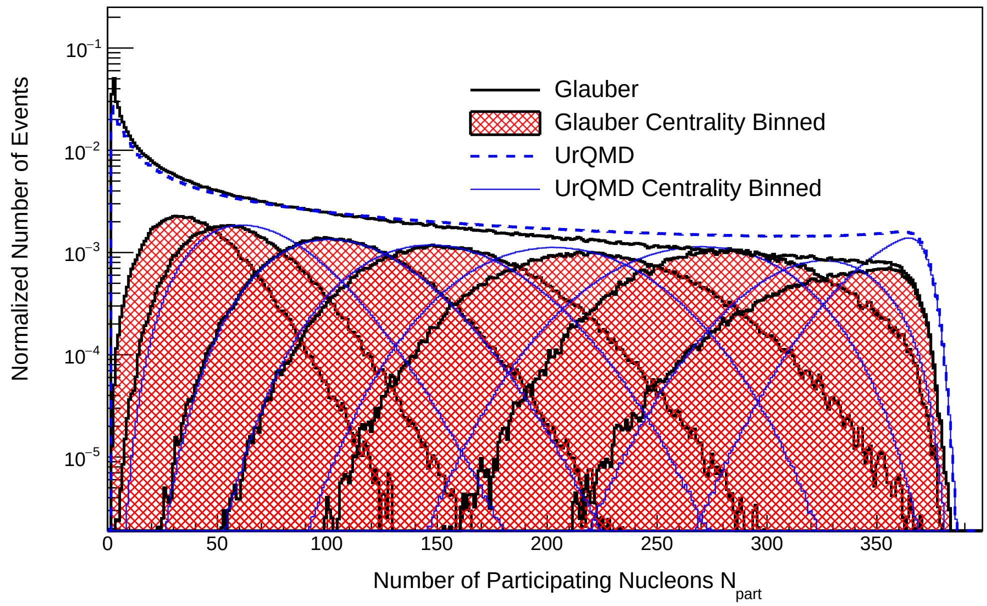

Figure 3.6.1: Number of participating nucleons (N_{part}) distribution from Glauber (black lines) and UrQMD (blue lines) model, respectively. The red shaded areas and blue lines indicate N_{part} distributions from centrality classes of 0-5%, 5-10%, ···, 50-60% which are determined by reference multiplicity.

In the field of heavy ion physics, collision volume is not a well-defined quantity. It reflects initial collision geometry and is usually related to number of participants (or called wounded nucleons proposed in Wound Nucleon Model [81]) which is the number of nucleons in one collision that has at least one inelastic interaction. In experiment, reference multiplicity is usually used to define centrality using the information that more central collision has a larger particle multiplicity. But the mapping of collision volume to reference multiplicity is not one-to-one correspondence. In a word about the VF effect, in fluctuation analysis using a centrality reference like charged particle reference multiplicity or other references in experiment, additional fluctuations due to fluctuating collision volume are mixed with the dynamical fluctuations because of QCD critical point or phase transition. The volume fluctuation effect is due a weak correlation between experimental centrality reference and collision volume.

In low energy fixed-target experiment, because of limited value of reference multiplicity, it is important to take care of the volume fluctuation effect in fluctuation analysis. A volume fluctuation correction

(VFC) method is proposed in Ref. [82]. The method based on Wound Nucleon Model [81] assumes that particle production in heavy ion collision is independently contributed from wounded nucleons. In another word, total particles produced in a collision are a sum of particles produced from each wounded nucleon. No correlation is considered between each wounded nucleon when producing particles. The deduction of volume corrected moments is shown below briefly.

Let us define the probability to find n particle from a wounded nucleon is $P(n)$, the moment generating function is written as $M(t) = \int_{-\infty}^{\infty} e^{t\cdot n} P(n) dn$. Total particles N is written as $N = n_1 + n_2 + n_3 + \cdots$ where n_i represents particle from each source and the corresponding moment generating function is then the product of that from each wounded nucleon $M(t)_N = [M(t)]^{N_w}$ where N_w is defined as number of wounded nucleons. Then it is easily to calculate raw moments of particle number distribution N of any order by taking derivatives of $M(t)_N$. The 1$^{\text{st}}$ and 2$^{\text{nd}}$-order raw moments are

$$\langle N \rangle_f = \left[\frac{dM_{N(t)}}{dt}\right]_{t=0} = \left[N_w \, [M(t)]^{N_w-1} \, \frac{dM(t)}{dt}\right] = N_w \langle n \rangle \tag{3.6.1}$$

and

$$\langle N^2 \rangle_f = \left[\frac{d^2 M_{N(t)}}{dt^2}\right]_{t=0} = N_w (N_w - 1) \langle n \rangle^2 + N_w \langle n^2 \rangle, \tag{3.6.2}$$

where $\langle . \rangle$ indicates taking average and $\langle N \rangle_f$ mean fixed number of wounded nucleons. Above equations apply to fixed number of wounded nucleons. For fluctuating wounded nucleon number with a probability $P(N_w)$, Eqs. 3.6.1 and 3.6.2 can be rewritten as

$$\langle N \rangle = \sum_{N_w} \langle N \rangle_f P(N_w) = \langle N_w \rangle \langle n \rangle \tag{3.6.3}$$

and

$$\langle N^2 \rangle = \sum_{N_w} \langle N^2 \rangle_f P(N_w) = \langle N_w (N_w - 1) \rangle \langle n \rangle^2 + \langle N_w \rangle \langle n^2 \rangle. \tag{3.6.4}$$

Higher order moments are obtained similarly. The final volume fluctuation corrected cumulants up to 6$^{\text{th}}$-

order expressed in terms of moments are shown below,

$$
\begin{aligned}
C_{1,N} &= C_{1,N_w} C_{1,n}, \\
C_{2,N} &= C_{1,N_w} C_{2,n} + C_{1,n}^2 C_{2,N_w}, \\
C_{3,N} &= C_{1,N_w} C_{3,n} + 3C_{1,n} C_{2,n} C_{2,N_w} + C_{1,n}^3 C_{3,N_w}, \\
C_{4,N} &= C_{1,N_w} C_{4,n} + 4C_{1,n} C_{3,n} C_{2,N_w} + 3C_{2,n}^2 C_{2,N_w} + 6C_{1,n}^2 C_{2,n} C_{3,N_w} + C_{1,n}^4 C_{4,N_w}, \\
C_{5,N} &= C_{1,N_w} C_{5,n} + 5C_{1,n} C_{4,n} C_{2,N_w} + 10C_{2,n} C_{3,n} C_{2,N_w} + 10C_{3,n} C_{1,n}^2 C_{3,N_w} \\
&\quad + 15C_{2,n}^2 C_{1,n} C_{3,N_w} + 10C_{2,n} C_{1,n}^3 C_{4,N_w} + C_{1,n}^5 C_{5,N_w}, \\
C_{6,N} &= C_{1,N_w} C_{6,n} + 6C_{5,n} C_{1,n} C_{2,N_w} + 15C_{4,n} C_{2,n} C_{2,N_w} + 10C_{3,n}^2 C_{2,N_w} \\
&\quad + 15C_{4,n} C_{1,n}^2 C_{3,N_w} + 60C_{3,n} C_{2,n} C_{1,n} C_{3,N_w} + 15C_{2,n}^3 C_{3,N_w} + 20C_{3,n} C_{1,n}^3 C_{4,N_w} \\
&\quad + 45C_{2,n}^2 C_{1,n}^2 C_{4,N_w} + 15C_{2,n} C_{1,n}^4 C_{5,N_w} + C_{1,n}^6 C_{6,N_w},
\end{aligned} \tag{3.6.5}
$$

where $C_{i,N}$, $C_{i,n}$ and C_{i,N_w} are i^{th} order cumulant from measured N distribution, each source's n distribution, and N_w distribution. From Eqs. 3.6.5, it is seen that cumulant from N_w is involved in measured cumulant $C_{i,N}$. Under an unrealistic case the cumulant $C_{i,N}^{'}$ without contribution from N_w can be expressed by

$$
C_{i,N}^{'} = \langle N_w \rangle \cdot C_{i,n}. \tag{3.6.6}
$$

The necessary input is only distribution of N_w which is not available in data and has to rely on model simulation.

3.6.1 Model Test of Volume Fluctuation Correction

In this section, I show a test the volume fluctuation correction using Eqs. 3.6.5 within UrQMD model. Around 80 million minbias events are generated using UrQMD program (v3.4) configured as the standard cascade mode. The necessary N_w distribution for correction (will use N_{part} instead in following section) is from UrQMD data or a Glauber Monte Carlo simulation. For real data analysis, one has to rely on Glauber simulation to give this N_{part} distribution. In UrQMD model, N_{part} distribution can be given without Glauber model and the N_{part} distribution should be more precise than that given by the Glauber model similation.

Figure 3.6.1 shows number of participating nucleon (N_{part}) distribution from UrQMD (dash line) and Glauber model (solid line) in Au+Au collisions at $\sqrt{s_{\text{NN}}} = 3$ GeV where the blue and red shaded areas are for 0-5% collisions determined by reference multiplicity. It is seen that UrQMD and Glauber show different shapes for N_{part} distribution which brings difference to volume fluctuation corrected result.

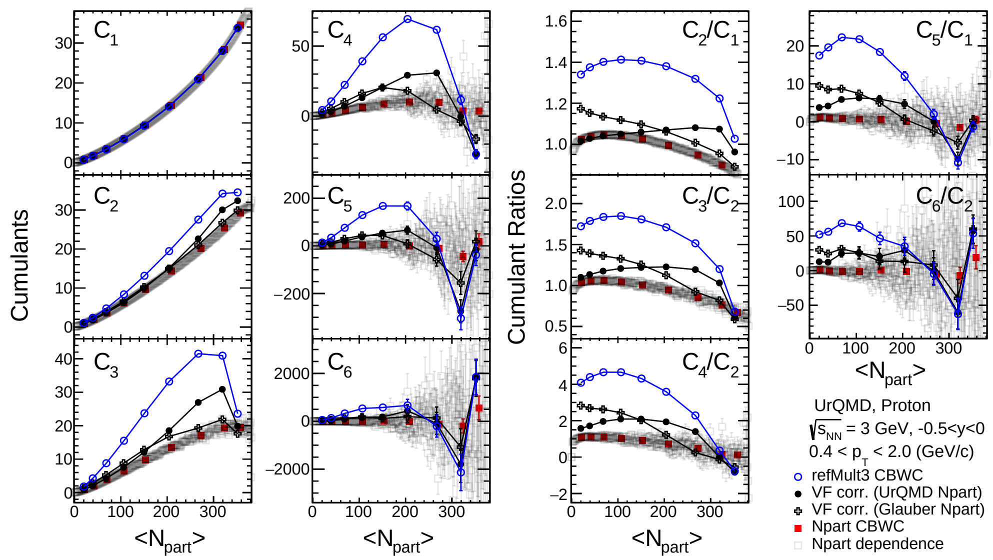

Figure 3.6.2: Centrality dependence of cumulants and cumulant ratios in Au+Au collisions at $\sqrt{s_{\rm NN}}$ = 3 GeV within kinematic acceptance $-0.5 < y < 0$ and $0.4 < p_{\rm T} < 2.0$ GeV/c from UrQMD model.

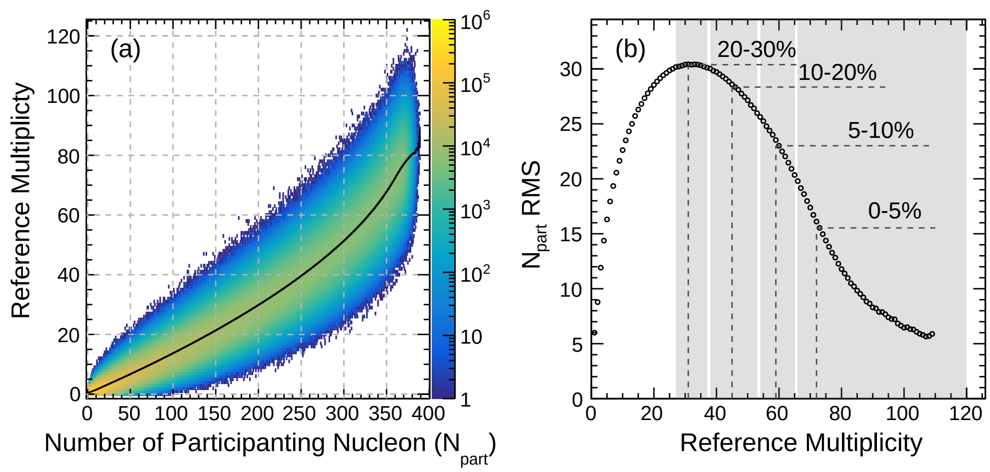

Figure 3.6.3: Left panel(a): Reference multiplicity distribution v.s. number of participating nucleon ($N_{\rm part}$) distribution from UrQMD model. Right panel(b): $N_{\rm part}$ RMS (root-mean-square) as a function of reference multiplicity. The vertical lines indicate average $N_{\rm part}$ RMS for each centrality class.

Figure 3.6.2 shows centrality dependence of cumulants in Au+Au collisions at $\sqrt{s_{\mathrm{NN}}} = 3$ GeV with kinematic acceptance $-0.5 < y < 0$ and $0.4 < p_{\mathrm{T}} < 2.0$ GeV/c within UrQMD model. The blue open circles represent a default calculation in UrQMD that cumulants and their ratios are calculated in each RefMult3 bin then are performed CBWC using number of events as weight. The black circles and crosses are calculation with volume fluctuation correction using N_{part} from UrQMD and Glauber model, respectively. Comparing volume fluctuation corrected cumulant ratios (black circles and crosses) with that in default calculation (blue open circles), it is seen that results from most central and peripheral collisions are least modified by volume fluctuation correction. This is expected from Fig. 3.6.3 panel (b) which shows N_{part} RMS with fixed reference multiplicity. Figure 3.6.3 panel (a) shows correlation between reference multiplicity and N_{part} in Au+Au collisions at $\sqrt{s_{\mathrm{NN}}} = 3$ GeV from UrQMD model. The N_{part} RMS, width of N_{part} distribution for each reference multiplicity bin, are small for most central and peripheral, and large for mid-central collisions. In Fig. 3.6.2, volume fluctuation corrected results (black circles and crosses) show least effect for most central collisions.

As a baseline without contribution from volume fluctuation I calculate cumulants in terms of N_{part}. Black open squares in Fig. 3.6.2 are cumulants and their ratios as a function of N_{part}. N_{part} is also used to determine different % of centrality, for example 0-5%, 5-10%, ···, 50-60%, then we can apply CBWC to the N_{part} dependence of cumulants using number of events as weight at individual N_{part} bin. This result is shown with red solid squares and is genuine result without volume fluctuation. Comparing results with or without volume fluctuation correction to the genuine result, we see that in most central centrality class the volume corrected results are close to results calculated with respect to N_{part}, but one can still see residual effects from volume fluctuation.

3.6.2 Volume Fluctuation Correction on Data

With the N_{part} distributions extracted from the Glauber and UrQMD model, the volume fluctuation correction can then be applied on data. Note that the reference multiplicity distribution from the UrQMD model is scaled to fit into data. The volume fluctuation is done at each reference multiplicity bin and is applied CBWC to obtain centrality binned results.

Figures 3.6.4 and 3.6.5 show proton cumulants and ratios up to 6$^{\mathrm{th}}$-order in Au+Au collisions at $\sqrt{s_{\mathrm{NN}}}$= 3 GeV within acceptance of $-0.5 < y < 0$ and $0.4 < p_{\mathrm{T}} < 2.0$ GeV/c. The fine bin results are cumulants as a function of reference multiplicity while wider bin results are for centrality binned cumulants. By definition shown in Eq. 3.6.5 and Eq. 3.6.6, mean value of proton multiplicity (C_1) is superposition of contributions from each sources thus is not corrected. Overall, comparing results with and without volume

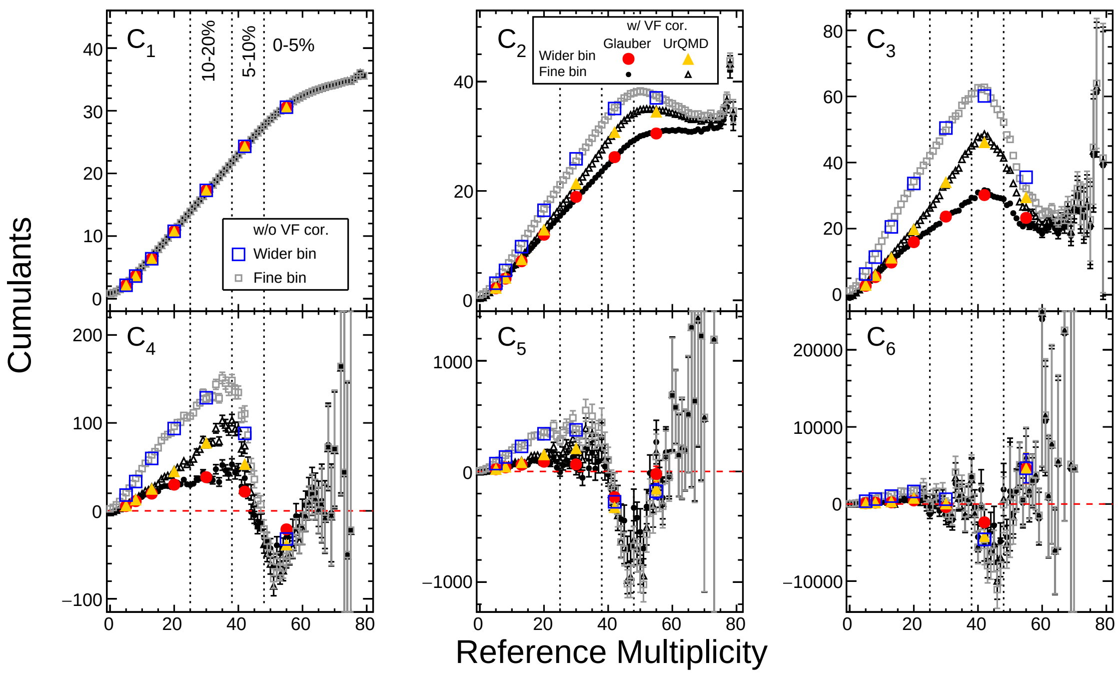

Figure 3.6.4: Proton cumulants up to 6th-order as a function of reference multiplicity in Au+Au collisions at $\sqrt{s_{NN}} = 3$ GeV within acceptance of $-0.5 < y < 0$ and $0.4 < p_T < 2.0$ GeV/c. Centrality binned (wider bin in plot) results with volume fluctuation correction using Glauber, UrQMD model and the result without correction are shown with red circles, blue squares, and yellow triangles, respectively. The corresponding fine bind results are shown with black circles, black triangles, and black squares, respectively. The vertical dashed lines indicate the centrality classes, from right to left, $0-5\%$, $5-10\%$, $10-20\%$, $20-30\%$, $30-40\%$, $40-50\%$ and $50-60\%$.

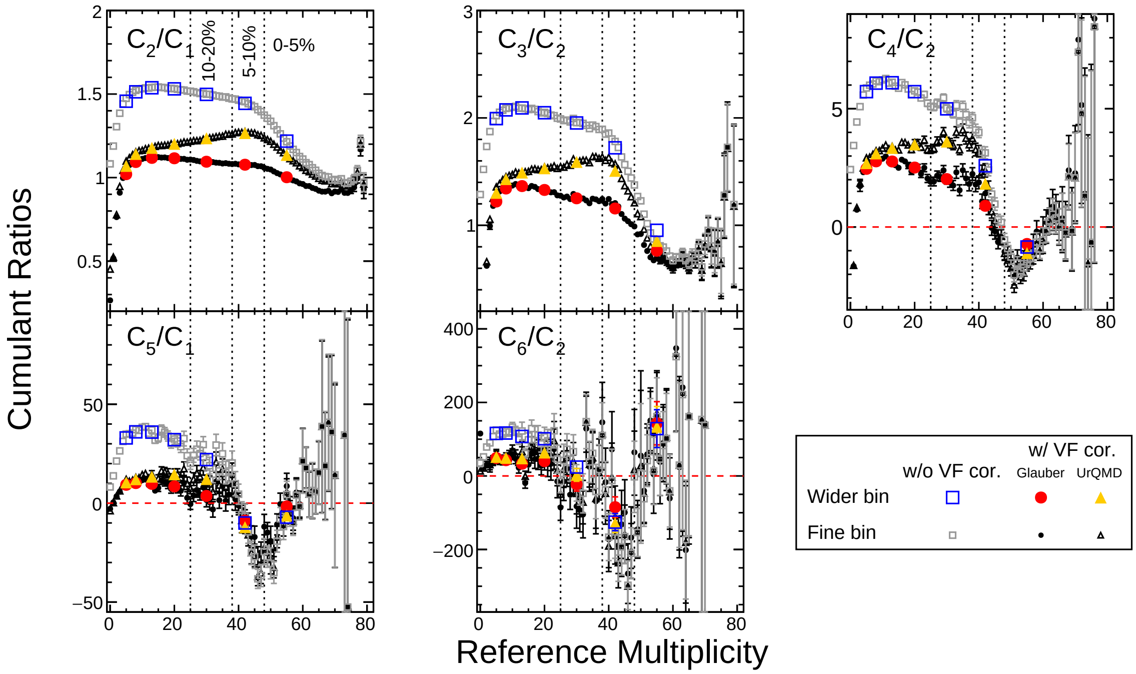

Figure 3.6.5: Proton cumulant ratios up to 6$^{\text{th}}$-order as a function of reference multiplicity in Au+Au collisions at $\sqrt{s_{\mathrm{NN}}} = 3$ GeV within acceptance of $-0.5 < y < 0$ and $0.4 < p_{\mathrm{T}} < 2.0$ GeV/c. Centrality binned (wider bin in plot) results with volume fluctuation correction using Glauber, UrQMD model and the result without correction are shown with red circles, blue squares, and yellow triangles, respectively. The corresponding fine bin results are shown with black circles, black triangles, and black squares, respectively. The vertical dashed lines indicate the centrality classes, from right to left, $0-5\%$, $5-10\%$, $10-20\%$, $20-30\%$, $30-40\%$, $40-50\%$ and $50-60\%$.

correction, for higher order cumulants, a maximum difference is seen around mid-central centrality and the difference slightly depends on the order of the cumulants. In the most central centrality, the difference between results with and without the correction is small for all cumulants $C_i, i > 3$. It is also seen that centrality binned results follow the trend of reference multiplicity dependence, thus the CBWC procedure is necessary in order to extract properly centrality binned results. It is worth noting that the results using different N_{part} to perform volume correction show clear difference for cumulants $C_i, i = 2, 3, 4$. The correction shows strong model dependence on N_{part}.

3.7 UrQMD Calculation

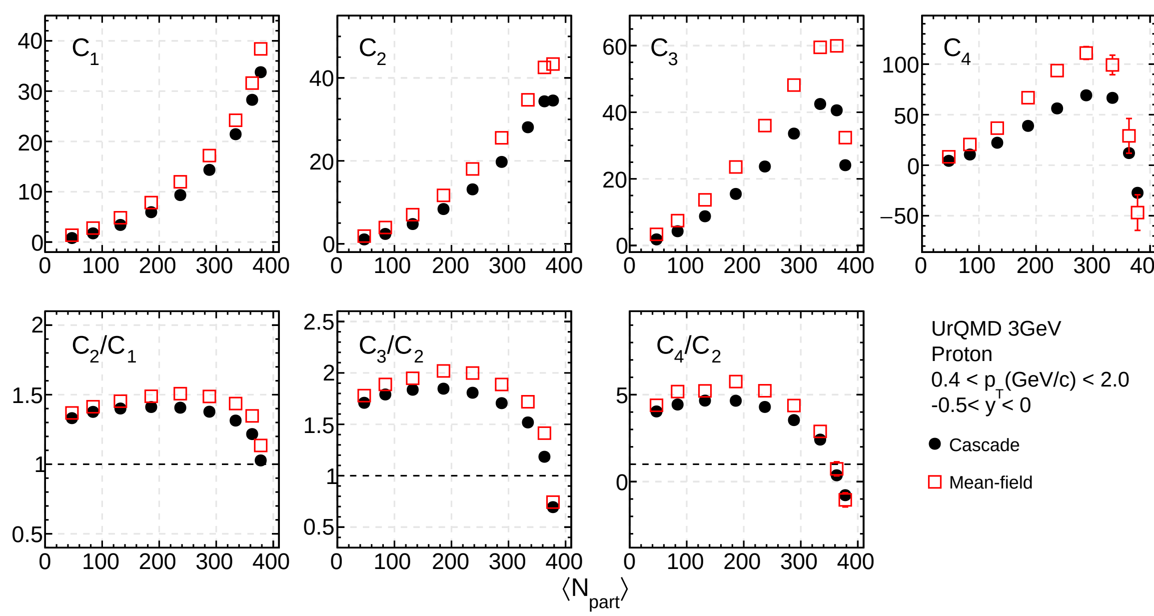

Figure 3.7.1: Cumulants and cumulant ratios up to 4$^{\mathrm{th}}$-order of proton multiplicity distributions in Au+Au collisions at $\sqrt{s_{\mathrm{NN}}}$= 3 GeV within $-0.5 < y < 0$ and $0.4 < p_{\mathrm{T}} < 2.0$ GeV/c within UrQMD model.

The Ultra-relativistic Quantum Molecular Dynamics [58, 59] (UrQMD) is a microscopic transport model, which is used to simulate the time evolution of (ultra-) relativistic heavy-ion collisions from 1 AGeV fixed-target energies up to collider energies of $\sqrt{s_{\mathrm{NN}}} = 200$ GeV from initial reaction-state to fragmentation into hadrons and then covariant propagation of hadrons and resonances through scatterings and decays. UrQMD model has been quite successful and widely applied towards heavy-ion phenomenology at a wide range of energy coverage from SIS to RHIC. In UrQMD model, hadron interactions below $\sqrt{s_{\rm NN}} =$ 5 GeV are described by interactions between hadrons and resonances. At collision energies above $\sqrt{s_{\rm NN}} =$ 5 GeV, the excitation of color strings and their fragmentation into hadrons dominates particle production. In UrQMD, hadrons have explicit space-time evolution trajectories and does not contain any de-confined quarks degrees of freedom which means no phase transition physics are implemented. So results from UrQMD model can be used as a non-critical baseline for experimentally measured higher-order cumulants.

In this section I show a comparison of UrQMD (v3.4) calculations using two configurations, the cascade and mean field mode. By default a cascade mode is used in which there is no nuclear potential. The Skyrme type potential (including Yukuka and Coulomb potentials) is available in UrQMD codes and is also used in UrQMD simulation. At low energy nuclear potential is a non-negligible effect, thus a comparison of calculation in both modes is necessary as a baseline for the comparison with experimental measurements. I generated around 80 million and 10 million events in cascade and Skyrme mode, respectively, and calculate cumulants in a same manner that is used for data. Figure 3.7.1 shows centrality dependence of proton cumulants up to 4$^{\rm th}$-order in Au+Au collisions at $\sqrt{s_{\rm NN}}$= 3 GeV within acceptance of $-0.5 < y < 0$ and $0.4 < p_{\rm T} < 2.0$ GeV/c from UrQMD model. It is seen that cumulants and ratios are close within statistical uncertainty in both calculations. Thus for qualitatively comparison with experimental data, the cascade mode should be fine.

3.8 Statistical and Systematic Uncertainty Estimation

3.8.1 Statistical Uncertainty

The statistical uncertainties are obtained using the Bootstrap approach [83] in which events are re-sampled with replacement and the analysis is re-run. The Bootstrap procedure is repeated for 200 times and the statistical uncertainty is the standard deviation of the observable, such as the cumulants and their ratios. The analytical method called Delta theorem [75, 84] to evaluate statistical uncertainty are also tested to crosscheck the uncertainty. In Appendix B and C I show analytical equations derived by Delta theorem. Equations in Appendix B are for efficiency uncorrected cumulants and correlation functions while equations in Appendix C are for efficiency corrected ones. Due to limit of thesis length and number of terms is too large for efficiency corrected formulas, only equations up to 2$^{\rm nd}$ order are listed. One can use the shared Python code to generate higher order equations.

3.8.2 Systematic Uncertainty

The systematic uncertainty of the cumulant calculation can be subdivided into three categories: uncertainty associated with a STAR Monte Carlo simulation, pileup correction, and centrality determination. The STAR Monte Carlo simulation includes the efficiency in the TPC and TOF, the track reconstruction requirements (maximum of DCA, minimum TPC spatial points), and the PID requirements ($n\sigma_{\text{Proton}}$ and mass-squared cut). The centrality determination for each centrality class is given in Tab. 3.3. The effect of lowering the dE/dx cut to $|n\sigma_{\text{Proton}}| < 2$ was tested but did not affect the final result.

To estimate the systematic uncertainty, the analysis was repeated with different analysis requirements which are outlined in Tab. 3.4. The difference between the systematic analyses and nominal analysis in C_2/C_1, C_3/C_2, and C_4/C_2 in 0-5% central Au+Au collisions is listed in Tab. 3.5.

Source	**Nominal Values**	**Variations**
Centrality	(N_{ch}) see Tab. 3.3	± 1 N_{ch}
Pileup fraction	0.46%	0.37%, 0.55%
TPC cuts	10	12 , 15
DCA < (cm)	3.0	2.75, 2.5, 2.0, 1.0
PID m^2 cuts (GeV^2/c^4)	(0.6, 1.2)	(0.5, 1.3), (0.7, 1.1)
Efficiency (ϵ)	ϵ	$\epsilon \times 1.05$, $\epsilon \times 0.95$

Table 3.4: Sources, choices of nominal values and their variations for systematic uncertainties in proton cumulant measurements from the fixed-target Au+Au collisions at 3 GeV.

3.8.3 Uncertainty from Pileup Events

Estimating the systematic uncertainty on the pileup correction method is straightforward: The underlying pileup distribution is fitted with a χ^2 minimization, and to test the systematic uncertainty, the χ^2/ndf is varied by ± 1. As expected, the change in the pileup's underlying distribution only affects the cumulants in the most central centrality class. As seen in Fig. 3.8.2, decreasing the pileup probability pulls C_4/C_2 closer to 1, while increasing the pileup probability pushes C_4/C_2 to a lower value, potentially over correcting. To see the increase with centrality, we can study the cumulants vs. FXTMult3, before applying CBWC. Figure 3.8.1 shows the pileup correction at each FXTMult3 bin. In the most central centrality class ($49 \le$ FXTMult3 < 80), the systematic is dominated by the highest multiplicity bins. Note that the statistics

Source	C_2/C_1	C_3/C_2	C_4/C_2
	1.218±0.001	0.954±0.005	-0.845±0.086
Centrality	**0.014**	**0.041**	**0.042**
Pileup	**0.002**	**0.017**	**0.242**
TPC cuts	0.002	0.015	0.24
DCA	0.008	**0.060**	**0.78**
PID m^2 cuts	0.003	0.009	0.05
Efficiency ϵ	**0.011**	0.023	0.27
Total	0.018	0.073	0.818

Table 3.5: Main contributors to systematic uncertainty to the proton cumulant ratios: C_2/C_1, C_3/C_2, and C_4/C_2 from 0-5% central 3 GeV Au+Au collisions. The first row shows values and statistical uncertainty of those ratios. The corresponding values of these ratios along with the statistical uncertainties are listed in the table. The final total value is the quadratic sum of contributions from Centrality, pileup and variations of cuts on TPC points, DCA and PID m^2 and efficiency ϵ which are written as bold. Clearly this analysis is systematic dominant.

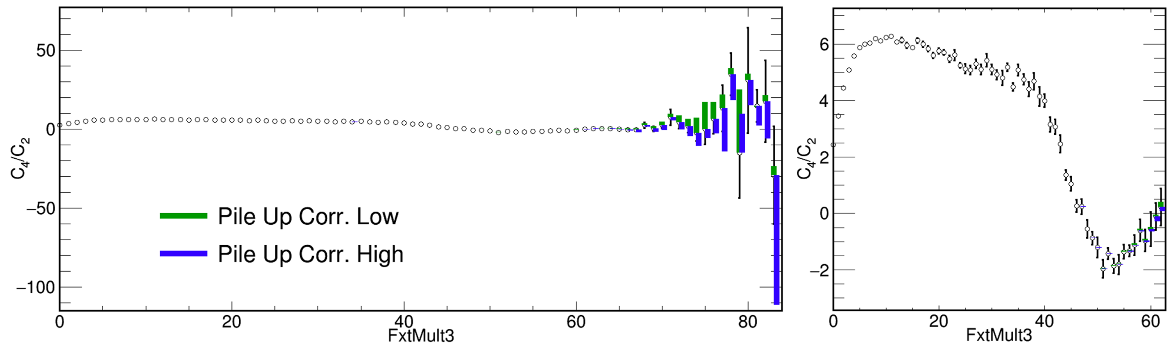

Figure 3.8.1: Left panel shows the uncertainty from pileup for the unbinned C_4/C_2 as a function of FXT-Mult3 for the fixed-target $\sqrt{s_{\mathrm{NN}}} = 3\,\mathrm{GeV}$ Au+Au collisions for the rapidity window $-0.5 < y < 0$ and the transverse-momentum window $0.4 < p_T < 2.0\,(\mathrm{GeV}/c)$. The right panel shows the same information with a limited x-axis from $0 <$ FXTMult3 < 60 and reduced y-axis to show the uncertainty at lower multiplicities. The difference in C_4/C_2 for the pileup high and pileup low correction (corresponding to $\chi^2 \pm 1$ of the pileup fit) is shown by blue and green error bars, respectively.

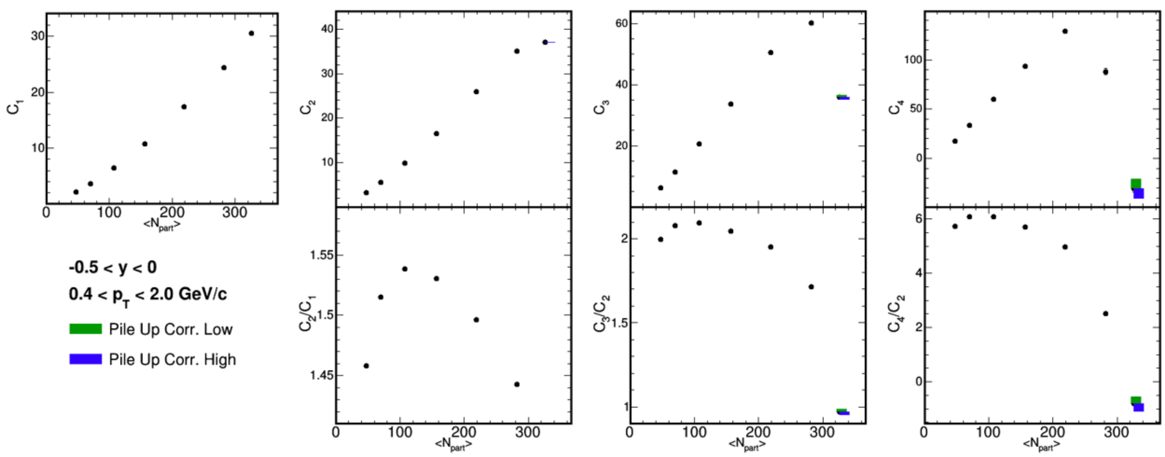

Figure 3.8.2: Panels show the proton cumulants (up to C_4) and proton cumulants ratios (C_2/C_1, C_3/C_2 and C_4/C_2) for the fixed-target $\sqrt{s_{\mathrm{NN}}} = 3\,\mathrm{GeV}$ Au+Au collisions for the rapidity window $-0.5 < y < 0$ and the transverse-momentum window $0.4 < p_{\mathrm{T}} < 2.0\,(\mathrm{GeV}/c)$. The difference in cumulant and cumulants ratios for the pileup high and pileup low correction (corresponding to $\chi^2 \pm 1$ of the pileup fit) is shown by blue and green error bars, respectively.

of these high multiplicity events significantly drop above multiplicities of 70. The large systematic uncertainties at high FXTMult3 bins will be reduced from the CBWC method. This can be seen comparing the most central centrality class in Fig. 3.8.1 and the final result with CBWC in Fig. 3.8.2.

3.8.4 Uncertainty from Efficiency and Related Cuts

The $\mathrm{nHitsFit}_{\mathrm{Min}} \geq 10$, TOF m^2, $n\sigma_{\mathrm{Proton}} < 3$, and DCA < 3 cm cuts are all correlated with efficiency, and the uncertainty can be attributed to systematic uncertainty in the embedding procedure. However, the cuts should be studied independently, as there may be changes to the proton purity of the selected proton candidates. For our analysis, the proton purity is higher than 95% at all rapidity region, momenta and centrality classes, therefore cut selection did not primarily prioritize proton purity.

Two cuts associated with proton purity are $n\sigma_{\mathrm{Proton}} < 3$ and DCA < 3cm. Lowering the $n\sigma_{\mathrm{Proton}}$ and DCA cuts will increase proton purity but decrease the TPC tracking efficiency. To test the effect of changing the $n\sigma_{\mathrm{Proton}} < 3$ cut, the analysis was run with $n\sigma_{\mathrm{Proton}} < 2$, decreasing the number of raw uncorrected protons, decreasing the efficiency and slightly increasing the purity. Running the analysis with $n\sigma_{\mathrm{Proton}} < 2$ generated a small increase in the C_4/C_2 as seen in Fig. 3.8.5. The $n\sigma_{\mathrm{Proton}} < 2$ was a relatively small uncertainty and was not included in the total systematic uncertainty. To study the effect on DCA, the value was lowered from DCA < 3 cm to DCA < 2.75 cm and DCA < 2.5 cm. As DCA < 3cm is the highest possible value in our reconstruction procedure, the uncertainty will be assumed to be symmetric around DCA < 3 cm. As the cut was decreased, all cumulants decreased to lower values, which indicates a lower tracking efficiency. I assume the DCA uncertainty to be highly correlated with the efficiency uncertainty. The choice of DCA < 3 cm as the nominal value was to maximize the number of raw protons measured and decrease the effect of the efficiency correction. Not only does a low DCA cut decrease overall efficiency, the cut introduces an East/West bias for track selection in the TPC. Due to increased distance from the fixed target, tracks in the East half of the TPC experience larger DCA values than tracks in the West TPC sector. By allowing tracks with a higher DCA, I minimize the East/West bias. The effect of DCA on the C_4/C_2 signal as a function of FXTMult3 can be seen in Fig. 3.8.5. Fig. 3.8.3 shows the effect of lowering the DCA for all cumulants. Like most systematic cuts studied, the DCA is most sensitive in the higher order cumulant C_4 and at central events.

An additional study of the DCA variable is performed to check the effect of lambda decays on the higher order cumulants. Fig. 3.8.4 shows the cumulants and cumulant ratios up to 4^{th}-order. The variation is comparable to the total systematic uncertainty.

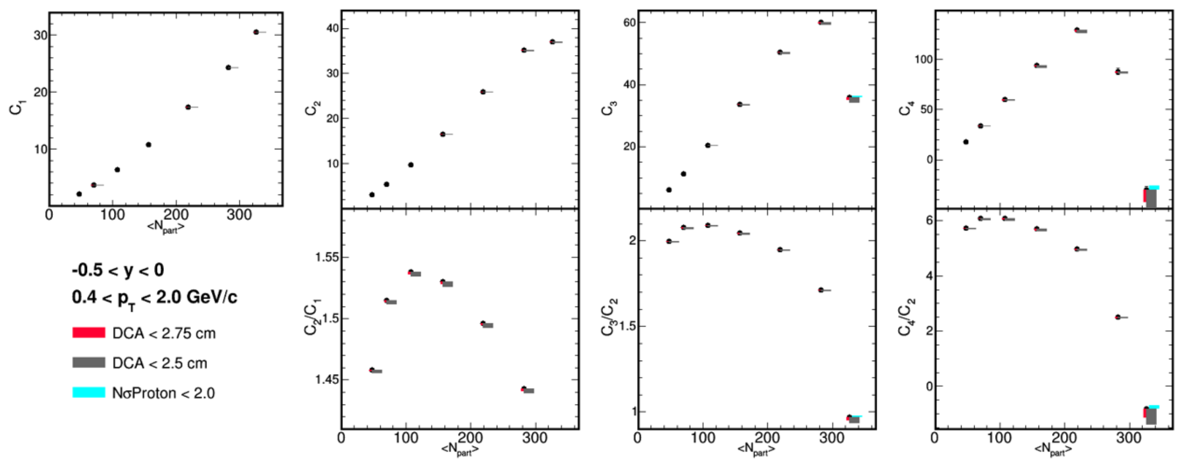

Figure 3.8.3: Panels show the proton cumulants (up to C_4) and proton cumulants ratios (C_2/C_1, C_3/C_2 and C_4/C_2) for the fixed-target $\sqrt{s_{\mathrm{NN}}} = 3$ GeV Au+Au collisions for the rapidity window $-0.5 < y < 0$ and the transverse-momentum window $0.4 < p_{\mathrm{T}} < 2.0$ (GeV/c). The difference in cumulants and cumulant ratios for the DCA < 2.75 cm, DCA < 2.5 cm and $n\sigma_{\mathrm{Proton}} < 2$ cuts are shown by red, gray and light blue error bars, respectively.

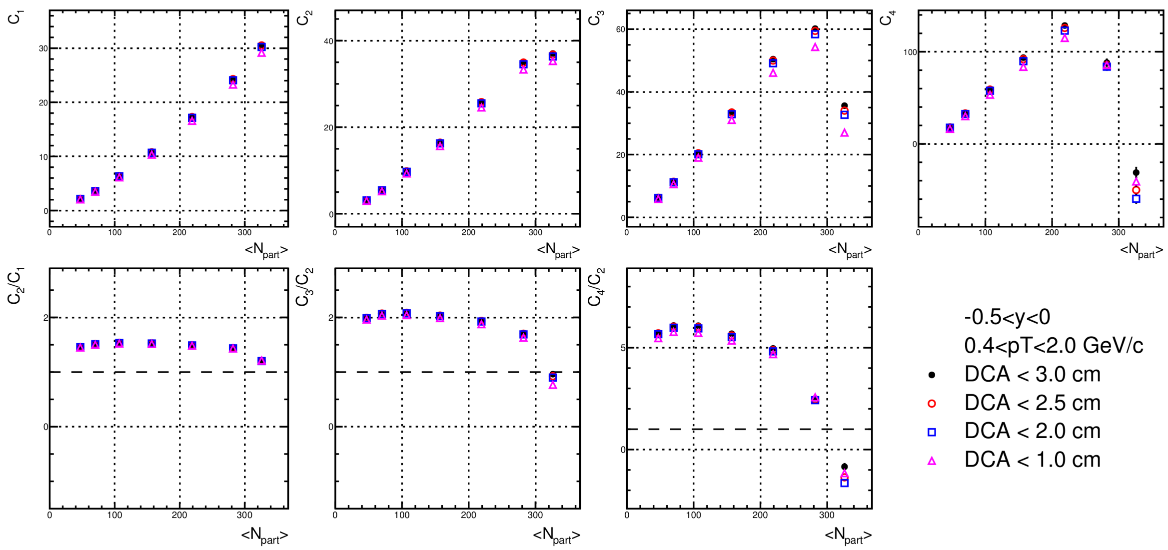

Figure 3.8.4: Panels show the proton cumulants (up to C_4) and proton cumulants ratios (C_2/C_1, C_3/C_2 and C_4/C_2) for the fixed-target $\sqrt{s_{\mathrm{NN}}} = 3\,\mathrm{GeV}$ Au+Au collisions for the rapidity window $-0.5 < y < 0$ and the transverse-momentum window $0.4 < p_{\mathrm{T}} < 2.0$ (GeV/c). The analysis is performed for various DCA cuts.

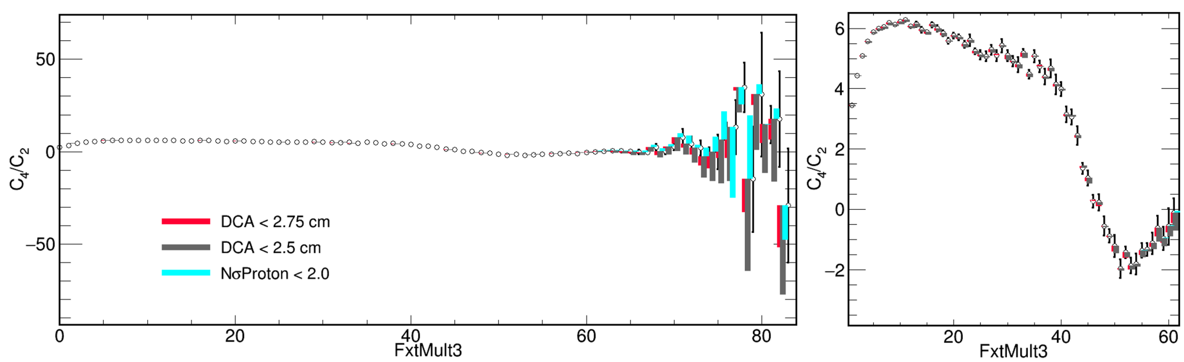

Figure 3.8.5: Left panel shows the uncertainty from pileup for the unbinned C_4/C_2 as a function of FXTMult3 for the fixed-target $\sqrt{s_{\mathrm{NN}}} = 3\,\mathrm{GeV}$ Au+Au collisions for the rapidity window $-0.5 < y < 0$ and the transverse-momentum window $0.4 < p_T < 2.0$ (GeV/c). The right panel shows the same information with a limited x-axis from $0 <$ FXTMult3 < 60 and reduced y-axis to show the uncertainty at lower multiplicities. The difference in C_4/C_2 for the DCA < 2.75 cm, DCA < 2.5 cm and $n\sigma_{\mathrm{Proton}} < 2.0$ cuts are shown by red, gray and light blue error bars, respectively.

The nHitsFit $\geq$ 10 cut is set to the lowest allowed value in the reconstruction procedure. Previous analyses have used a larger value to ensure track quality and the removal of broken tracks. However, we do not see the track quality to decrease with lower nHitsFit cuts and the removal of broken tracks can be accomplished by requiring nHitsFit/nHitsPossible > 0.51, a less restrictive cut. For the Fixed-Target regime, the high nHitsFit ≥ 15 or nHitsFit ≥ 25 cuts remove high η tracks in the region of interest. Due to the geometry of the target and the TPC, higher η tracks will pass through fewer TPC pad rows. Unlike the collider setup, the higher $\eta \approx 2$ correspond to mid-rapidity particles, our region of interest. To test the effect of nHitsFit on the analysis, the nHitsFit ≥ 10 is increased to nHitsFit ≥ 12 and nHitsFit ≥ 15. As nHitsFit ≥ 10 is the lowest allowed value, we assume a symmetric systematic uncertainty.

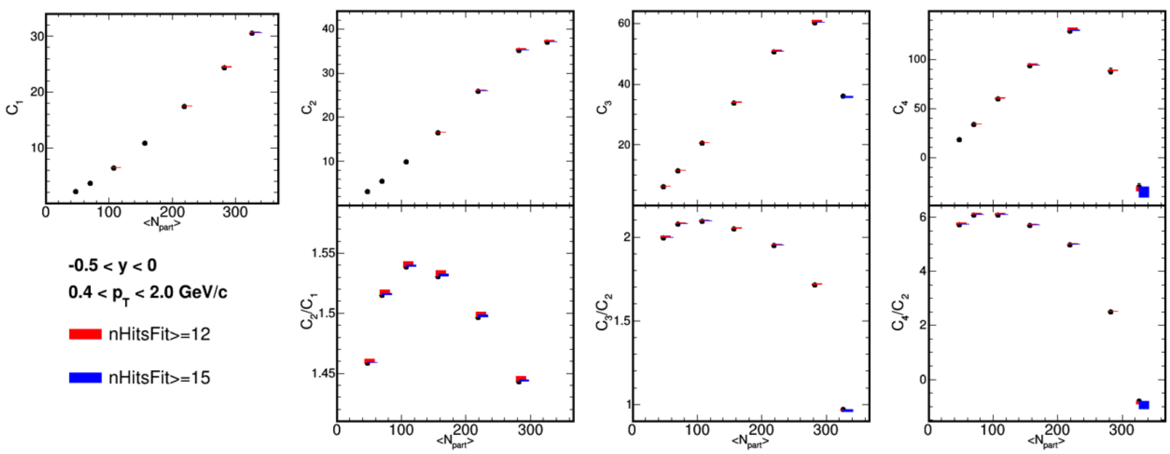

Figure 3.8.6: Panels show the proton cumulants (up to C_4) and proton cumulants ratios (C_2/C_1, C_3/C_2 and C_4/C_2) for the fixed-target $\sqrt{s_{\mathrm{NN}}} = 3$ GeV Au+Au collisions for the rapidity window $-0.5 < y < 0$ and the transverse-momentum window $0.4 < p_{\mathrm{T}} < 2.0$ (GeV/c). The difference in cumulants and cumulant ratios for the nHitsFit$\geq$ 12 and nHitsFit$\geq$ 15 cuts are shown by red and blue error bars, respectively.

The TOF m^2 cut is commonly studied in the cumulant analyses. Varying the TOF m^2 cut did not have a large effect on the higher order cumulants. The TOF m^2 is varied above and below the standard $0.6 < m^2 < 1.2$ (GeV/c^2)^2 by ± 0.05. The C_4/C_2 vs. FXTMult3 result is shown in Fig.3.8.9 and the final result for all cumulants and cumulant ratios are shown in Fig. 3.8.8. In Fig. 3.8.8, the systematic uncertainty from the TOF m^2 is negligible. Looking at C_4/C_2 in 3.8.9, there is a small increase in the systematic uncertainty at high multiplicities, but remains small with respect to the statistical and other systematic uncertainties.

The efficiency calculation of the TPC detector has considerable uncertainty. The process of embedding

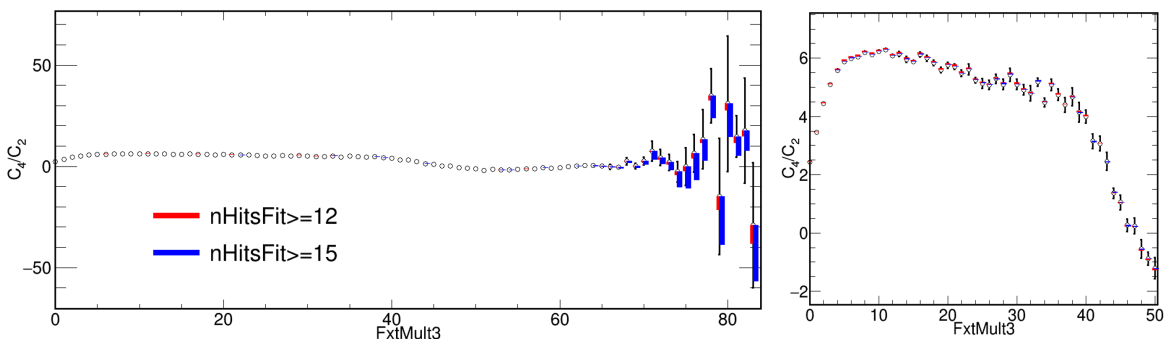

Figure 3.8.7: Left panel shows the uncertainty from pile up for the unbinned C_4/C_2 as a function of FXTMult3 for the fixed-target $\sqrt{s_{\mathrm{NN}}} = 3$ GeV Au+Au collisions for the rapidity window $-0.5 < y < 0$ and the transverse-momentum window $0.4 < p_{\mathrm{T}} < 2.0$ (GeV/c). The right panel shows the same information with a limited x-axis from $0 <$ FXTMult3 < 60 and reduced y-axis to show the uncertainty at lower multiplicities. The difference in C_4/C_2 for the nHitsFit$\geq$ 12 and nHitsFit$\geq$ 15 cuts are shown by red and blue error bars, respectively.

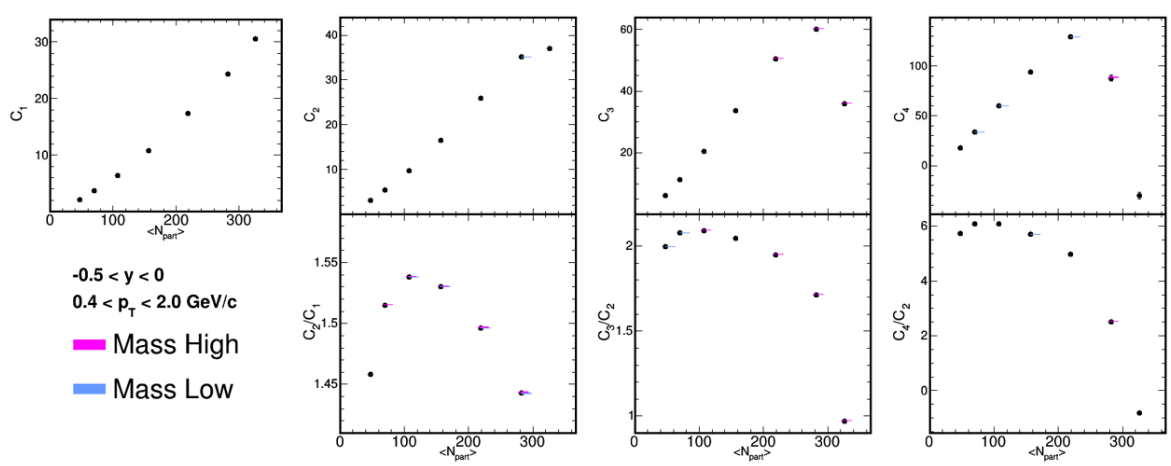

Figure 3.8.8: Panels show the proton cumulants (up to C_4) and proton cumulants ratios ($C_2/C_1, C_3/C_2$ and C_4/C_2) for the fixed-target $\sqrt{s_{\mathrm{NN}}} = 3$ GeV Au+Au collisions for the rapidity window $-0.5 < y < 0$ and the transverse-momentum window $0.4 < p_{\mathrm{T}} < 2.0$ (GeV/c). The difference in cumulants and cumulant ratios for the mass low and mass high cuts (mass cuts are varied by ± 0.05 from the nominal $0.6 < m^2 < 1.2$ (GeV/c^2)^2) are shown by magenta and blue error bars, respectively.

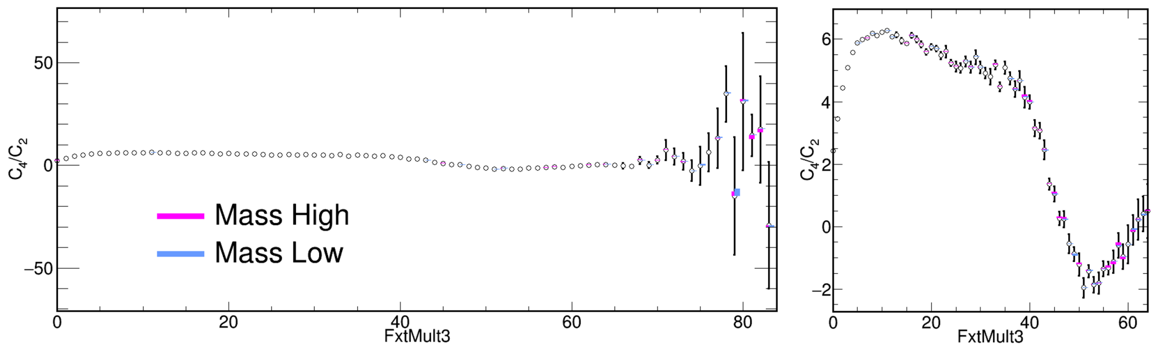

Figure 3.8.9: Left panel shows the uncertainty from pile up for the unbinned C_4/C_2 as a function of FXTMult3 for the fixed-target $\sqrt{s_{\mathrm{NN}}} = 3\,\mathrm{GeV}$ Au+Au collisions for the rapidity window $-0.5 < y < 0$ and the transverse-momentum window $0.4 < p_{\mathrm{T}} < 2.0$. The right panel shows the same information with a limited x-axis from 0 < FXTMult3 < 60 and reduced y-axis to show the uncertainty at lower multiplicities. The difference in C_4/C_2 for the mass low and mass high cuts (mass cuts are varied by ± 0.05 from the nominal $0.6 < m^2 < 1.2$ (GeV/c^2)^2) are shown by magenta and blue error bars, respectively.

Monte Carlo tracks into data and running the track reconstruction process is estimated to have an uncertainty of 2–5%. Therefore, the cumulants analysis is run with ±5% efficiency to estimate the effect on the higher order moments. Figure 3.8.10 shows the effect on the CBWC cumulants and cumulant ratios as a function of average N_{part}. Unlike previous cuts associated with efficiency, which preferentially affected the central 0-5% cumulant ratios, the broad change in ±5% overall efficiency affects all cumulants and cumulant ratios. Fig. 3.8.11 shows the effect on the C_4/C_2 ratio.

3.8.5 Uncertainty from Centrality Determination

The last systematic uncertainty considered is from the centrality determination. The centrality determination process is described in Sec. 3.2. Centrality determination is limited by the finite bin width of the multiplicity distribution. To estimate how this affects the cumulants, the centrality determination is varied by ±1 bin and the difference is taken as the systematic uncertainty. This uncertainty is negligible for the central events but considerable in the peripheral events. Fig. 3.8.12 shows the effect on the cumulants and ratios.

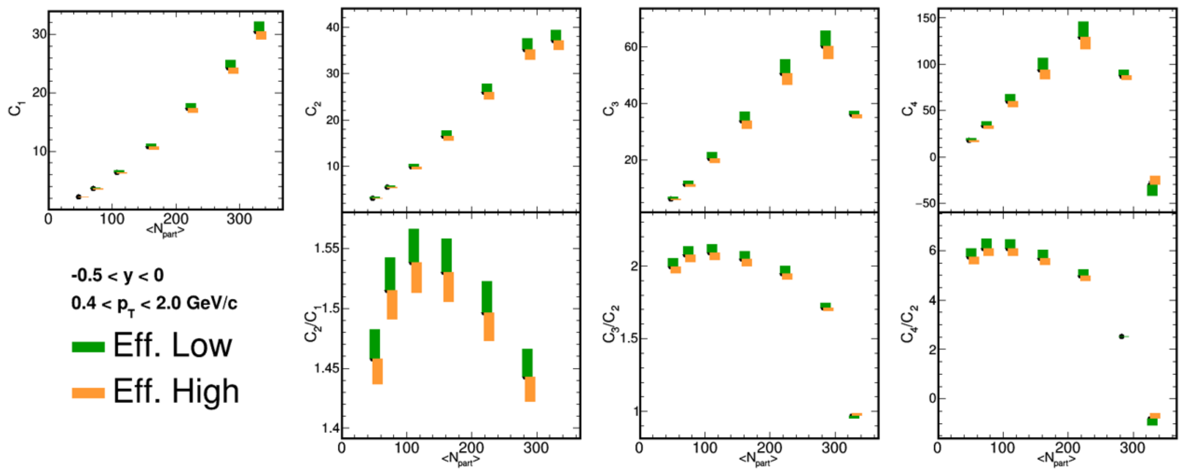

Figure 3.8.10: Panels show the proton cumulants (up to C_4) and proton cumulants ratios (C_2/C_1, C_3/C_2 and C_4/C_2) for the fixed-target $\sqrt{s_{\mathrm{NN}}} = 3$ GeV Au+Au collisions for the rapidity window $-0.5 < y < 0$ and the transverse-momentum window $0.4 < p_{\mathrm{T}} < 2.0$ (GeV/c). The difference in cumulants and cumulant ratios for an increased and decreased efficiency ($\pm5\%$) are shown by orange and green error bars, respectively.

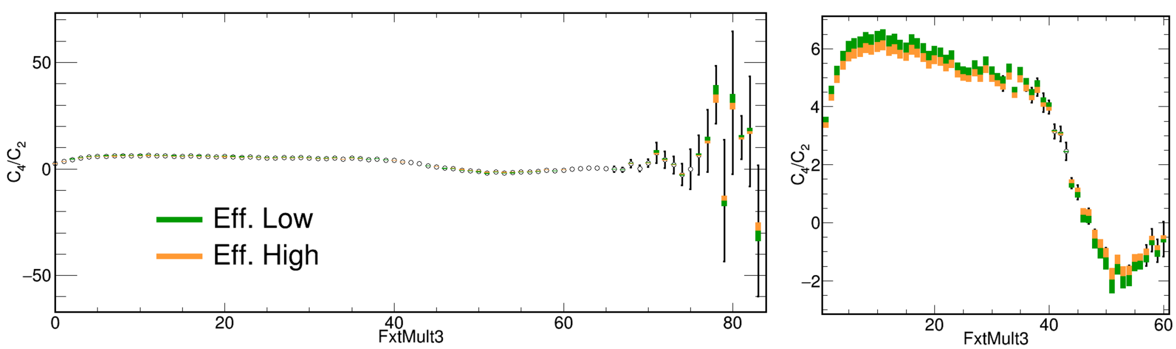

Figure 3.8.11: Left panel shows the uncertainty from pile up for the unbinned C_4/C_2 as a function of FXTMult3 for the fixed-target $\sqrt{s_{\mathrm{NN}}} = 3$ GeV Au+Au collisions for the rapidity window $-0.5 < y < 0$ and the transverse-momentum window $0.4 < p_{\mathrm{T}} < 2.0$ (GeV/c). The right panel shows the same information with a limited x-axis from FXTMult3 0 to 60 and reduced y-axis to show the uncertainty at lower multiplicities. The difference in C_4/C_2 for an increased and decreased efficiency ($\pm5\%$) are shown by orange and green error bars, respectively.

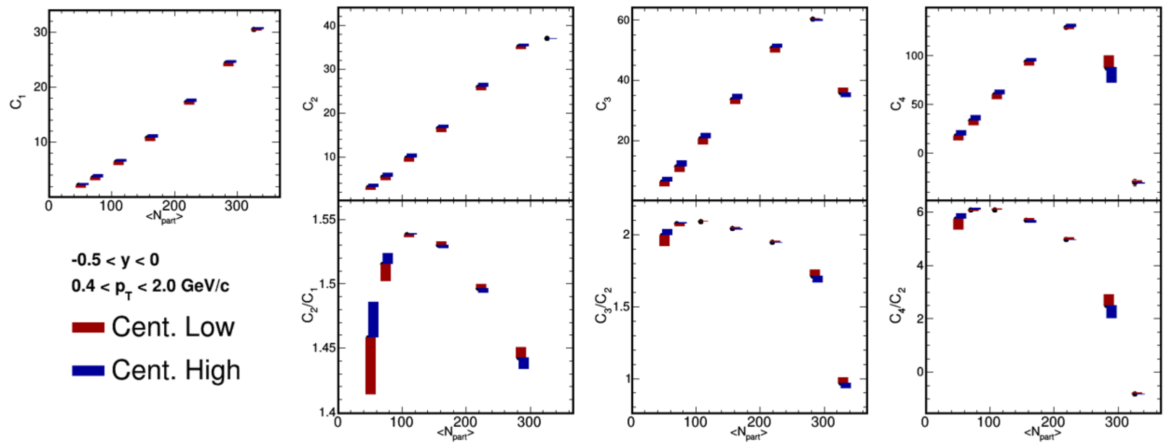

Figure 3.8.12: Panels show the proton cumulants (up to C_4) and proton cumulants ratios ($C_2/C_1, C_3/C_2 and C_4/C_2$) for the fixed-target $\sqrt{s_{\mathrm{NN}}} = 3\,\mathrm{GeV}$ Au+Au collisions for the rapidity window $-0.5 < y < 0$ and the transverse-momentum window $0.4 < p_{\mathrm{T}} < 2.0$ (GeV/c). The difference in cumulants and cumulant ratios for a change in centrality by ± 1 FXTMult3 bin are shown by red (-1) and blue ($+1$) error bars.

3.8.6 Summary of Systematic Uncertainty

An overview of the systematic uncertainty for C_4/C_2 is shown in Fig.3.8.13. The uncertainty is divided into two categories, the uncertainty from pile up determination and from efficiency related systematic variables. The uncertainty from the two sources are added in quadrature, where the uncertainty to C_4/C_2 is ± 0.30 and ± 0.27 from pile up and efficiency, respectively. A table is included (Tab.3.5) to describe each systematic cut and the effect on the C_4/C_2 uncertainty.

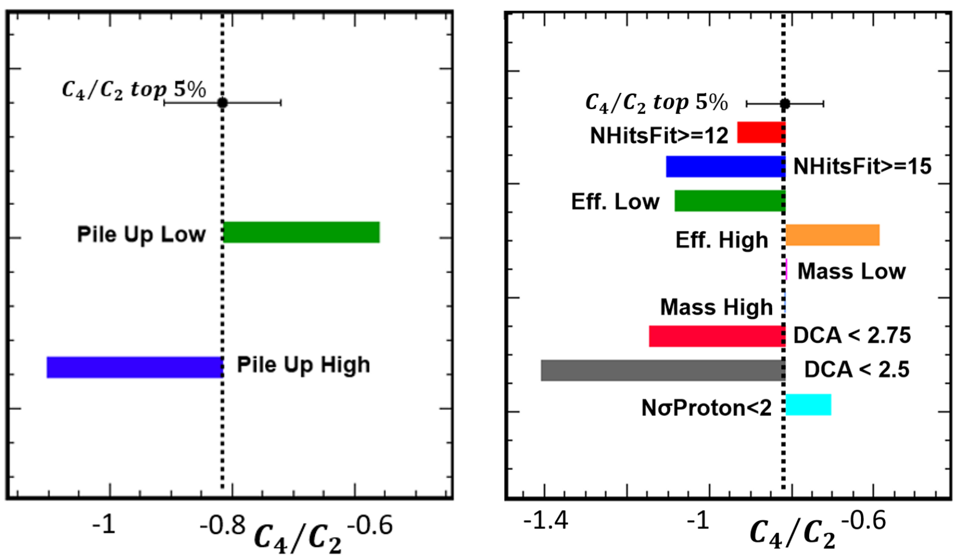

Figure 3.8.13: Left panel shows the systematic uncertainty from pile up determination for C_4/C_2. Right panel shows the systematic uncertainty from efficiency and related cuts for C_4/C_2.

Chapter 4

Results and Discussion

In this chapter I show results of higher-order cumulants of proton multiplicity distributions from STAR fixed-target data. Model calculations from UrQMD hydrodynamics model are also shown and compared with experimental measurements. Physics implications are discussed with respect to centrality, acceptance and collision energy dependence.

4.1 Event-by-event Proton Multiplicity Distribution

Figure 4.1.1 shows detector efficiency uncorrected event-by-event proton multiplicity distributions for 0-5%, 5-10%, 10-20%, 20-30%, 30-40%, 40-50% and 50-60% centrality classes in Au+Au collisions at $\sqrt{s_{\mathrm{NN}}} = 3$ GeV. Protons are identified by combining TPC and TOF detectors within kinematic acceptance $-0.5 < y < 0$ and $0.4 < p_{\mathrm{T}} < 2.0$ GeV/c. The distributions are normalized.

4.2 Centrality Dependence

Figure 4.2.1 show cumulants and cumulant ratios up to 6^{th}-order of proton multiplicity distributions as a function of the average of number of participants $\langle N_{\mathrm{part}} \rangle$ in Au+Au collisions at $\sqrt{s_{\mathrm{NN}}} = 3$ GeV within kinematic acceptance $-0.5 < y < 0$ and $0.4 < p_{\mathrm{T}} < 2.0$ GeV/c. Experimental data are corrected for detector efficiency and pileup effect, and are shown with black squares for different centrality classes which are 0-5%, 5-10%, 10-20%, 20-30%, 30-40%, 40-50%, and 50-60%. Black and grey bars indicate statistical and systematical uncertainties, respectively. The gold bands are calculations from UrQMD model within

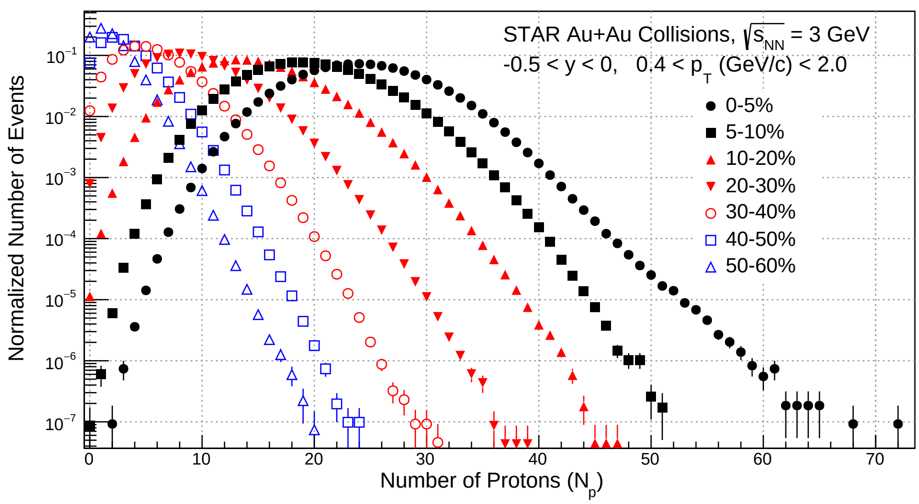

Figure 4.1.1: Event-by-event raw proton multiplicity distributions for 0-5%, 5-10%, 10-20%, 20-30%, 30-40%, 40-50% and 50-60% centrality classes in Au+Au collisions at $\sqrt{s_{\mathrm{NN}}} = 3$ GeV. The distributions are normalized.

the same kinematic acceptance used for data. CBWC are applied for both data and UrQMD calculations. It is seen from Fig. 4.2.1 that lower order cumulants (C_i, $i = 1, 2$) increase with the increase of N_{part} from peripheral to central collisions. The higher order cumulants (C_i, $i \geq 3$) reach a maximum at $\langle N_{\mathrm{part}} \rangle \sim 200$ then decrease rapidly. The non-linear scaling of C_3 and C_4 with respect to N_{part} were not seen in BES-I net-proton cumulants measurements [57, 74]. This may be due to the effect of volume fluctuation. All cumulant ratios are above unity in peripheral and mid-central collisions except in most central collisions. C_2/C_1 is above unity for all centrality which is not observed for proton in high energy measurements of experimental data in collider mode. The ratio C_4/C_2 in most central collisions is -0.845 ± 0.086 (stat) ± 0.818 (sys.) which is very well reproduced by UrQMD calculation.

Comparing data with UrQMD calculation it is seen that lower order cumulants (C_1 and C_2) of data are well reproduced by UrQMD, and for higher order cumulants ($\geq C_3$), the centrality dependence of data are qualitatively reproduced. The negative C_4 and C_4/C_2 in most central collisions are also seen in UrQMD calculation. Recall the calculation shown in Fig. 3.6.2 of UrQMD using N_{part} as centrality reference, we observed a positive C_4/C_2 for most central collisions. It might suggest that the negative sign for C_4 shown in data is due to volume fluctuation. 5^{th}- and 6^{th}-order cumulants and ratios show large systematic uncertainty which is mainly contributed by the DCA cut. Figure 4.2.2 shows centrality dependence of correlation

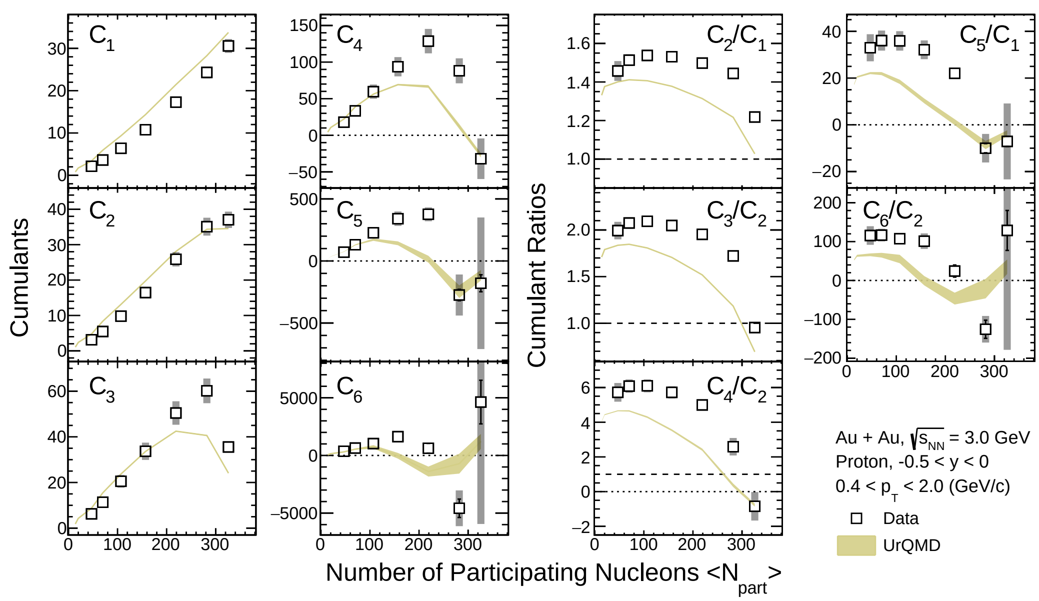

Figure 4.2.1: Centrality dependence of cumulants and cumulant ratios of proton multiplicity distributions up to 6$^{\text{th}}$-order in Au+Au collisions at $\sqrt{s_{\text{NN}}} = 3\,\text{GeV}$ within kinematic acceptance $-0.5 < y < 0$ and $0.4 < p_{\text{T}} < 2.0\,\text{GeV}/c$. Data are shown with black squares while UrQMD results are shown with gold band. Statistical and systematical uncertainty are shown with black and grey bars, respectively.

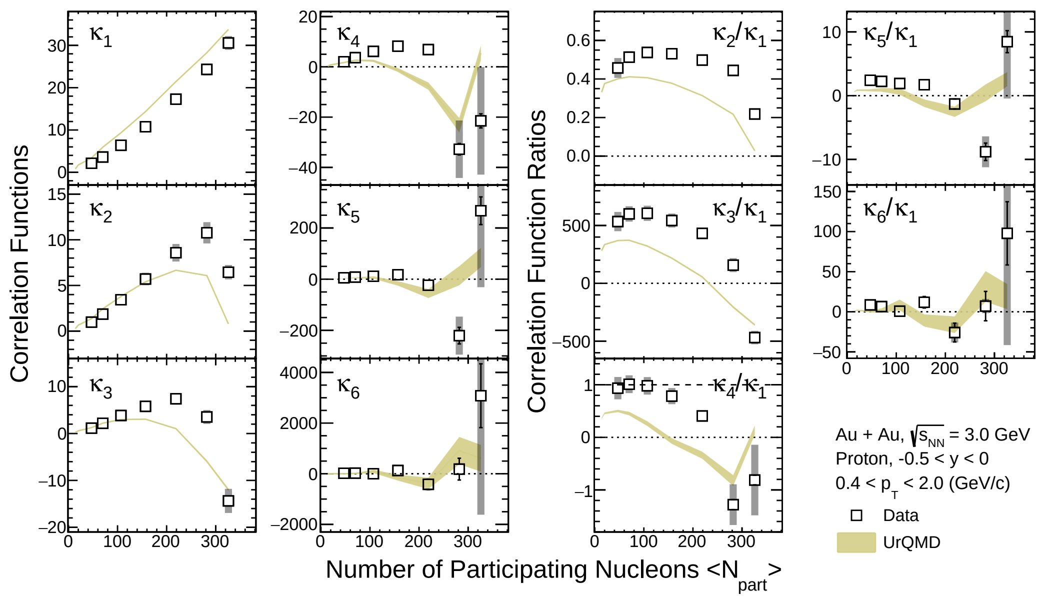

Figure 4.2.2: Centrality dependence of correlation and correlation function ratios of proton multiplicity distributions up to 6th-order in Au+Au collisions at $\sqrt{s_{\mathrm{NN}}} = 3\,\mathrm{GeV}$ within kinematic acceptance $-0.5 < y < 0$ and $0.4 < p_{\mathrm{T}} < 2.0\,\mathrm{GeV}/c$. Data are shown with black squares while UrQMD results are shown with gold band. Statistical and systematical uncertainty are shown with black and grey bars, respectively.

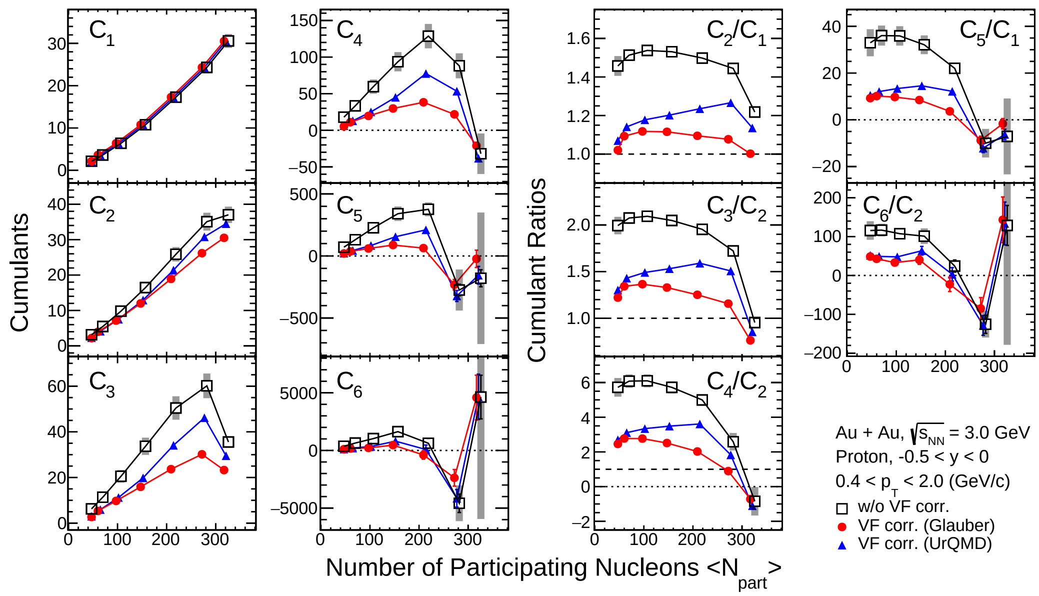

Figure 4.2.3: Centrality dependence of cumulants and cumulant ratios up to 6th-order in Au+Au collisions at $\sqrt{s_{\mathrm{NN}}} = 3$ GeV within kinematic acceptance $-0.5 < y < 0$ and $0.4 < p_{\mathrm{T}} < 2.0$ GeV/c. The black squares are results without volume correction while red circles and blue triangles represent results with volume correction using Glauber and UrQMD model, respectively.

functions and correlation function ratios with same acceptance from Fig. 4.2.1. We can see an positive κ_2 for all centrality classes. The large values of correlation functions are also seen in UrQMD calculation (gold bands) and the trends in data are qualitatively reproduced.

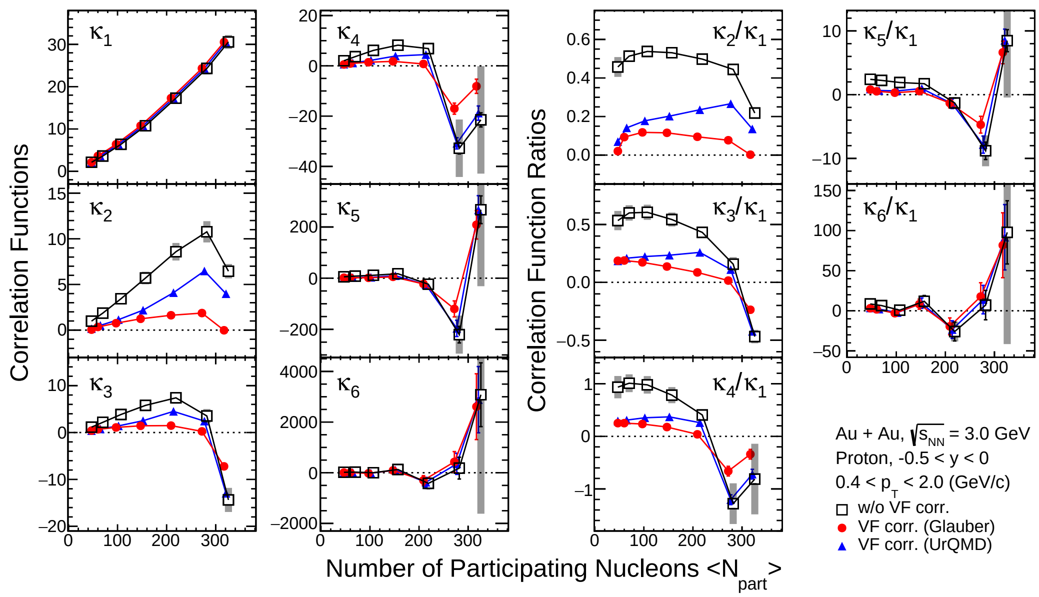

Figure 4.2.4: Centrality dependence of correlation functions and correlation function ratios up to 6$^{\text{th}}$-order in Au+Au collisions at $\sqrt{s_{\text{NN}}} = 3$ GeV within kinematic acceptance $-0.5 < y < 0$ and $0.4 < p_{\text{T}} < 2.0$ GeV/c. The black squares are results without volume correction while red circles and blue triangles represent results with volume correction using Glauber and UrQMD model, respectively.

Figures 4.2.3 and 4.2.4 show centrality dependence of cumulants and correlation functions of 3 GeV data within kinematic acceptance $-0.5 < y < 0$ and $0.4 < p_{\text{T}} < 2.0$ GeV/c. In these figures I show the data with the volume fluctuation correction. The blacks squares are without correction which are same data points shown in Figs. 4.2.1 and 4.2.2. The red circles and blue triangles are with volume correction using N_{part} distributions from Glauber and UrQMD model, respectively. As is shown in Sec. 3.6.2 according to the assumption of the volume fluctuation correction, C_1 is not modified. From C_2 we begin to see some changes which are large in mid central centrality ($\langle N_{\text{part}} \rangle \approx$ 150-250) small in peripheral and most central centrality. For C_3 or higher-order cumulants and ratios, results with or without volume fluctuation correction are consistent within uncertainty. The results with volume correction show strong model dependence on

N_{part} which is due to different mapping of charged particle reference multiplicity and number of participants in UrQMD or Glauber model. But one can see for higher order ratios C_3/C_2, C_4/C_2, C_5/C_1 and C_6/C_2 the effect is small in most central centrality class.

4.3 Rapidity (y) Dependence

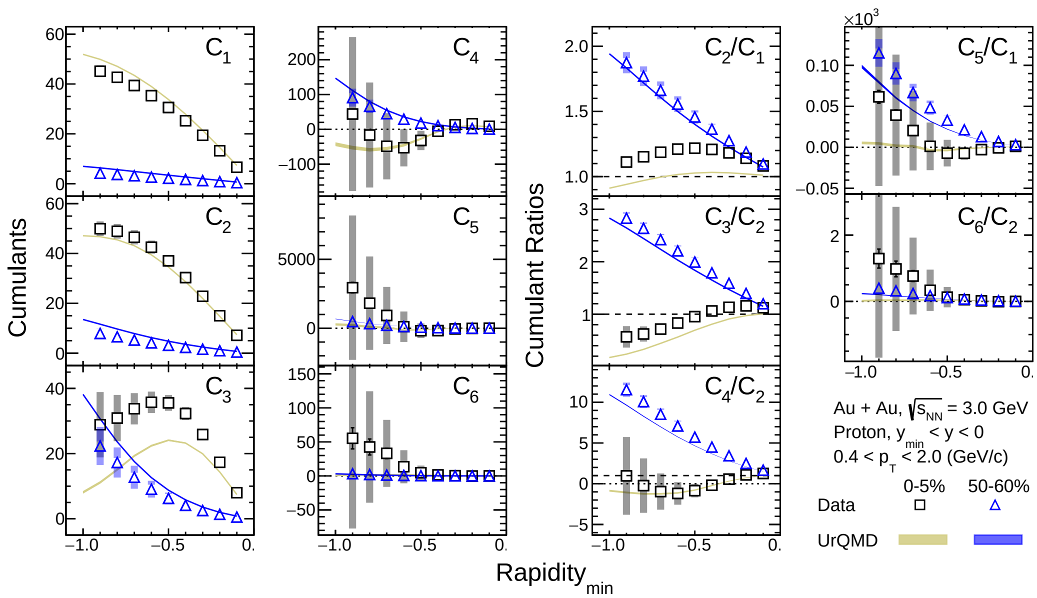

Figure 4.3.1: Rapidity dependence of cumulants and cumulant ratios of proton multiplicity distributions ratios up to 6th order in top 5% central and 50-60% peripheral Au+Au collisions at $\sqrt{s_{\text{NN}}} = 3$ GeV within kinematic acceptance $0.4 < p_{\text{T}} < 2.0$ GeV/c. The lower rapidity cut is varied from -0.1 to -0.9. Data are shown with black squares while UrQMD calculations are shown with gold bands. Statistical and systematical uncertainty are shown with black and grey bars, respectively.

Figure 4.3.1 shows rapidity dependence of cumulants and their ratios up to 6th-order in top 5% central and 50-60% peripheral Au+Au collisions at $\sqrt{s_{\text{NN}}} = 3$ GeV within kinematic acceptance $0.4 < p_{\text{T}} < 2.0$ GeV/c. The black squares and blue blue triangles are for data of 0-5% and 50-60% centrality, respectively. Similarly, the gold and blue lines are for UrQMD calculations of 0-5% and 50-60% centrality, respectively. The Black and grey bars are statistical and systematical uncertainties, respectively. The x axis is the lower cut on rapidity which changes from -0.1 to -0.9 means rapidity window are varied from $-0.1 < y < 0$ to $-0.9 < y < 0$.

With the increase of rapidity window it is seen that cumulants and ratios for both 5% and 50-60% centrality increase while higher order ones decrease early. It is seen at $-0.1 < y < 0$ that all cumulant ratios are consistent with unity (Poisson baseline) which means that the acceptance compared to system correlation length is too small to measure dynamical fluctuation so that the measurement falls to Poisson statistics which has no correlation at all. C_2/C_1 is above unity for most central 5% collisions for each rapidity window which might means there is volume fluctuation effect but it looks the volume fluctuation effect is small for higher-order ratios of C_4/C_2, C_5/C_1 and C_6/C_2. It is worth noting that C_4/C_2 reaches a minimum when $\mathrm{Rapidity_{min}} \approx -0.6$ then goes back to unity when $\mathrm{Rapidity_{min}} \approx -0.9$ with large uncertainty though. C_4/C_2 in UrQMD calculation also shows a similar convergent trend. In general, the rapidity dependence of cumulants and their ratios are qualitatively reproduced by UrQMD calculations.

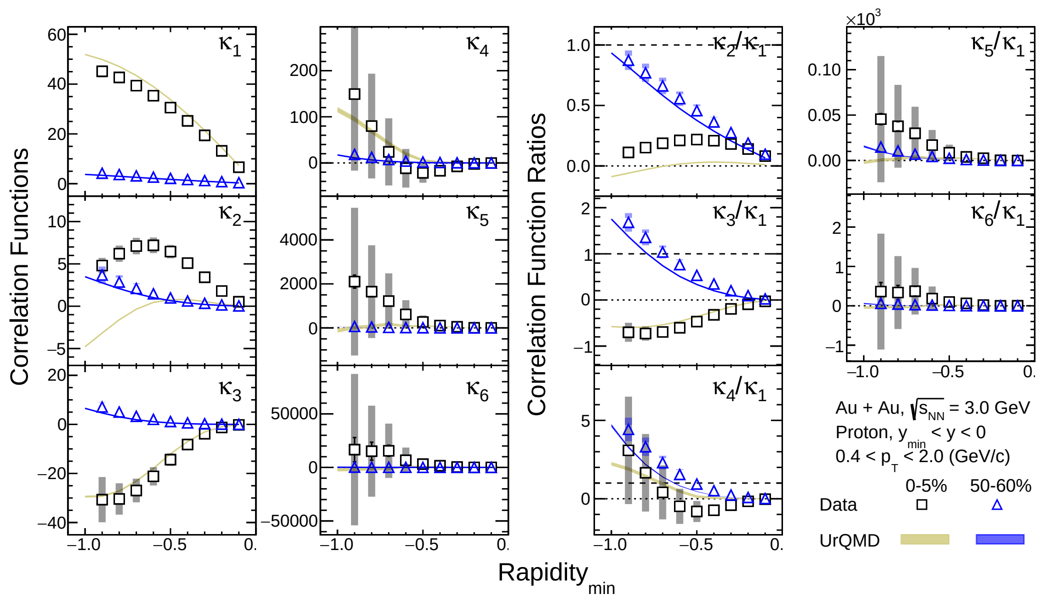

Figure 4.3.2: Rapidity dependence of correlation and correlation function ratios of proton multiplicity distributions up to 6$^{\mathrm{th}}$-order in top 5% central and 50-60% peripheral Au+Au collisions at $\sqrt{s_{\mathrm{NN}}} = 3\,\mathrm{GeV}$ within kinematic acceptance $0.4 < p_{\mathrm{T}} < 2.0\,\mathrm{GeV}/c$. The lower rapidity cut is varied from -0.1 to -0.9. Data are shown with black squares while UrQMD results are shown with gold band. Statistical and systematical uncertainty are shown with black and grey bars, respectively.

Figure 4.3.2 shows rapidity dependence of correlation functions and their normalized ratios (κ_n/κ_1) up to 6th-order in most central 5% and 50-60% peripheral Au+Au collisions at $\sqrt{s_{\rm NN}} = 3$ GeV within kinematic acceptance $0.4 < p_{\rm T} < 2.0$ GeV/c. It is seen that in data two-particle correlation functions (κ_2) for are positive for both top 5% and peripheral centrality from each rapidity window. κ_2 reaches a maximum around when Rapidity$_{\rm min} \approx 0.6$ then decreases when further decreasing Rapidity$_{\rm min}$. κ_2 from UrQMD model also shows a maximum Rapidity$_{\rm min} \approx 0.5$ but decreases to negative when further enlarging rapidity window.

4.4 Transverse Momentum ($p_{\rm T}$) Dependence

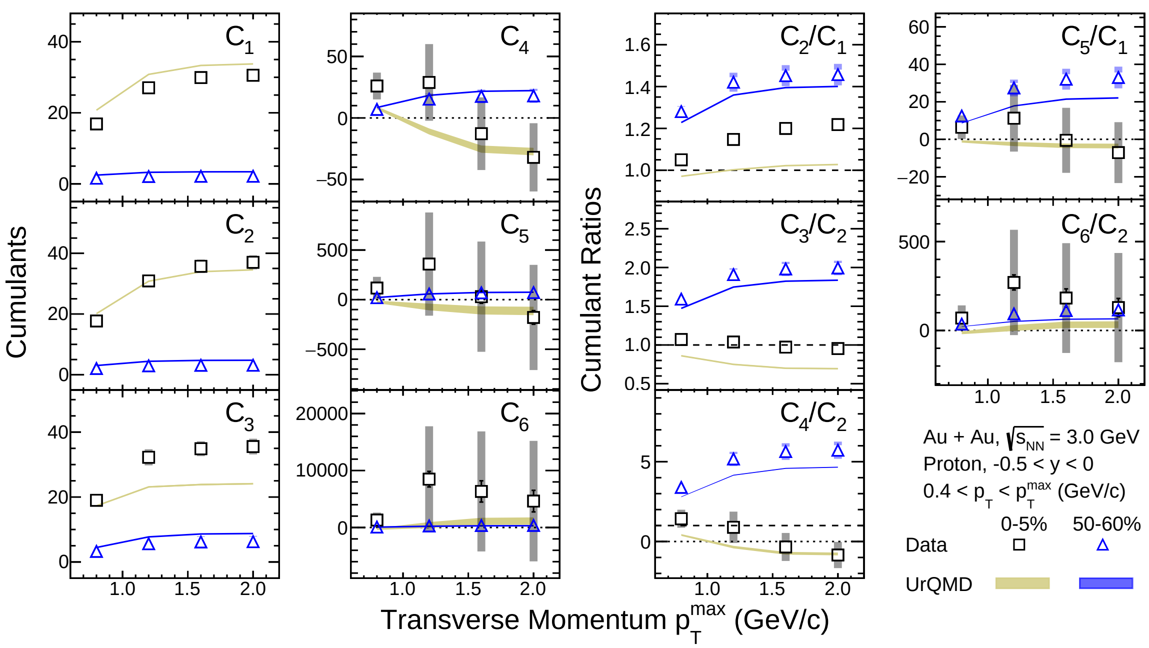

Figure 4.4.1: Transverse momentum ($p_{\rm T}$) dependence of cumulants and their ratios of proton multiplicity distributions up to 6th order in top 5% central and 50-60% peripheral Au+Au collisions at $\sqrt{s_{\rm NN}} = 3$ GeV within kinematic acceptance $-0.5 < y < 0$. The higher $p_{\rm T}$ cut is varied from 0.8 to 2.0 GeV/c. Data are shown with black squares while UrQMD results are shown with gold band. Statistical and systematical uncertainty are shown with black and grey bars, respectively.

Figure 4.4.1 and Fig. 4.4.2 show transverse momentum ($p_{\rm T}$) dependence of cumulants and correlation

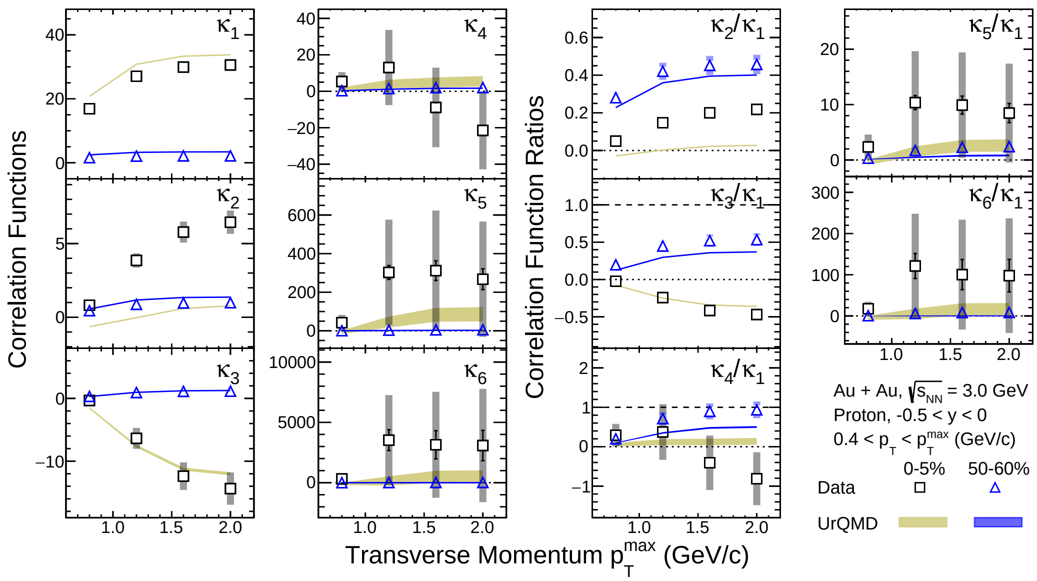

Figure 4.4.2: Transverse momentum (p_T) dependence of correlation function and their normalized ratios of proton multiplicity distributions up to 6th-order in top 5% central and 50-60% peripheral Au+Au collisions at $\sqrt{s_{NN}} = 3$ GeV within kinematic acceptance $-0.5 < y < 0$. The higher p_T cut is varied from 0.8 to 2.0 GeV/c. Data are shown with black squares while UrQMD results are shown with gold band. Statistical and systematical uncertainty are shown with black and grey bars, respectively.

functions of proton multiplicity distributions up to 6$^{\text{th}}$-order in top 5% central and 50-60% peripheral Au+Au collisions at $\sqrt{s_{\text{NN}}} = 3$ GeV within kinematic acceptance $-0.5 < y < 0$. The x axis is a lower cut on p_{T} which varies from 0.8 to 2.0 GeV/c. Cumulants ($C_i, i \leq 3$) increase with increasing p_{T} window while cumulants ($C_i, i \geq 4$) reach a maximum then decrease. Trends of cumulants are reproduced by UrQMD calculation. C_2/C_1 is above unity and increases with increasing p_{T} window, while C_2/C_1 is consistent with unity for all p_{T} window. C_3/C_2 of data is consistent with unity while UrQMD calculation is below unity and show a decreasing trend with increasing p_{T} window. C_4/C_2 is consistent with unity within uncertainty when $p_{\text{T}}^{\text{max}} = 0.8$ and decreases to -1.

4.5 Collision Energy Dependence

New proton results from the 3 GeV collisions are from rapidity window $-0.5 < y < 0$ and p_{T} window $0.4 < p_{\text{T}} < 2.0$ GeV/c and are shown with filled squares. The energy dependence results from UrQMD [58, 59] and hydrodynamic [85] calculations are shown with gold band and red dashed line, respectively. In the hydrodynamic calculation, its evolution is made with the open-source code MUSIC v3.0 [86]. The initial condition is taken from Ref. [87] and the particlization is given by the Cooper-Frye formula [88] with non-ideal hadron resonance gas model [89]. At the grand canonical limit, with including both effects of excluded volume and global baryon number conservation, the net-proton cumulants are evaluated on the Cooper-Frye hypersurface. One may find more details of the model calculations in Ref. [85]. Unlike the commonly used transport model approach, here all calculations, starting from initial condition to hydro-evolution to hadronlization, are all done with the manner of averaged ensembles.

The top panels plots (a) and (b) of Fig. 4.5.1, by definition, are identical(Eq. 1.5.19). Above 7 GeV, all proton and anti-proton κ_2/κ_1 ratios are below zero, and they converge to similar values at top RHIC energy. As the energy decreases, the proton ratio is suppressed and the anti-proton ratio increases slightly and approaches the Poisson limit. The difference becomes largest at 7.7 GeV. The new proton data from 3 GeV Au+Au collisions, shown with filled squares, are found to be positive. The HADES experiment recently reported the measurements of proton ($|y| < 0.4, 0.2 < p_{\text{T}} < 2$ GeV/c) high moments from 2.4 GeV Au+Au top 10% collisions [90] and the value of the κ_2/κ_1 ratio is much larger than 1.

In the energy range 7.7 – 200 GeV, the UrQMD results on the second order ratios show a similar energy dependence although the exact data points are not reproduced. At 3 GeV, within the same acceptance, the UrQMD model calculation on κ_2/κ_1 is also positive (blue cross) and consistent with data. Hydrodynamic model calculations [85], on the other hand, predict negative second order ratios in the entire energy range

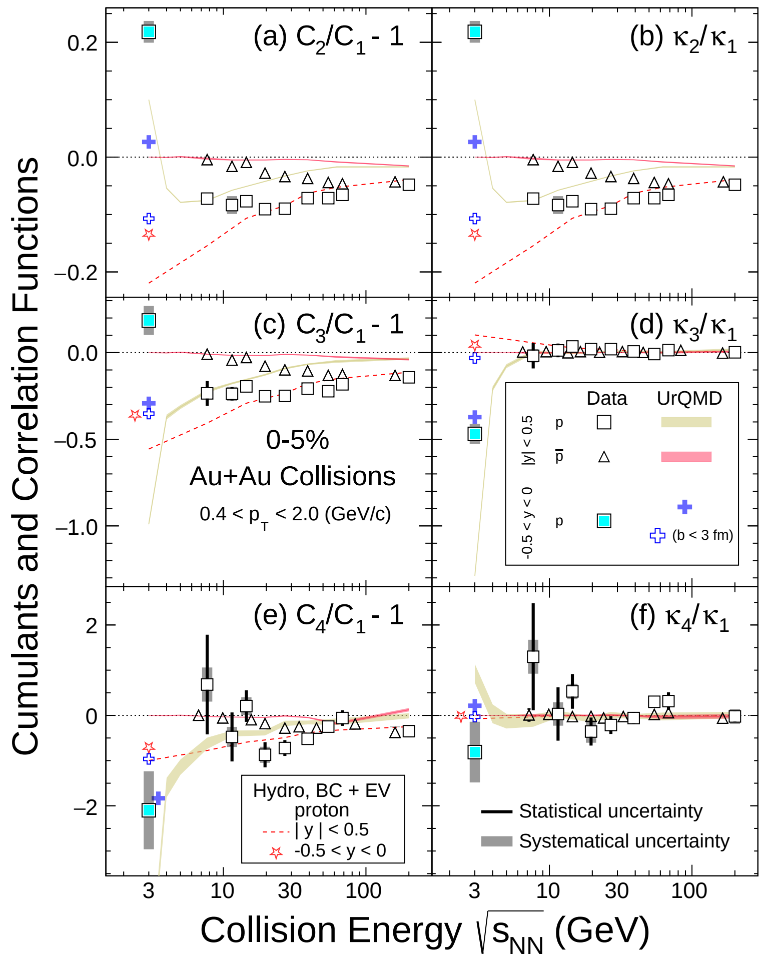

Figure 4.5.1: Collision energy dependence of reduced cumulants ratios and correlation function ratios of (anti)proton multiplicity distributions up to 4^{th}-order in Au+Au collisions within acceptance cut $0.4 < p_T < 2.0$ GeV/c. Results from data with rapidity cut $|y| < 0.5$ are shown with black squares for proton, triangles for antiproton. Results from data and UrQMD model with rapidity cut $-0.5 < y < 0$ are shown with cyan filled squares and blue crosses, respectively. An additional calculation in UrQMD model with impact parameter b < 3 fm is shown with open cross. UrQMD calculations with rapidity cut $|y| < 0.5$ are shown with gold and pink bands for proton and antiproton, respectively. A hydrodynamic calculation is shown with red dashed line for $|y| < 0.5$, red star for $-0.5 < y < 0$. Statistical and systematical uncertainty are shown with black and grey bars, respectively.

3 – 200 GeV, see red dashed lines. By limiting the calculation to half of the nominal rapidity window $-0.5 < y < 0$, the ratio remains negative with a reduced magnitude, see open blue crosses.

As discussed in the previous section, the collision centrality is determined using a similar technique for both UrQMD and data multiplicity distributions. Thus, the sizable volume fluctuations are expected in the UrQMD 3 GeV calculations. In contrast, the hydrodynamic calculations are performed within a fixed volume, but include baryon number conservation and a repulsive volume. In Fig. 4.5.1, the hydrodynamic model predicts negative values for all reduced cumulant ratios [85] (see dashed red lines and open stars). Within the same rapidity window ($-0.5 < y < 0$), the hydro model results (red open stars) are comparable to the UrQMD model calculations with a fixed impact parameter $b < 3$ fm (blue crosses) which corresponds to the top 5% Au+Au central collisions for κ_2/κ_1, κ_3/κ_1, and κ_4/κ_1. Note that the hydrodynamic calculations of cumulants of net-protons are discussed in Fig. 2 of Ref. [85] for the top 5% central Au+Au collisions over the energy range 7.7 – 200 GeV. The trend of the energy dependence in experimental data is well reproduced by the model calculations [85].

At higher energies, the hydrodynamic and UrQMD models appear to agree with each other. In general, it is expected that the effects from volume fluctuation are diminished at higher energy collisions. This could be due to larger multiplicities and the stronger correlation between the reference multiplicity and the initial volume. In addition, the difference between model calculations with and without volume fluctuation corrections is small for higher order reduced cumulants and correlation function ratios due to the cancellation among different orders (Eq. 1.5.19). For example, in panel (e) and (f) in the figure, data points and model results are within the 1σ range. Comparing the reduced cumulant ratios from different orders, one might also conclude that the volume fluctuation in the second order dominates the initial fluctuation in higher orders in low energy nuclear collisions.

In panel (d), the ratios of third order correlation functions are close to zero except for the 3 GeV data. On the other hand, the reduced cumulant ratios in panel (c) show a clear energy dependence similar to that in the top panels. These results imply that the observed energy dependence primarily stems from the second order cumulants and correlation functions. At 3 GeV, the κ_3/κ_1 ratio is well reproduced by the UrQMD calculation. Conversely, the model fails to predict the sign of the reduced cumulant ratio $C_3/C_1 - 1$. In addition, at this energy, the hydrodynamic results show opposite signs of the data in both $C_3/C_1 - 1$ and κ_3/κ_1.

The fourth order results are shown in the bottom panels of Fig. 4.5.1. At collision energy below 20 GeV, the proton κ_4/κ_1 data show hints of non-zero deviations but suffer large statistical uncertainties, see panel (f). At 3 GeV, the proton data is below zero although systematic uncertainty is sizable. Overall, UrQMD calculations are consistent with data. The situation for the reduced cumulant ratio is similar.

In summary, it appears that the second order correlations dominate the energy dependence of the higher order ratios of reduced cumulants and correlation functions. Volume fluctuations are suppressed either in high energy collisions where charged particle multiplicity is large or in higher order correlations due to cancellations. The results from the 3 GeV breaks the systematic energy dependent trends observed in higher energy collisions. This is partly due to the effect of volume fluctuations but also due to that hadronic interactions are dominant in such low energy collisions.

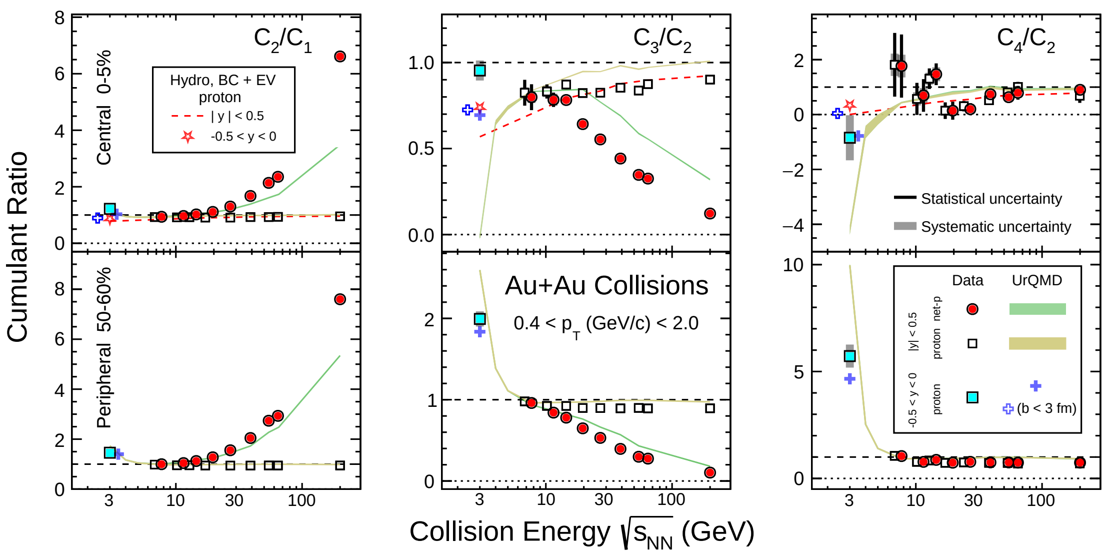

Figure 4.5.2: Collision energy dependence of cumulants ratios up to 4^{th}-order in Au+Au collisions within kinematic acceptance cut $0.4 < p_T < 2.0$ GeV/c. Results from data and Ur within $|y| < 0.5$ are shown with red filled circles for netproton, black squares for proton. Results from data and UrQMD model at with rapidity cut $-0.5 < y < 0$ are shown with filled squares and blue crosses, respectively. An additional calculation in UrQMD model with impact parameter b < 3 fm is shown with open cross. UrQMD calculations with rapidity cut $|y| < 0.5$ are shown with gold and pink bands for proton and antiproton, respectively. A hydrodynamic calculation is shown with red dashed line for $|y| < 0.5$, red star for $-0.5 < y < 0$. Statistical and systematical uncertainty are shown with black and grey bars, respectively.

At first order, taking the ratio of cumulants cancels the effect of volume but not the fluctuations in volume. Fig. 4.5.2 depicts the collision energy dependence of the cumulant ratios from 0-5% central (top panels) and 50-60% peripheral (bottom panels) collisions. The new result of protons from 3 GeV, shown with filled squares, is compared to that of protons (open squares) and net-protons (filled circles) from higher energy ($\sqrt{s_{\rm NN}} = 7.7 - 200$ GeV) collisions.

Transport model UrQMD [58, 59] results of both net-protons (from $|y| < 0.5$) and protons (from 3 GeV within rapidity window $-0.5 < y < 0$) are shown with a gold band and blue cross, respectively. While the net-proton ratios show a clear energy dependence, the proton C_2/C_1 and C_3/C_2 ratios are relatively flat and around unity as a function of collision energy except for the 3 GeV data. This is in contrast to the net-proton ratios which display a clear energy dependence. The new proton data from 3 GeV does not follow this trend in the most central collisions. Notably, both proton (open squares) and net-proton (filled circles) cumulant ratios at collision energies below 20 GeV converge. This implies that at high net-baryon region, the anti-proton production becomes negligible. At the center of mass energy of 2.4 GeV, HADES reported the values for proton cumulant ratios: C_3/C_2 = -1.63 $\pm$ 0.09 (stat) $\pm$ 0.34 (sys) and C_4/C_2 = 0.15 $\pm$ 0.9 (stat) $\pm$ 1.4 (sys) from kinematic acceptance $|y| < 0.4$, $0.4 < p_T < 1.6$ GeV/c [90]. While the value of C_4/C_2 from the HADES experiment is consistent with the 3 GeV new data, the sign of C_3/C_2 is opposite to what we observed here.

Except the C_3/C_2 ratio from central collisions, the transport model UrQMD [58, 59] results reproduce the energy dependence trend well for both proton and net-proton, see green and gold bands in the figure. For the peripheral 50-60% collisions, the C_4/C_2 ratio from 3 GeV is larger than that from higher energy collisions, by a factor of five. A rapid increase in the energy dependence seems confirmed by the UrQMD model calculations, see both the blue cross and gold band in the figure. In the most central collisions at 3 GeV, unlike all higher energy collisions, the value of C_4/C_2 is negative. The UrQMD model calculations, again, reproduced the trend well, due to baryon number conservation, the C_4/C_2 is dramatically suppressed in the high baryon density region.

Hydrodynamic calculations are shown with red dashed lines in Fig. 4.5.2 for the most central 5% Au+Au collisions. The ratios of C_2/C_1, C_3/C_2, and C_4/C_2 in Hydrodynamic calculations are all below unity. Interestingly, the UrQMD result with a fixed impact parameter are also suppressed, see open blue cross. Qualitatively, the results from the fixed volume UrQMD follows that of the Hydro calculations with canonical ensemble.

Initial participant fluctuations can be seen in the ratios for all peripheral collisions and only C_2/C_1 in central collisions. Due to cancellation [82], higher order ratios C_3/C_2 and C_4/C_2 are all suppressed to below unity. In the case of absent or minimal volume fluctuations, calculations of the hydrodynamic model and the UrQMD model with fixed impact parameter are consistent.

At vanishing net-baryon density, first principle Lattice QCD calculations have predicted a positive value of C_4/C_2 from the formation of de-confined QCD matter [91]. The fact that the negative C_4/C_2 value in the most central Au+Au collisions at 3 GeV are reproduced by the hadronic transport UrQMD model although C_3/C_2 is over-predicted, implies that the system is dominant by hadronic interactions. This conclusion is also consistent with that from the measurements of collectivity of light hadrons [92] as well as the strange hadron production [93] at the same collision energy.

Chapter 5

Summary and Outlook

5.1 Summary

In summary, we report a systematic measurement of cumulants and correlation functions of proton multiplicities up to the 6$^{\text{th}}$-order from Au+Au collisions at $\sqrt{s_{\text{NN}}} = 3$ GeV. The data was collected with the STAR fixed-target mode in year 2018 at RHIC. The analysis includes the centrality, acceptance and energy dependence of these fluctuation observables for proton multiplicities. Other important effects which are relevant to low energy fixed-target collisions such as events pileup and volume fluctuation are also discussed.

The protons are identified using the STAR TPC and TOF with greater than 95% purity. The centrality selection is based on pion and kaon multiplicities in the full acceptance of the TPC. The proton tracks are corrected for tracking inefficiencies using a binomial response function. The cumulant values are corrected for pileup contamination. The event-averaged total pileup fraction is determined to be (0.46 ± 0.09)%.

Due to a weak correlation between the measured reference multiplicity and the initial number of participants, a considerable effect from the volume fluctuations is expected. The effects can be suppressed by implementing a model dependent correction procedure [82], however, the results are highly dependent on the choice of model that provides inputs for the correction procedure. Interestingly, higher order cumulant ratios C_4/C_2, C_5/C_1, and C_6/C_2 in most central events appear least affected by volume fluctuations in the 3 GeV collisions.

The proton cumulants and their ratios show a rapidity, transverse momentum, and centrality dependence. The UrQMD model reproduces the trends well, however, does not agree within uncertainties. Comparing with data from higher energy collisions, the $\sqrt{s_{\text{NN}}} = 3$ GeV cumulant ratios of C_2/C_1, C_3/C_2 and

C_4/C_2, except C_3/C_2 in central collisions, UrQMD reproduced all energy dependence. This is attributed to effects from volume fluctuations and hadronic interactions. On the other hand, the data and results of both UrQMD and hydrodynamic models of C_4/C_2 in the most central collisions are consistent which signals the effects of baryon number conservation and an energy regime dominated by hadronic interactions. Therefore, the QCD critical point, if discovered in heavy ion collisions, could only exist at energies higher than 3 GeV.

New data sets have been collected during the second phase of the RHIC beam energy scan program for Au+Au collisions at $\sqrt{s_{\rm NN}} = 3 - 19.6$ GeV. The data sets will have extended kinematic coverage and higher statistics. This will allow analyzers to reduce the statistical uncertainties dramatically and expand the systematic analysis of both p_T and rapidity dependence to wider regions. These studies will be crucial in exploring the QCD phase structure at high baryon density region and locating the illusive critical point.

5.2 Outlook

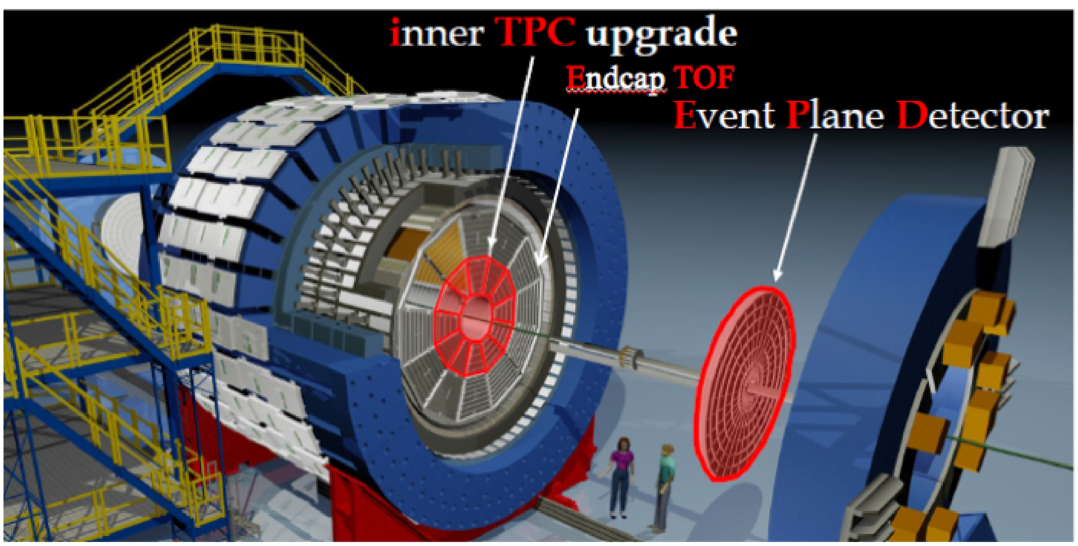

Figure 5.2.1: The upgrades of the STAR detector, iTPC, eTOF and EPD.

From the year 2019 to 2021 RHIC finished data-taking of the beam energy scan program phase II. The collected datasets are 10 – 20 times larger than the statistics from BES-I. The large datasets will allow us to perform high-precision measurements on higher-order cumulants even up to 8$^{\rm th}$ or 10$^{\rm th}$-order. Besides that, in the BES-II STAR upgraded three sub-detectors which are inner TPC detector (iTPC), End Cap TOF

BES-II / BES-I	
$\sqrt{s_{\mathrm{NN}}}$ (GeV)	Statistics (Million)
19.6	400 / 36
17.3	250
14.5	300 / 20
11.5	230 / 12
9.1	160
7.7	100 / 4
13.7 (FXT)	50
11.5 (FXT)	50
9.2 (FXT)	50
7.7 (FXT)	160
6.2 (FXT)	120
5.2 (FXT)	100
4.5 (FXT)	100
3.9 (FXT)	120
3.5 (FXT)	120
3.2 (FXT)	200
3 (FXT)	2000

Table 5.1: Statistics of Au+Au collisions at $\sqrt{s_{\mathrm{NN}}} = 3 - 19.6\,\mathrm{GeV}$ of RHIC beam energy scan program. The BES-II combines both collider and fixed-target configurations of the STAR experiment in order to investigate the nature of the phase transition. The blue and black indicate statistics collected from BES-II and BES-I, respectively.

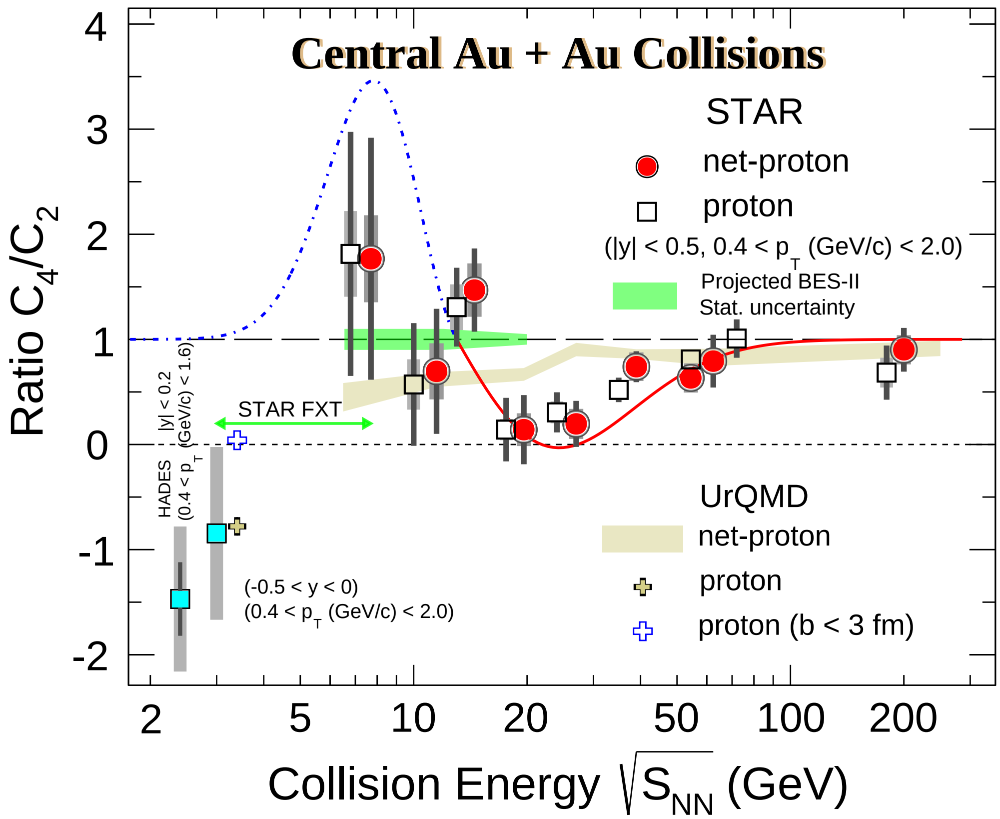

Figure 5.2.2: Energy dependence of $\kappa\sigma^2$ of proton (open squares) and net-proton (red circles) multiplicity distributions in most central 5% centrality class for Au+Au collisions at $\sqrt{s_{NN}} = 7.7 - 200$ GeV. The yellow shaded area indicates the energy region covered by various experiments, CEE, HADES at GSI, CBM at FAIR, NICA at Russia and STAR fixed-target experiment at RHIC.

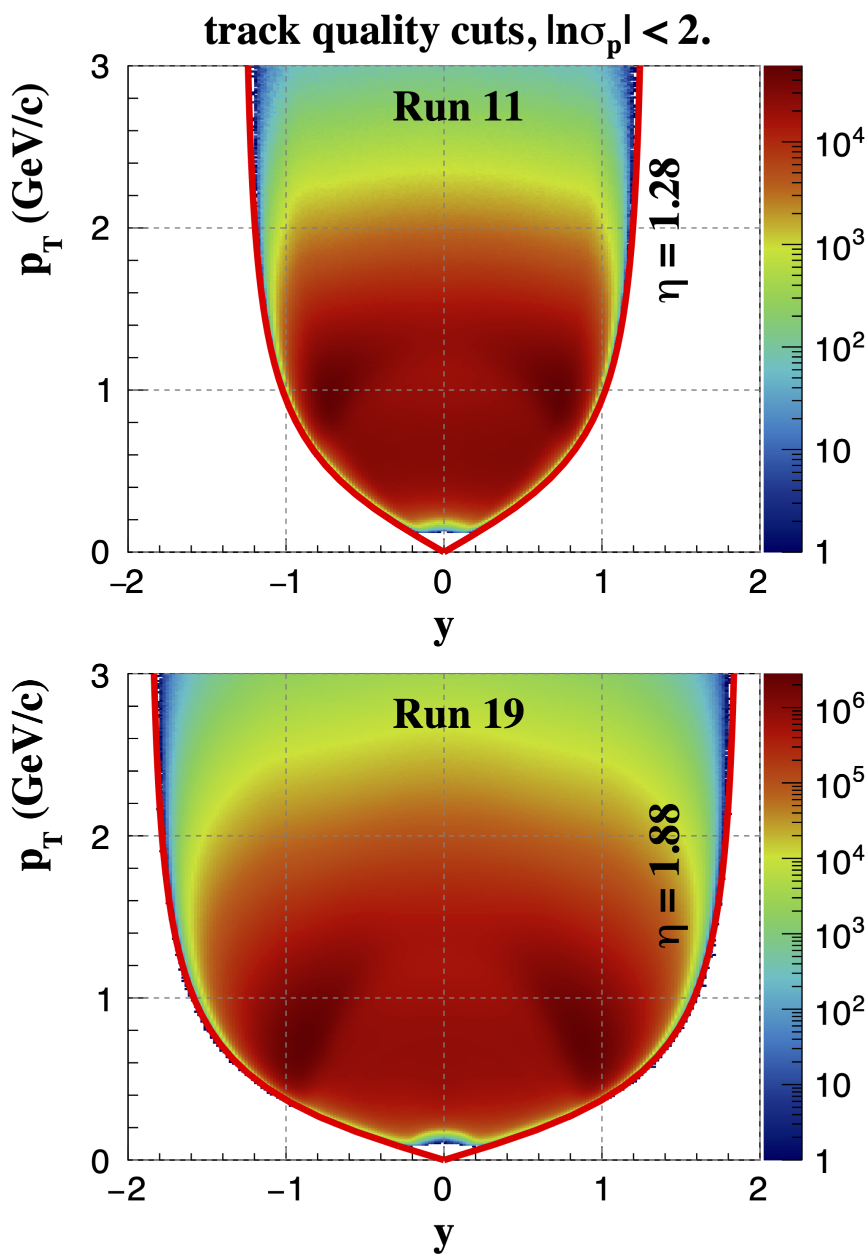

Figure 5.2.3: Proton phase space in Au+Au collisions at $\sqrt{s_{\mathrm{NN}}} = 19.6\,\mathrm{GeV}$ from RHIC-STAR. Protons are selected using TPC PID cut, $|n\sigma_p| < 2$. The top panel is using data from Run 11 while the bottom panel is from Run 19. The red lines in both panels indicate TPC coverage for data from Run 11 and Run 19, respectively.

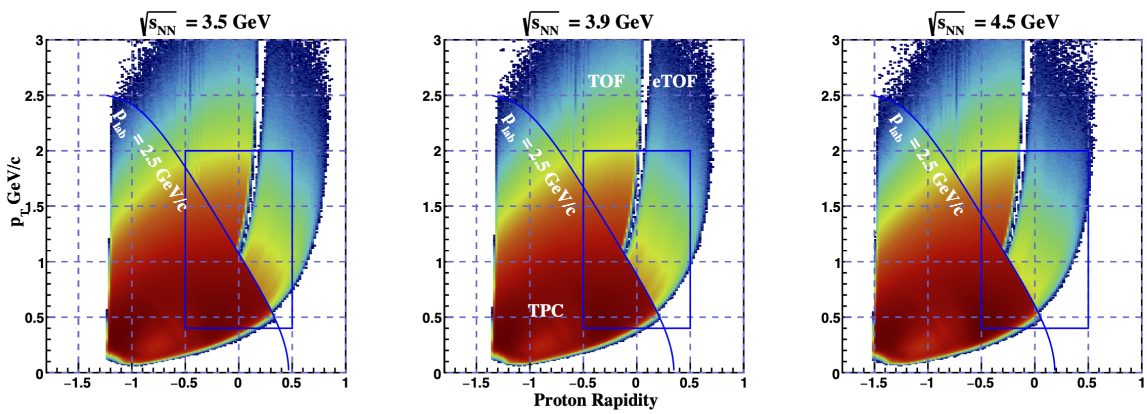

Figure 5.2.4: Proton phase space in Au+Au collisions at $\sqrt{s_{NN}}$ = 3.5, 3.9, and 4.5 GeV by STAR fixed-target experiment. The protons are selected using TPC PID cut, $|n\sigma_p| < 3$. The blue dashed boxes indicate acceptance window for mid-rapidity ($|y| < 0.5$) and $0.4 < p_T < 2.0$ GeV/c. To ensure high-purity proton samples, above total momentum in laboratory frame of 2.5 GeV/c, the TPC, TOF, and eTOF PID are combined to identify protons and below 2 GeV/c only TPC PID is used. For 3 GeV from Run 18 that a cut on momentum 2 GeV/c in laboratory frame is used for TPC, TOF, and eTOF PID.

(eTOF) and Event Plane Detector (EPD).

As is shown in Fig. 5.2.1 the iTPC enlarges TPC rapidity coverage up-to $|\eta| < 1.5$ and has better dE/dx resolution. Fig. 5.2.3 shows proton phase space in Au+Au collisions at $\sqrt{s_{\mathrm{NN}}} = 19.6\,\mathrm{GeV}$ in terms of rapidity (y) and transverse-momentum (p_{T}). The top panel is from Run 11 while the bottom panel is from Run 19 of BES-II. It is seen that with the upgrade of iTPC the rapidity dependence of higher-order cumulants can be scanned up to 0.8. The eTOF enables the particle identification at forward rapidity $-1.6 < \eta < 1.0$. The new installed EPD detectors provide capability to measure charged particles at forward rapidity $2.1 < |\eta| < 5.1$ which may be used to define collision centrality. Fig. 5.2.4 shows the proton phase space in Au+Au collisions at $\sqrt{s_{\mathrm{NN}}} = 3.5$, 3.9, and 4.5 GeV/$c$ from STAR fixed-target experiments in the year 2019 and 2020. In the plot, protons are selected using TPC PID. It can be seen that with the upgrades of iTPC and eTOF up to 4.5 GeV it is still hopeful to measure proton cumulants at mid-rapidity.

The statistics of BES-II program can be seen in Tab. 5.1 where the collision energy varies from 3 up to 19.6 GeV. Fig. 5.2.2 shows the energy dependence of $\kappa\sigma^2$ of proton and net-proton multiplicity distributions in most central 5% Au+Au collisions at $\sqrt{s_{\mathrm{NN}}} = 7.7 - 200\,\mathrm{GeV}$. The yellow shaded area indicates the energy range covered by future experiments like CEE (fixed-target experiment), CBM (fixed-target experiment, $\sqrt{s_{\mathrm{NN}}} = 2 - 5$ GeV), NICA (MPD: collider, $\sqrt{s_{\mathrm{NN}}} = 4 - 11\,\mathrm{GeV}$). The fruitful datasets will allow one to explore QCD phase diagram in high baryon density region, which is the most important region for the search of the illusive QCD critical point.

In this analysis, the initial volume fluctuation effect is discussed and a volume fluctuation correction method is tested in both data and UrQMD model. While as is shown in corresponding chapter this effect is still not well taken care of. In future analysis we will work on this effect for possible solutions. For example if we know precisely the number of participating nucleons (or neutrons) of each collision event then we can use it as a reference for collision centrality. Then the volume fluctuation effect is mostly reduced. It is also pointed in Refs. [94, 95, 96, 97] that strongly intensive cumulants can be used to reduce volume fluctuation effect. The application on the current data still needs more work.

Bibliography

[1] https://commons.wikimedia.org/wiki/File:Standard_Model_of_Elementary_Particles.svg.

[2] Siegfried Bethke. The 2009 World Average of alpha(s). *Eur. Phys. J. C*, 64:689–703, 2009.

[3] I. Arsene et al. Quark gluon plasma and color glass condensate at RHIC? The Perspective from the BRAHMS experiment. *Nucl. Phys. A*, 757:1–27, 2005.

[4] B. B. Back et al. The PHOBOS perspective on discoveries at RHIC. *Nucl. Phys. A*, 757:28–101, 2005.

[5] K. Adcox et al. Formation of dense partonic matter in relativistic nucleus-nucleus collisions at RHIC: Experimental evaluation by the PHENIX collaboration. *Nucl. Phys. A*, 757:184–283, 2005.

[6] John Adams et al. Experimental and theoretical challenges in the search for the quark gluon plasma: The STAR Collaboration's critical assessment of the evidence from RHIC collisions. *Nucl. Phys. A*, 757:102–183, 2005.

[7] Y. Aoki, G. Endrodi, Z. Fodor, S. D. Katz, and K. K. Szabo. The Order of the quantum chromodynamics transition predicted by the standard model of particle physics. *Nature*, 443:675–678, 2006.

[8] Szabocls Borsanyi et al. Full result for the QCD equation of state with 2+1 flavors. *Phys. Lett. B*, 730:99–104, 2014.

[9] Sourendu Gupta et al. Scale for the Phase Diagram of Quantum Chromodynamics. *Science*, 332:1525–1528, 2011.

[10] Szabolcs Borsanyi et al. Is there still any T_c mystery in lattice QCD? Results with physical masses in the continuum limit III. *JHEP*, 09:073, 2010.

[11] A. Bazavov et al. Chiral crossover in QCD at zero and non-zero chemical potentials. *Phys. Lett. B*, 795:15–21, 2019.

[12] Adam Miklos Halasz et al. On the phase diagram of QCD. *Phys. Rev. D*, 58:096007, 1998.

[13] Philippe de Forcrand and Owe Philipsen. The QCD phase diagram for small densities from imaginary chemical potential. *Nucl. Phys. B*, 642:290–306, 2002.

[14] G. Endrodi, Z. Fodor, S. D. Katz, and K. K. Szabo. The QCD phase diagram at nonzero quark density. *JHEP*, 04:001, 2011.

[15] M. Shifman and Boris Ioffe, editors. *At the frontier of particle physics. Handbook of QCD. Vol. 1-3*. World Scientific, Singapore, Singapore, 2001.

[16] Z. Fodor and S. D. Katz. Lattice determination of the critical point of QCD at finite T and mu. *JHEP*, 03:014, 2002.

[17] Misha A. Stephanov, K. Rajagopal, and Edward V. Shuryak. Signatures of the tricritical point in QCD. *Phys. Rev. Lett.*, 81:4816–4819, 1998.

[18] Misha A. Stephanov, K. Rajagopal, and Edward V. Shuryak. Event-by-event fluctuations in heavy ion collisions and the QCD critical point. *Phys. Rev. D*, 60:114028, 1999.

[19] S. Jeon and V. Koch. Fluctuations of particle ratios and the abundance of hadronic resonances. *Phys. Rev. Lett.*, 83:5435–5438, 1999.

[20] Masayuki Asakawa, Ulrich W. Heinz, and Berndt Muller. Fluctuation probes of quark deconfinement. *Phys. Rev. Lett.*, 85:2072–2075, 2000.

[21] V. Koch, A. Majumder, and J. Randrup. Baryon-strangeness correlations: A Diagnostic of strongly interacting matter. *Phys. Rev. Lett.*, 95:182301, 2005.

[22] S. Ejiri, F. Karsch, and K. Redlich. Hadronic fluctuations at the QCD phase transition. *Phys. Lett. B*, 633:275–282, 2006.

[23] Christiana Athanasiou, Krishna Rajagopal, and Misha Stephanov. Using Higher Moments of Fluctuations and their Ratios in the Search for the QCD Critical Point. *Phys. Rev. D*, 82:074008, 2010.

[24] M. A. Stephanov. Non-Gaussian fluctuations near the QCD critical point. *Phys. Rev. Lett.*, 102:032301, 2009.

[25] M. A. Stephanov. On the sign of kurtosis near the QCD critical point. *Phys. Rev. Lett.*, 107:052301, 2011.

[26] B. J. Schaefer and M. Wagner. QCD critical region and higher moments for three flavor models. *Phys. Rev. D*, 85:034027, 2012.

[27] Y. Hatta and M. A. Stephanov. Proton-number fluctuation as a signal of the qcd critical end point. *Phys. Rev. Lett.*, 91:102003, Sep 2003.

[28] Heng-Tong Ding, Frithjof Karsch, and Swagato Mukherjee. Thermodynamics of strong-interaction matter from Lattice QCD. *Int. J. Mod. Phys. E*, 24(10):1530007, 2015.

[29] STAR Note 0598: BES-II whitepaper.

[30] M. M. Aggarwal et al. An Experimental Exploration of the QCD Phase Diagram: The Search for the Critical Point and the Onset of De-confinement. 7 2010.

[31] https://particleadventure.org/history-universe.html.

[32] R. V. Gavai and Sourendu Gupta. Lattice QCD predictions for shapes of event distributions along the freezeout curve in heavy-ion collisions. *Phys. Lett. B*, 696:459–463, 2011.

[33] M. Cheng et al. Baryon Number, Strangeness and Electric Charge Fluctuations in QCD at High Temperature. *Phys. Rev. D*, 79:074505, 2009.

[34] A. Bazavov et al. Fluctuations and Correlations of net baryon number, electric charge, and strangeness: A comparison of lattice QCD results with the hadron resonance gas model. *Phys. Rev. D*, 86:034509, 2012.

[35] A. Bazavov et al. Freeze-out Conditions in Heavy Ion Collisions from QCD Thermodynamics. *Phys. Rev. Lett.*, 109:192302, 2012.

[36] B. Friman, F. Karsch, K. Redlich, and V. Skokov. Fluctuations as probe of the QCD phase transition and freeze-out in heavy ion collisions at LHC and RHIC. *Eur. Phys. J. C*, 71:1694, 2011.

[37] Bengt Friman. Probing the QCD phase diagram with fluctuations. *Nucl. Phys. A*, 928:198–208, 2014.

[38] Swagato Mukherjee, Raju Venugopalan, and Yi Yin. Real time evolution of non-Gaussian cumulants in the QCD critical regime. *Phys. Rev. C*, 92(3):034912, 2015.

[39] Kenji Morita, Bengt Friman, and Krzysztof Redlich. Criticality of the net-baryon number probability distribution at finite density. *Phys. Lett. B*, 741:178–183, 2015.

[40] Masayuki Asakawa, Shinji Ejiri, and Masakiyo Kitazawa. Third moments of conserved charges as probes of QCD phase structure. *Phys. Rev. Lett.*, 103:262301, 2009.

[41] Sangyong Jeon and Volker Koch. *Event by event fluctuations*, pages 430–490. 2004.

[42] M. Consoli. Spontaneous symmetry breaking and the p —> 0 limit. *Phys. Rev. D*, 65:105017, 2002.

[43] Eduardo S. Fraga, Takeshi Kodama, Leticia F. Palhares, and Paul Sorensen. Finite-Size Effects and the Search for the Critical Endpoint of QCD. *PoS*, FACESQCD:017, 2010.

[44] Shu He and Xiaofeng Luo. Proton Cumulants and Correlation Functions in Au + Au Collisions at $\sqrt{s_{\rm NN}}$=7.7-200 GeV from UrQMD Model. *Phys. Lett. B*, 774:623–629, 2017.

[45] Yunxiao Ye et al. Cumulants of the baryon number from central au+au collision at $E_{\rm lab} = 1.23$ gev/nucleon reveal the nuclear mean-field potentials. *Phys. Rev. C*, 98:054620, Nov 2018.

[46] Masakiyo Kitazawa. Rapidity window dependences of higher order cumulants and diffusion master equation. *Nucl. Phys. A*, 942:65–96, 2015.

[47] P. Garg, D. K. Mishra, P. K. Netrakanti, B. Mohanty, A. K. Mohanty, B. K. Singh, and N. Xu. Conserved number fluctuations in a hadron resonance gas model. *Phys. Lett. B*, 726:691–696, 2013.

[48] Marlene Nahrgang, Marcus Bluhm, Paolo Alba, Rene Bellwied, and Claudia Ratti. Impact of resonance regeneration and decay on the net-proton fluctuations in a hadron resonance gas. *Eur. Phys. J. C*, 75(12):573, 2015.

[49] A. Mukherjee, J. Steinheimer, and S. Schramm. Higher-order baryon number susceptibilities: interplay between the chiral and the nuclear liquid-gas transitions. *Phys. Rev. C*, 96(2):025205, 2017.

[50] Swagato Mukherjee, Raju Venugopalan, and Yi Yin. Universal off-equilibrium scaling of critical cumulants in the QCD phase diagram. *Phys. Rev. Lett.*, 117(22):222301, 2016.

[51] Xiaofeng Luo, Bedangadas Mohanty, and Nu Xu. Baseline for the cumulants of net-proton distributions at STAR. *Nucl. Phys. A*, 931:808–813, 2014.

[52] Terence J. Tarnowsky and Gary D. Westfall. First Study of the Negative Binomial Distribution Applied to Higher Moments of Net-charge and Net-proton Multiplicity Distributions. *Phys. Lett. B*, 724:51–55, 2013.

[53] Adam Bzdak, Volker Koch, and Vladimir Skokov. Baryon number conservation and the cumulants of the net proton distribution. *Phys. Rev. C*, 87(1):014901, 2013.

[54] Claude A. Pruneau. Role of baryon number conservation in measurements of fluctuations. *Phys. Rev. C*, 100:034905, Sep 2019.

[55] P. Braun-Munzinger, B. Friman, K. Redlich, A. Rustamov, and J. Stachel. Relativistic nuclear collisions: Establishing a non-critical baseline for fluctuation measurements. *Nucl. Phys.*, A1008:122141, 2021.

[56] M. M. Aggarwal et al. Higher Moments of Net-proton Multiplicity Distributions at RHIC. *Phys. Rev. Lett.*, 105:022302, 2010.

[57] J. Adam et al. Nonmonotonic Energy Dependence of Net-Proton Number Fluctuations. *Phys. Rev. Lett.*, 126(9):092301, 2021.

[58] S. A. Bass et al. Microscopic models for ultrarelativistic heavy ion collisions. *Prog. Part. Nucl. Phys.*, 41:255–369, 1998.

[59] M. Bleicher et al. Relativistic hadron hadron collisions in the ultrarelativistic quantum molecular dynamics model. *J. Phys. G*, 25:1859–1896, 1999.

[60] Jaroslav Adam et al. Flow and interferometry results from Au+Au collisions at $\sqrt{s_{NN}} = 4.5$ GeV. *Phys. Rev. C*, 103(3):034908, 2021.

[61] Arghya Chatterjee et al. Effects of centrality fluctuation and deuteron formation on the proton number cumulant in Au+Au collisions $\sqrt{s_{\mathrm{NN}}} = 3$ GeV from the JAM model. *Chin. Phys. C*, 45(6):064003, 2021.

[62] A. Bazavov et al. Skewness, kurtosis, and the fifth and sixth order cumulants of net baryon-number distributions from lattice QCD confront high-statistics STAR data. *Phys. Rev. D*, 101(7):074502, 2020.

[63] Wei-jie Fu, Xiaofeng Luo, Jan M. Pawlowski, Fabian Rennecke, Rui Wen, and Shi Yin. Hyper-order baryon number fluctuations at finite temperature and density. *Phys. Rev. D*, 104(9):094047, 2021.

[64] Bo Ling and Mikhail A. Stephanov. Acceptance dependence of fluctuation measures near the QCD critical point. *Phys. Rev. C*, 93(3):034915, 2016.

[65] Volker Koch, Adam Bzdak, Dmytro Oliinychenko, and Jan Steinheimer. The QCD phase diagram and statistics friendly distributions. *Nucl. Phys. A*, 1005:121968, 2021.

[66] Adam Bzdak and Volker Koch. Mapping the QCD phase diagram with statistics friendly distributions. *Phys. Rev. C*, 100(5):051902, 2019.

[67] Yutaro Ohnishi, Masakiyo Kitazawa, and Masayuki Asakawa. Thermal blurring of event-by-event fluctuations generated by rapidity conversion. *Phys. Rev. C*, 94(4):044905, 2016.

[68] https://www.bnl.gov/newsroom/news.php?a=119262.

[69] M. Anderson et al. The Star time projection chamber: A Unique tool for studying high multiplicity events at RHIC. *Nucl. Instrum. Meth. A*, 499:659–678, 2003.

[70] H. Bichsel. A method to improve tracking and particle identification in TPCs and silicon detectors. *Nucl. Instrum. Meth. A*, 562:154–197, 2006.

[71] J. Adamczewski-Musch et al. Proton-number fluctuations in $\sqrt{s_{NN}}$ =2.4 GeV Au + Au collisions studied with the High-Acceptance DiElectron Spectrometer (HADES). *Phys. Rev. C*, 102(2):024914, 2020.

[72] Xiaofeng Luo, Ji Xu, Bedangadas Mohanty, and Nu Xu. Volume fluctuation and auto-correlation effects in the moment analysis of net-proton multiplicity distributions in heavy-ion collisions. *J. Phys. G*, 40:105104, 2013.

[73] V FINE and P NEVSKI. Oo model of star detector for simulation, visualization and reconstruction., 2 2000.

[74] Mohamed Abdallah et al. Cumulants and correlation functions of net-proton, proton, and antiproton multiplicity distributions in Au+Au collisions at energies available at the BNL Relativistic Heavy Ion Collider. *Phys. Rev. C*, 104(2):024902, 2021.

[75] Xiaofeng Luo. Unified description of efficiency correction and error estimation for moments of conserved quantities in heavy-ion collisions. *Phys. Rev. C*, 91(3):034907, 2015. [Erratum: Phys.Rev.C 94, 059901 (2016)].

[76] Toshihiro Nonaka, Masakiyo Kitazawa, and ShinIchi Esumi. More efficient formulas for efficiency correction of cumulants and effect of using averaged efficiency. *Phys. Rev. C*, 95(6):064912, 2017. [Erratum: Phys.Rev.C 103, 029901 (2021)].

[77] Xiaofeng Luo and Toshihiro Nonaka. Efficiency correction for cumulants of multiplicity distributions based on track-by-track efficiency. *Phys. Rev. C*, 99(4):044917, 2019.

[78] Toshihiro Nonaka, Masakiyo Kitazawa, and ShinIchi Esumi. Pileup corrections on higher-order cumulants. *Nucl. Instrum. Meth. A*, 984:164632, 2020.

[79] Yu Zhang, Yige Huang, Toshihiro Nonaka, and Xiaofeng Luo. Pileup Correction on Higher-order Cumulants with Unfolding Approach. *Nucl. Instrum. Meth. A*, 1026:166246, 8 2021.

[80] ShinIchi Esumi, Kana Nakagawa, and Toshihiro Nonaka. Reconstructing particle number distributions with convoluting volume fluctuations. *Nucl. Instrum. Meth. A*, 987:164802, 2021.

[81] A. Bialas, M. Bleszynski, and W. Czyz. Multiplicity Distributions in Nucleus-Nucleus Collisions at High-Energies. *Nucl. Phys. B*, 111:461–476, 1976.

[82] P. Braun-Munzinger, A. Rustamov, and J. Stachel. Bridging the gap between event-by-event fluctuation measurements and theory predictions in relativistic nuclear collisions. *Nucl. Phys. A*, 960:114–130, 2017.

[83] B. Efron and R.J. Tibshirani. Chapman & Hall/CRC Monographs on Statistics & Applied Probability. Taylor & Francis, 1994. https://doi.org/10.1201/9780429246593.

[84] Xiaofeng Luo. Error Estimation for Moments Analysis in Heavy Ion Collision Experiment. *J. Phys. G*, 39:025008, 2012.

[85] Volodymyr Vovchenko, Volker Koch, and Chun Shen. Proton number cumulants and correlation functions in Au-Au collisions at sNN=7.7–200 GeV from hydrodynamics. *Phys. Rev. C*, 105(1):014904, 2022.

[86] Gabriel S. Denicol et al. Net baryon diffusion in fluid dynamic simulations of relativistic heavy-ion collisions. *Phys. Rev. C*, 98(3):034916, 2018.

[87] Chun Shen and Sahr Alzhrani. Collision-geometry-based 3D initial condition for relativistic heavy-ion collisions. *Phys. Rev. C*, 102(1):014909, 2020.

[88] Fred Cooper and Graham Frye. Comment on the Single Particle Distribution in the Hydrodynamic and Statistical Thermodynamic Models of Multiparticle Production. *Phys. Rev. D*, 10:186, 1974.

[89] Volodymyr Vovchenko et al. Repulsive baryonic interactions and lattice QCD observables at imaginary chemical potential. *Phys. Lett. B*, 775:71–78, 2017.

[90] Adamczewski-Musch et al. *Phys. Rev. C*, 102:024914, Aug 2020.

[91] F. Karsch and K. Redlich. Probing freeze-out conditions in heavy ion collisions with moments of charge fluctuations. *Phys. Lett. B*, 695(1):136–142, 2011.

[92] M. S. Abdallah et al. Disappearance of partonic collectivity in sNN=3GeV Au+Au collisions at RHIC. *Phys. Lett. B*, 827:137003, 2022.

[93] Mohamed Abdallah et al. Probing Strangeness Canonical Ensemble with K^-, $\phi(1020)$ and Ξ^- Production in Au+Au Collisions at $\sqrt{s_{NN}} = 3\,GeV$. 8 2021.

[94] M. Gazdzicki and S. Mrowczynski. A Method to study 'equilibration' in nucleus-nucleus collisions. *Z. Phys. C*, 54:127–132, 1992.

[95] M. I. Gorenstein and M. Gazdzicki. Strongly Intensive Quantities. *Phys. Rev. C*, 84:014904, 2011.

[96] Evan Sangaline. Strongly Intensive Cumulants: Fluctuation Measures for Systems With Incompletely Constrained Volumes. 5 2015.

[97] M. Mackowiak-Pawlowska, M. Naskręt, and M. Gazdzicki. Remarks on volume fluctuations in fixed-target heavy-ion experiments. *Nucl. Phys. A*, 1014:122258, 2021.

[98] https://www.python.org.

[99] https://www.sympy.org/en/index.html.

[100] https://gitlab.com/yzh2021/cumulantsformulas.

Appendix

Statistical Uncertainty of Efficiency Uncorrected Cumulants

Below we show formulas for statistical uncertainty of detector efficiency uncorrected cumulants and correlation functions up to 8^{th} order. The "Var" indicates variance. μ, $\langle N \rangle$ and n represent central moment, mean value and number of events. The formulas given in this section are used to evaluate statistical uncertainty for cumulants and correlation functions given in Sec. 1.5.1 and Sec. 1.5.2.

$$
\begin{aligned}
\mathrm{Var}(C2) &= (-\mu_2^2 + \mu_4)/n, \\
\mathrm{Var}(C3) &= (9\mu_2^3 - 6\mu_2\mu_4 - \mu_3^2 + \mu_6)/n, \\
\mathrm{Var}(C4) &= (-36\mu_2^4 + 48\mu_2^2\mu_4 + 64\mu_2\mu_3^2 - 12\mu_2\mu_6 - 8\mu_3\mu_5 - \mu_4^2 + \mu_8)/n, \\
\mathrm{Var}(C5) &= (\mu_{10} + 900\mu_2^5 - 900\mu_2^3\mu_4 - 1000\mu_2^2\mu_3^2 + 160\mu_2^2\mu_6 + 240\mu_2\mu_3\mu_5 \\
&\quad + 125\mu_2\mu_4^2 - 20\mu_2\mu_8 + 200\mu_3^2\mu_4 - 20\mu_3\mu_7 - 10\mu_4\mu_6 - \mu_5^2)/n, \\
\mathrm{Var}(C6) &= (-30\mu_{10}\mu_2 + \mu_{12} - 8100\mu_2^6 + 13500\mu_2^4\mu_4 + 39600\mu_2^3\mu_3^2 - 2880\mu_2^3\mu_6 \\
&\quad - 9720\mu_2^2\mu_3\mu_5 - 3600\mu_2^2\mu_4^2 + 405\mu_2^2\mu_8 - 9600\mu_2\mu_3^2\mu_4 + 840\mu_2\mu_3\mu_7 + 510\mu_2\mu_4\mu_6 \\
&\quad + 216\mu_2\mu_5^2 - 400\mu_3^4 + 440\mu_3^2\mu_6 + 1020\mu_3\mu_4\mu_5 - 40\mu_3\mu_9 + 225\mu_4^3 - 30\mu_4\mu_8 \\
&\quad - 12\mu_5\mu_7 - \mu_6^2)/n, \\
\mathrm{Var}(C7) &= (861\mu_{10}\mu_2^2 - 70\mu_{10}\mu_4 - 70\mu_{11}\mu_3 - 42\mu_{12}\mu_2 + \mu_{14} + 396900\mu_2^7 - 529200\mu_2^5\mu_4 \\
&\quad - 1102500\mu_2^4\mu_3^2 + 79380\mu_2^4\mu_6 + 299880\mu_2^3\mu_3\mu_5 + 176400\mu_2^3\mu_4^2 - 10080\mu_2^3\mu_8 \\
&\quad + 558600\mu_2^2\mu_3^2\mu_4 - 33600\mu_2^2\mu_3\mu_7 - 29400\mu_2^2\mu_4\mu_6 - 10584\mu_2^2\mu_5^2 + 137200\mu_2\mu_3^4 \\
&\quad - 43120\mu_2\mu_3^2\mu_6 - 76440\mu_2\mu_3\mu_4\mu_5 + 2310\mu_2\mu_3\mu_9 - 14700\mu_2\mu_4^3 \\
&\quad + 1890\mu_2\mu_4\mu_8 + 966\mu_2\mu_5\mu_7 + 343\mu_2\mu_6^2 - 15680\mu_3^3\mu_5 - 14700\mu_3^2\mu_4^2 \\
&\quad + 1505\mu_3^2\mu_8 + 2590\mu_3\mu_4\mu_7 + 2254\mu_3\mu_5\mu_6 + 1715\mu_4^2\mu_6 + 1911\mu_4\mu_5^2
\end{aligned}
$$

$$
\begin{aligned}
&- 42\mu_5\mu_9 - 14\mu_6\mu_8 - \mu_7^2)/n,\\
\mathrm{Var}(C8) &= (-28560\mu_{10}\mu_2^3 + 5600\mu_{10}\mu_2\mu_4 + 4256\mu_{10}\mu_3^2 - 56\mu_{10}\mu_6 + 5376\mu_{11}\mu_2\mu_3 - 112\mu_{11}\mu_5\\
&+ 1624\mu_{12}\mu_2^2 - 140\mu_{12}\mu_4 - 112\mu_{13}\mu_3 - 56\mu_{14}\mu_2 + \mu_{16} - 6350400\mu_2^8 + 12700800\mu_2^6\mu_4\\
&+ 59270400\mu_2^5\mu_3^2 - 2399040\mu_2^5\mu_6 - 15523200\mu_2^4\mu_3\mu_5 - 6174000\mu_2^4\mu_4^2 + 322560\mu_2^4\mu_8\\
&- 35280000\mu_2^3\mu_3^2\mu_4 + 1626240\mu_2^3\mu_3\mu_7 + 1340640\mu_2^3\mu_4\mu_6 + 677376\mu_2^3\mu_5^2 - 8467200\mu_2^2\mu_3^4\\
&+ 2759680\mu_2^2\mu_3^2\mu_6 + 5597760\mu_2^2\mu_3\mu_4\mu_5 - 119840\mu_2^2\mu_3\mu_9 + 882000\mu_2^2\mu_4^3 - 108360\mu_2^2\mu_4\mu_8\\
&- 77952\mu_2^2\mu_5\mu_7 - 26656\mu_2^2\mu_6^2 + 2007040\mu_2\mu_3^3\mu_5 + 3684800\mu_2\mu_3^2\mu_4^2 - 160160\mu_2\mu_3^2\mu_8\\
&- 322560\mu_2\mu_3\mu_4\mu_7 - 257152\mu_2\mu_3\mu_5\mu_6 - 172480\mu_2\mu_4^2\mu_6 - 178752\mu_2\mu_4\mu_5^2 + 3808\mu_2\mu_5\mu_9\\
&+ 1680\mu_2\mu_6\mu_8 + 512\mu_2\mu_7^2 + 940800\mu_3^4\mu_4 - 71680\mu_3^3\mu_7 - 203840\mu_3^2\mu_4\mu_6 - 75264\mu_3^2\mu_5^2\\
&- 156800\mu_3\mu_4^2\mu_5 + 8960\mu_3\mu_4\mu_9 + 6496\mu_3\mu_5\mu_8 + 4480\mu_3\mu_6\mu_7 - 4900\mu_4^4 + 5040\mu_4^2\mu_8\\
&+ 9856\mu_4\mu_5\mu_7 + 4704\mu_4\mu_6^2 + 6272\mu_5^2\mu_6 - 16\mu_7\mu_9 - \mu_8^2)/n,\\
\mathrm{Var}(C2/C1) &= (-\frac{\mu_2^2}{\langle N\rangle^2} + \frac{\mu_4}{\langle N\rangle^2} - \frac{2\mu_2\mu_3}{\langle N\rangle^3} + \frac{\mu_2^3}{\langle N\rangle^4})/n,\\
\mathrm{Var}(C3/C2) &= (9\mu_2 - \frac{6\mu_4}{\mu_2} + \frac{6\mu_3^2}{\mu_2^2} + \frac{\mu_6}{\mu_2^2} - \frac{2\mu_3\mu_5}{\mu_2^3} + \frac{\mu_3^2\mu_4}{\mu_2^4})/n,\\
\mathrm{Var}(C4/C2) &= (-9\mu_2^2 + 9\mu_4 + \frac{40\mu_3^2}{\mu_2} - \frac{6\mu_6}{\mu_2} - \frac{8\mu_3\mu_5}{\mu_2^2} + \frac{6\mu_4^2}{\mu_2^2} + \frac{\mu_8}{\mu_2^2} + \frac{8\mu_3^2\mu_4}{\mu_2^3} - \frac{2\mu_4\mu_6}{\mu_2^3} + \frac{\mu_4^3}{\mu_2^4})/n,\\
\mathrm{Var}(C5/C1) &= (\frac{\mu_{10}}{\langle N\rangle^2} + \frac{900\mu_2^5}{\langle N\rangle^2} - \frac{900\mu_2^3\mu_4}{\langle N\rangle^2} - \frac{1000\mu_2^2\mu_3^2}{\langle N\rangle^2} + \frac{160\mu_2^2\mu_6}{\langle N\rangle^2} + \frac{240\mu_2\mu_3\mu_5}{\langle N\rangle^2} + \frac{125\mu_2\mu_4^2}{\langle N\rangle^2}\\
&- \frac{20\mu_2\mu_8}{\langle N\rangle^2} + \frac{200\mu_3^2\mu_4}{\langle N\rangle^2} - \frac{20\mu_3\mu_7}{\langle N\rangle^2} - \frac{10\mu_4\mu_6}{\langle N\rangle^2} - \frac{\mu_5^2}{\langle N\rangle^2} + \frac{600\mu_2^4\mu_3}{\langle N\rangle^3}\\
&- \frac{60\mu_2^3\mu_5}{\langle N\rangle^3} - \frac{300\mu_2^2\mu_3\mu_4}{\langle N\rangle^3} - \frac{200\mu_2\mu_3^3}{\langle N\rangle^3} + \frac{20\mu_2\mu_3\mu_6}{\langle N\rangle^3} + \frac{30\mu_2\mu_4\mu_5}{\langle N\rangle^3}\\
&+ \frac{20\mu_3^2\mu_5}{\langle N\rangle^3} - \frac{2\mu_5\mu_6}{\langle N\rangle^3} + \frac{100\mu_2^3\mu_3^2}{\langle N\rangle^4} - \frac{20\mu_2^2\mu_3\mu_5}{\langle N\rangle^4} + \frac{\mu_2\mu_5^2}{\langle N\rangle^4})/n,\\
\mathrm{Var}(C6/C2) &= (-\frac{30\mu_{10}}{\mu_2} + \frac{\mu_{12}}{\mu_2^2} - 3600\mu_2^4 + 5400\mu_2^2\mu_4 + 30000\mu_2\mu_3^2 - 1800\mu_2\mu_6\\
&- 8160\mu_3\mu_5 - 225\mu_4^2 + 345\mu_8 - \frac{3900\mu_3^2\mu_4}{\mu_2} + \frac{840\mu_3\mu_7}{\mu_2} - \frac{120\mu_4\mu_6}{\mu_2}\\
&+ \frac{216\mu_5^2}{\mu_2} + \frac{2300\mu_3^4}{\mu_2^2} - \frac{140\mu_3^2\mu_6}{\mu_2^2} + \frac{240\mu_3\mu_4\mu_5}{\mu_2^2} - \frac{40\mu_3\mu_9}{\mu_2^2} - \frac{12\mu_5\mu_7}{\mu_2^2}\\
&+ \frac{30\mu_6^2}{\mu_2^2} - \frac{520\mu_3^3\mu_5}{\mu_2^3} + \frac{20\mu_3^2\mu_8}{\mu_2^3} + \frac{52\mu_3\mu_5\mu_6}{\mu_2^3} - \frac{2\mu_6\mu_8}{\mu_2^3} + \frac{100\mu_3^4\mu_4}{\mu_2^4} - \frac{20\mu_3^2\mu_4\mu_6}{\mu_2^4} + \frac{\mu_4\mu_6^2}{\mu_2^4})/n,\\
\mathrm{Var}(C7/C1) &= (\frac{861\mu_{10}\mu_2^2}{\langle N\rangle^2} - \frac{70\mu_{10}\mu_4}{\langle N\rangle^2} - \frac{70\mu_{11}\mu_3}{\langle N\rangle^2} - \frac{42\mu_{12}\mu_2}{\langle N\rangle^2} + \frac{\mu_{14}}{\langle N\rangle^2} + \frac{396900\mu_2^7}{\langle N\rangle^2} - \frac{529200\mu_2^5\mu_4}{\langle N\rangle^2}
\end{aligned}
$$

$$
\begin{aligned}
&-\frac{1102500\mu_2^4\mu_3^2}{\langle N\rangle^2}+\frac{79380\mu_2^4\mu_6}{\langle N\rangle^2}+\frac{299880\mu_2^3\mu_3\mu_5}{\langle N\rangle^2}+\frac{176400\mu_2^3\mu_4^2}{\langle N\rangle^2}-\frac{10080\mu_2^3\mu_8}{\langle N\rangle^2}\\
&+\frac{558600\mu_2^2\mu_3^2\mu_4}{\langle N\rangle^2}-\frac{33600\mu_2^2\mu_3\mu_7}{\langle N\rangle^2}-\frac{29400\mu_2^2\mu_4\mu_6}{\langle N\rangle^2}-\frac{10584\mu_2^2\mu_5^2}{\langle N\rangle^2}+\frac{137200\mu_2\mu_3^4}{\langle N\rangle^2}\\
&-\frac{43120\mu_2\mu_3^2\mu_6}{\langle N\rangle^2}-\frac{76440\mu_2\mu_3\mu_4\mu_5}{\langle N\rangle^2}+\frac{2310\mu_2\mu_3\mu_9}{\langle N\rangle^2}-\frac{14700\mu_2\mu_4^3}{\langle N\rangle^2}+\frac{1890\mu_2\mu_4\mu_8}{\langle N\rangle^2}\\
&+\frac{966\mu_2\mu_5\mu_7}{\langle N\rangle^2}+\frac{343\mu_2\mu_6^2}{\langle N\rangle^2}-\frac{15680\mu_3^3\mu_5}{\langle N\rangle^2}-\frac{14700\mu_3^2\mu_4^2}{\langle N\rangle^2}+\frac{1505\mu_3^2\mu_8}{\langle N\rangle^2}+\frac{2590\mu_3\mu_4\mu_7}{\langle N\rangle^2}\\
&+\frac{2254\mu_3\mu_5\mu_6}{\langle N\rangle^2}+\frac{1715\mu_4^2\mu_6}{\langle N\rangle^2}+\frac{1911\mu_4\mu_5^2}{\langle N\rangle^2}-\frac{42\mu_5\mu_9}{\langle N\rangle^2}-\frac{14\mu_6\mu_8}{\langle N\rangle^2}-\frac{\mu_7^2}{\langle N\rangle^2}+\frac{264600\mu_2^6\mu_3}{\langle N\rangle^3}\\
&-\frac{26460\mu_2^5\mu_5}{\langle N\rangle^3}-\frac{220500\mu_2^4\mu_3\mu_4}{\langle N\rangle^3}+\frac{1260\mu_2^4\mu_7}{\langle N\rangle^3}-\frac{235200\mu_2^3\mu_3^3}{\langle N\rangle^3}+\frac{11760\mu_2^3\mu_3\mu_6}{\langle N\rangle^3}\\
&+\frac{17640\mu_2^3\mu_4\mu_5}{\langle N\rangle^3}+\frac{47040\mu_2^2\mu_3^2\mu_5}{\langle N\rangle^3}+\frac{44100\mu_2^2\mu_3\mu_4^2}{\langle N\rangle^3}-\frac{420\mu_2^2\mu_3\mu_8}{\langle N\rangle^3}-\frac{840\mu_2^2\mu_4\mu_7}{\langle N\rangle^3}\\
&-\frac{1176\mu_2^2\mu_5\mu_6}{\langle N\rangle^3}+\frac{39200\mu_2\mu_3^3\mu_4}{\langle N\rangle^3}-\frac{1120\mu_2\mu_3^2\mu_7}{\langle N\rangle^3}-\frac{1960\mu_2\mu_3\mu_4\mu_6}{\langle N\rangle^3}-\frac{2352\mu_2\mu_3\mu_5^2}{\langle N\rangle^3}\\
&-\frac{1470\mu_2\mu_4^2\mu_5}{\langle N\rangle^3}+\frac{42\mu_2\mu_5\mu_8}{\langle N\rangle^3}+\frac{56\mu_2\mu_6\mu_7}{\langle N\rangle^3}-\frac{3920\mu_3^2\mu_4\mu_5}{\langle N\rangle^3}-\frac{2450\mu_3\mu_4^3}{\langle N\rangle^3}+\frac{70\mu_3\mu_4\mu_8}{\langle N\rangle^3}\\
&+\frac{112\mu_3\mu_5\mu_7}{\langle N\rangle^3}+\frac{70\mu_4^2\mu_7}{\langle N\rangle^3}-\frac{2\mu_7\mu_8}{\langle N\rangle^3}+\frac{44100\mu_2^5\mu_3^2}{\langle N\rangle^4}-\frac{8820\mu_2^4\mu_3\mu_5}{\langle N\rangle^4}-\frac{14700\mu_2^3\mu_3^2\mu_4}{\langle N\rangle^4}\\
&+\frac{420\mu_2^3\mu_3\mu_7}{\langle N\rangle^4}+\frac{441\mu_2^3\mu_5^2}{\langle N\rangle^4}+\frac{1470\mu_2^2\mu_3\mu_4\mu_5}{\langle N\rangle^4}\\
&-\frac{42\mu_2^2\mu_5\mu_7}{\langle N\rangle^4}+\frac{1225\mu_2\mu_3^2\mu_4^2}{\langle N\rangle^4}-\frac{70\mu_2\mu_3\mu_4\mu_7}{\langle N\rangle^4}+\frac{\mu_2\mu_7^2}{\langle N\rangle^4})/n,\\
\mathrm{Var}(C8/C2)=&(-27300\mu_{10}\mu_2+\frac{4760\mu_{10}\mu_4}{\mu_2}+\frac{3136\mu_{10}\mu_3^2}{\mu_2^2}+\frac{112\mu_{10}\mu_3\mu_5}{\mu_2^3}+\frac{70\mu_{10}\mu_4^2}{\mu_2^3}-\frac{2\mu_{10}\mu_8}{\mu_2^3}\\
&+\frac{5376\mu_{11}\mu_3}{\mu_2}-\frac{112\mu_{11}\mu_5}{\mu_2^2}+1624\mu_{12}-\frac{140\mu_{12}\mu_4}{\mu_2^2}-\frac{112\mu_{13}\mu_3}{\mu_2^2}-\frac{56\mu_{14}}{\mu_2}+\frac{\mu_{16}}{\mu_2^2}\\
&-3572100\mu_2^6+6747300\mu_2^4\mu_4+48686400\mu_2^3\mu_3^2-1693440\mu_2^3\mu_6-13335840\mu_2^2\mu_3\mu_5\\
&-2425500\mu_2^2\mu_4^2+282240\mu_2^2\mu_8-25166400\mu_2\mu_3^2\mu_4+1545600\mu_2\mu_3\mu_7+664440\mu_2\mu_4\mu_6\\
&+606816\mu_2\mu_5^2-1254400\mu_3^4+1881600\mu_3^2\mu_6+3974880\mu_3\mu_4\mu_5-119840\mu_3\mu_9+102900\mu_4^3\\
&-78540\mu_4\mu_8-77952\mu_5\mu_7-784\mu_6^2-\frac{439040\mu_3^3\mu_5}{\mu_2}+\frac{1764000\mu_3^2\mu_4^2}{\mu_2}-\frac{115360\mu_3^2\mu_8}{\mu_2}\\
&-\frac{268800\mu_3\mu_4\mu_7}{\mu_2}-\frac{119168\mu_3\mu_5\mu_6}{\mu_2}-\frac{31360\mu_4^2\mu_6}{\mu_2}-\frac{131712\mu_4\mu_5^2}{\mu_2}+\frac{3808\mu_5\mu_9}{\mu_2}\\
&-\frac{840\mu_6\mu_8}{\mu_2}+\frac{512\mu_7^2}{\mu_2}-\frac{62720\mu_3^2\mu_4\mu_6}{\mu_2^2}+\frac{159936\mu_3^2\mu_5^2}{\mu_2^2}+\frac{3920\mu_3\mu_4^2\mu_5}{\mu_2^2}+\frac{8960\mu_3\mu_4\mu_9}{\mu_2^2}
\end{aligned}
$$

$$
\begin{aligned}
&+\frac{224\mu_3\mu_5\mu_8}{\mu_2^2}+\frac{896\mu_3\mu_6\mu_7}{\mu_2^2}+\frac{28175\mu_4^4}{\mu_2^2}+\frac{2100\mu_4^2\mu_8}{\mu_2^2}+\frac{9856\mu_4\mu_5\mu_7}{\mu_2^2}+\frac{3136\mu_5^2\mu_6}{\mu_2^2}\\
&-\frac{16\mu_7\mu_9}{\mu_2^2}+\frac{56\mu_8^2}{\mu_2^2}+\frac{62720\mu_3^3\mu_4\mu_5}{\mu_2^3}+\frac{39200\mu_3^2\mu_4^3}{\mu_2^3}-\frac{1120\mu_3^2\mu_4\mu_8}{\mu_2^3}-\frac{7168\mu_3^2\mu_5\mu_7}{\mu_2^3}\\
&-\frac{4480\mu_3\mu_4^2\mu_7}{\mu_2^3}-\frac{7840\mu_3\mu_4\mu_5\mu_6}{\mu_2^3}-\frac{6272\mu_3\mu_5^3}{\mu_2^3}+\frac{128\mu_3\mu_7\mu_8}{\mu_2^3}-\frac{4900\mu_4^3\mu_6}{\mu_2^3}-\frac{3920\mu_4^2\mu_5^2}{\mu_2^3}\\
&+\frac{140\mu_4\mu_6\mu_8}{\mu_2^3}+\frac{112\mu_5^2\mu_8}{\mu_2^3}+\frac{3136\mu_3^2\mu_4\mu_5^2}{\mu_2^4}+\frac{3920\mu_3\mu_4^3\mu_5}{\mu_2^4}\\
&-\frac{112\mu_3\mu_4\mu_5\mu_8}{\mu_2^4}+\frac{1225\mu_4^5}{\mu_2^4}-\frac{70\mu_4^3\mu_8}{\mu_2^4}+\frac{\mu_4\mu_8^2}{\mu_2^4})/n,
\end{aligned}
$$

$$
\mathrm{Var}(\kappa_2/\kappa_1)=(-\frac{\mu_2^2}{\langle N\rangle^2}+\frac{\mu_4}{\langle N\rangle^2}-\frac{2\mu_2\mu_3}{\langle N\rangle^3}+\frac{\mu_2^3}{\langle N\rangle^4})/n,
$$

$$
\begin{aligned}
\mathrm{Var}(\kappa_3/\kappa_1)=&(\frac{9\mu_2^3}{\langle N\rangle^2}-\frac{9\mu_2^2}{\langle N\rangle^2}+\frac{24\mu_2\mu_3}{\langle N\rangle^2}-\frac{6\mu_2\mu_4}{\langle N\rangle^2}-\frac{\mu_3^2}{\langle N\rangle^2}+\frac{9\mu_4}{\langle N\rangle^2}-\frac{6\mu_5}{\langle N\rangle^2}\\
&+\frac{\mu_6}{\langle N\rangle^2}-\frac{18\mu_2^3}{\langle N\rangle^3}+\frac{6\mu_2^2\mu_3}{\langle N\rangle^3}-\frac{18\mu_2\mu_3}{\langle N\rangle^3}+\frac{6\mu_2\mu_4}{\langle N\rangle^3}\\
&+\frac{6\mu_3^2}{\langle N\rangle^3}-\frac{2\mu_3\mu_4}{\langle N\rangle^3}+\frac{9\mu_2^3}{\langle N\rangle^4}-\frac{6\mu_2^2\mu_3}{\langle N\rangle^4}+\frac{\mu_2\mu_3^2}{\langle N\rangle^4})/n,
\end{aligned}
$$

$$
\begin{aligned}
\mathrm{Var}(\kappa_4/\kappa_1)=&(-\frac{36\mu_2^4}{\langle N\rangle^2}+\frac{456\mu_2^3}{\langle N\rangle^2}-\frac{432\mu_2^2\mu_3}{\langle N\rangle^2}+\frac{48\mu_2^2\mu_4}{\langle N\rangle^2}-\frac{121\mu_2^2}{\langle N\rangle^2}+\frac{64\mu_2\mu_3^2}{\langle N\rangle^2}\\
&+\frac{528\mu_2\mu_3}{\langle N\rangle^2}-\frac{370\mu_2\mu_4}{\langle N\rangle^2}+\frac{108\mu_2\mu_5}{\langle N\rangle^2}-\frac{12\mu_2\mu_6}{\langle N\rangle^2}-\frac{124\mu_3^2}{\langle N\rangle^2}+\frac{60\mu_3\mu_4}{\langle N\rangle^2}-\frac{8\mu_3\mu_5}{\langle N\rangle^2}\\
&-\frac{\mu_4^2}{\langle N\rangle^2}+\frac{121\mu_4}{\langle N\rangle^2}-\frac{132\mu_5}{\langle N\rangle^2}+\frac{58\mu_6}{\langle N\rangle^2}-\frac{12\mu_7}{\langle N\rangle^2}+\frac{\mu_8}{\langle N\rangle^2}+\frac{108\mu_2^4}{\langle N\rangle^3}-\frac{60\mu_2^3\mu_3}{\langle N\rangle^3}-\frac{396\mu_2^3}{\langle N\rangle^3}\\
&+\frac{502\mu_2^2\mu_3}{\langle N\rangle^3}-\frac{72\mu_2^2\mu_4}{\langle N\rangle^3}+\frac{6\mu_2^2\mu_5}{\langle N\rangle^3}-\frac{120\mu_2\mu_3^2}{\langle N\rangle^3}+\frac{20\mu_2\mu_3\mu_4}{\langle N\rangle^3}-\frac{242\mu_2\mu_3}{\langle N\rangle^3}+\frac{132\mu_2\mu_4}{\langle N\rangle^3}\\
&-\frac{22\mu_2\mu_5}{\langle N\rangle^3}+\frac{132\mu_3^2}{\langle N\rangle^3}-\frac{94\mu_3\mu_4}{\langle N\rangle^3}+\frac{12\mu_3\mu_5}{\langle N\rangle^3}+\frac{12\mu_4^2}{\langle N\rangle^3}-\frac{2\mu_4\mu_5}{\langle N\rangle^3}+\frac{9\mu_2^5}{\langle N\rangle^4}-\frac{66\mu_2^4}{\langle N\rangle^4}+\frac{36\mu_2^3\mu_3}{\langle N\rangle^4}\\
&-\frac{6\mu_2^3\mu_4}{\langle N\rangle^4}+\frac{121\mu_2^3}{\langle N\rangle^4}-\frac{132\mu_2^2\mu_3}{\langle N\rangle^4}+\frac{22\mu_2^2\mu_4}{\langle N\rangle^4}+\frac{36\mu_2\mu_3^2}{\langle N\rangle^4}-\frac{12\mu_2\mu_3\mu_4}{\langle N\rangle^4}+\frac{\mu_2\mu_4^2}{\langle N\rangle^4})/n,
\end{aligned}
$$

$$
\mathrm{Var}(\kappa_2)=(-\mu_2^2+\mu_2-2\mu_3+\mu_4)/n,
$$

$$
\mathrm{Var}(\kappa_3)=(9\mu_2^3-21\mu_2^2+24\mu_2\mu_3-6\mu_2\mu_4+4\mu_2-\mu_3^2-12\mu_3+13\mu_4-6\mu_5+\mu_6)/n,
$$

$$
\begin{aligned}
\mathrm{Var}(\kappa_4)=&(-36\mu_2^4+456\mu_2^3-432\mu_2^2\mu_3+48\mu_2^2\mu_4-337\mu_2^2+64\mu_2\mu_3^2+648\mu_2\mu_3\\
&-370\mu_2\mu_4+108\mu_2\mu_5-12\mu_2\mu_6+36\mu_2-124\mu_3^2+60\mu_3\mu_4-8\mu_3\mu_5\\
&-132\mu_3-\mu_4^2+193\mu_4-144\mu_5+58\mu_6-12\mu_7+\mu_8)/n,
\end{aligned}
$$

$$
\mathrm{Var}(\kappa_5)=(\mu_{10}+900\mu_2^5-9900\mu_2^4+8400\mu_2^3\mu_3-900\mu_2^3\mu_4+18465\mu_2^3-1000\mu_2^2\mu_3^2
$$

$$
\begin{aligned}
&- 30200\mu_2^2\mu_3 + 10050\mu_2^2\mu_4 - 1920\mu_2^2\mu_5 + 160\mu_2^2\mu_6 - 7540\mu_2^2 + 9900\mu_2\mu_3^2 \\
&- 3400\mu_2\mu_3\mu_4 + 240\mu_2\mu_3\mu_5 + 18800\mu_2\mu_3 + 125\mu_2\mu_4^2 - 15070\mu_2\mu_4 \\
&+ 7400\mu_2\mu_5 - 2110\mu_2\mu_6 + 320\mu_2\mu_7 - 20\mu_2\mu_8 + 576\mu_2 - 800\mu_3^3 + 200\mu_3^2\mu_4 \\
&- 5705\mu_3^2 + 5000\mu_3\mu_4 - 1570\mu_3\mu_5 + 280\mu_3\mu_6 - 20\mu_3\mu_7 - 2400\mu_3 - 450\mu_4^2 \\
&+ 120\mu_4\mu_5 - 10\mu_4\mu_6 + 4180\mu_4 - \mu_5^2 - 3980\mu_5 + 2273\mu_6 - 800\mu_7 + 170\mu_8 - 20\mu_9)/n, \\
\mathrm{Var}(\kappa_6) = &(-30\mu_{10}\mu_2 + 395\mu_{10} - 30\mu_{11} + \mu_{12} - 8100\mu_2^6 + 294300\mu_2^5 - 243000\mu_2^4\mu_3 + 13500\mu_2^4\mu_4 \\
&- 916920\mu_2^4 + 39600\mu_2^3\mu_3^2 + 1395000\mu_2^3\mu_3 - 340200\mu_2^3\mu_4 + 48600\mu_2^3\mu_5 - 2880\mu_2^3\mu_6 \\
&+ 843105\mu_2^3 - 510600\mu_2^2\mu_3^2 + 144000\mu_2^2\mu_3\mu_4 - 9720\mu_2^2\mu_3\mu_5 - 1838400\mu_2^2\mu_3 - 3600\mu_2^2\mu_4^2 \\
&+ 918810\mu_2^2\mu_4 - 313650\mu_2^2\mu_5 + 67620\mu_2^2\mu_6 - 8100\mu_2^2\mu_7 + 405\mu_2^2\mu_8 - 237076\mu_2^2 + 48000\mu_2\mu_3^3 \\
&- 9600\mu_2\mu_3^2\mu_4 + 876620\mu_2\mu_3^2 - 548250\mu_2\mu_3\mu_4 + 115200\mu_2\mu_3\mu_5 - 14700\mu_2\mu_3\mu_6 + 840\mu_2\mu_3\mu_7 \\
&+ 697200\mu_2\mu_3 + 48525\mu_2\mu_4^2 - 10350\mu_2\mu_4\mu_5 + 510\mu_2\mu_4\mu_6 - 683810\mu_2\mu_4 + 216\mu_2\mu_5^2 \\
&+ 439710\mu_2\mu_5 - 183218\mu_2\mu_6 + 48900\mu_2\mu_7 - 8070\mu_2\mu_8 + 750\mu_2\mu_9 + 14400\mu_2 - 400\mu_3^4 \\
&- 111000\mu_3^3 + 72200\mu_3^2\mu_4 - 8400\mu_3^2\mu_5 + 440\mu_3^2\mu_6 - 272945\mu_3^2 - 9750\mu_3\mu_4^2 + 1020\mu_3\mu_4\mu_5 \\
&+ 322950\mu_3\mu_4 - 146298\mu_3\mu_5 + 45150\mu_3\mu_6 - 8580\mu_3\mu_7 + 900\mu_3\mu_8 - 40\mu_3\mu_9 - 65760\mu_3 \\
&+ 225\mu_4^3 - 49195\mu_4^2 + 24750\mu_4\mu_5 - 4970\mu_4\mu_6 + 600\mu_4\mu_7 - 30\mu_4\mu_8 + 129076\mu_4 - 1245\mu_5^2 \\
&+ 210\mu_5\mu_6 - 12\mu_5\mu_7 - 143700\mu_5 - \mu_6^2 + 100805\mu_6 - 46710\mu_7 + 14523\mu_8 - 3000\mu_9)/n.
\end{aligned}
$$

C: Statistical Uncertainty of Efficiency Corrected Cumulants

In this section we show formulas for statistical uncertainty of detector efficiency corrected cumulants only up to 2$^{\text{nd}}$ order due to length limit of thesis. The number of terms rises quite high when it goes up to 3$^{\text{rd}}$ order. The formulas are derived according to Delta theorem [75, 84] by means of several useful Python [98] packages like Sympy [99]. The code is shared online [100] and one can use it to generate higher-order formulas.

$$
\begin{aligned}
\mathrm{Var}(C_1) = &(-\langle Q_{(1,1)}\rangle^2 + \langle Q_{(1,1)}^2\rangle)/n, \\
\mathrm{Var}(C_2) = &(-2 * \langle Q_{(1,1)}\rangle * (-\langle Q_{(1,1)}\rangle * \langle Q_{(1,1)}^2\rangle + \langle Q_{(1,1)}^3\rangle) \\
&- 2 * \langle Q_{(1,1)}\rangle * (-\langle Q_{(1,1)}\rangle * \langle Q_{(2,1)}\rangle + \langle Q_{(1,1)}Q_{(2,1)}\rangle) + 2 * \langle Q_{(1,1)}\rangle * (-\langle Q_{(1,1)}\rangle * \langle Q_{(2,2)}\rangle \\
&+ \langle Q_{(1,1)}Q_{(2,2)}\rangle) - 2 * \langle Q_{(1,1)}\rangle * (-\langle Q_{(1,1)}\rangle * \langle Q_{(1,1)}^2\rangle - \langle Q_{(1,1)}\rangle * \langle Q_{(2,1)}\rangle + \langle Q_{(1,1)}\rangle * \langle Q_{(2,2)}\rangle \\
&- 2 * \langle Q_{(1,1)}\rangle * (-\langle Q_{(1,1)}\rangle^2 + \langle Q_{(1,1)}^2\rangle) + \langle Q_{(1,1)}^3\rangle + \langle Q_{(1,1)}Q_{(2,1)}\rangle - \langle Q_{(1,1)}Q_{(2,2)}\rangle) \\
&- \langle Q_{(1,1)}^2\rangle^2 - 2 * \langle Q_{(1,1)}^2\rangle * \langle Q_{(2,1)}\rangle + 2 * \langle Q_{(1,1)}^2\rangle * \langle Q_{(2,2)}\rangle + 2 * \langle Q_{(1,1)}^2 Q_{(2,1)}\rangle
\end{aligned}
$$

$$
\begin{aligned}
&- 2 * \langle Q^2_{(1,1)} Q_{(2,2)} \rangle + \langle Q^4_{(1,1)} \rangle - \langle Q_{(2,1)} \rangle^2 + 2 * \langle Q_{(2,1)} \rangle * \langle Q_{(2,2)} \rangle + \langle Q^2_{(2,1)} \rangle \\
&- 2 * \langle Q_{(2,1)} Q_{(2,2)} \rangle - \langle Q_{(2,2)} \rangle^2 + \langle Q^2_{(2,2)} \rangle)/n.
\end{aligned}
$$